

Modelling granular flows impinging on an inclined plane with use of an open source DPM code in 3D

R.H.A. Fransen, BSc

FACULTY OF ENGINEERING TECHNOLOGY
MULTI SCALE MECHANICS GROUP

Examination committee

Dr. T. Weinhart
Prof. Dr. rer.-nat. S. Luding
Dr. A.R. Thornton
Dr. ir. M. Masen

Document number
MSM-001

Summary

Granular materials have a multiphase behaviour as they can behave like solids, fluids or gases. They appear in many industrial applications such as food processing or pharmaceuticals and also in geotechnical and -physical phenomena like avalanches. This study considers a test-problem where a granular jet impinges on an inclined plane resulting in a hydraulic shock enclosing a region of thin fast-flowing flow. Such an impingement has been studied extensively with experiments and finite volume methods. However, the applied model lacks the full details of the three-dimensional flow near, e.g. the impingement zone due to the assumption that the flow satisfies the depth-averaged granular shallow flow equations in all regions. The discrete particle method (DPM) is able to provide the fully three-dimensional details for the flow in all regions which is the reason for choosing this method. The simulations are performed with an open source DPM solver, Mercury, which is developed within the Multi Scale Mechanics group and modified to capture the problem. This method simulates the movement of individual particles over many time-steps, where the movement of the particles changes due to collisions with other particles or objects. The three-dimensional discrete results are interactively examined with an OpenGL based software package, VMD, which has been extended and adapted for the analysis of DPM. The discrete results are also coarse grained to obtain continuous fields for all regions including those where the earlier finite volume results, which are based on the granular shallow flow equations, could not reproduce the experimental observations.

Visual observations of the discrete results, for the set of parameters used, indicate that the flow differs from earlier experimental work in the strength of the hydraulic jump and the down-slope velocity of the flow outside the enclosed region. These differences are closer investigated with the coarse graining method which is subjected to a sensibility study and checked for compatibility with continuity. Analysis on the influence of system parameters like the falling height and inclination angle are consistent with some of the earlier work. However, discrepancies in the shape of the enclosed region are encountered and the height-velocity graphs confirm the weakness of the hydraulic jump, due to insufficient mass flux in the system, which is limited by CPU-power. Furthermore, on the theoretical side, dimensionless numbers such as the Knudsen number are calculated to validate the assumptions made in the derivation of the granular shallow flow equations and another example of such dimensionless number is the Froude number which is necessary for the characterisation of the dilute enclosed region.

Irrespective of the stated differences, DPM is able to model such a complex flow on a detailed level. Nevertheless, for a higher mass flux, the computational time has to be reduced by parallelisation to describe the flow behaviour in the interesting high mass flux regime. Profiling of the applied solver and a preliminary study on the application of the OpenMP method on the existing open source solver showed that this parallelisation method on its own will not result in a significant speed-up. A combination of MPI and OpenMP parallelisation is therefore advised.

Preface

‘Kapot maken is ook maken’ is a Dutch saying which can be roughly translated in ‘Destroying is just another method of creating’. My love for this saying resulted in the construction of a trebuchet in the last and biggest practical project within my secondary school. It is a medieval tool of war based on acceleration of a projectile due to a falling mass. This project enthused me for the bachelor Mechanical Engineering at the University of Twente. The diploma of this education came three years later and my interest in numerical studies has grown significantly in those years. Choosing the Multi Scale Mechanics group was based on my broad interest in both multidisciplinary applied mathematics and numerical methods which are needed to solve discrete particle simulations.

This thesis is part of my masterprogramme Mechanical Engineering within the University of Twente and contains a numerical study involving 1,000,000 particles. Both the mathematics and the numerical approach merge in the problem and it is close to topics in information technology. During the nine months project, Thomas Weinhart supervised the project, pointing out interesting phenomena or numerical methods. Furthermore, he spend a lot of time in reading and improving the thesis for which I’d like to thank him. Other persons involved are Anthony Thornton and Stefan Luding on the scientific part of the study and Tessa Jansen and Dinant Krijgsman as my room-mates. Furthermore, I’d like to thank any other person involved in my educational career which made it possible to combine work and study within the University of Twente.

Rudi H. A. Fransen, March 2, 2012

Contents

Summary	i
Preface	iii
Nomenclature	vii
1 Introduction	1
2 Theoretical background	5
2.1 Discrete Particle Method	5
2.1.1 Contact model	5
2.1.2 Time integration	8
2.2 Derivation of shallow granular flow equations	10
2.2.1 Reynolds transport theorem	10
2.2.2 Conservation of mass	11
2.2.3 Conservation of momentum	12
2.2.4 Further assumptions	13
2.2.5 Boundary conditions	14
2.2.6 Dimensionless form	15
2.2.7 Depth-averaged modelling	16
2.2.8 Closure relations	19
2.2.9 Jump conditions	20
2.3 Statistics	22
2.3.1 Basic idea	22
2.3.2 Continuity	25
2.3.3 Conservation of momentum	25
2.4 Dimensional analysis	29
2.4.1 Buckingham's π theorem	29
2.4.2 Dimensionless height	31
2.4.3 Froude number	31
2.4.4 Knudsen number	31
3 Simulation setup	33
3.1 Overview	33
3.2 Particle properties	33
3.3 Funnel properties	33
3.4 Bottom plate	34
3.5 Particle removal	35
4 Visualisation	37
4.1 Output	37
4.1.1 Data file	37
4.1.2 Fstat file	37
4.1.3 Restart file	38
4.1.4 Ene file	38
4.2 Launch script	38
4.3 Visualisation script	38

4.3.1	Read arguments	38
4.3.2	Gather parameters	38
4.3.3	Prepare VMD	38
4.3.4	Load data	39
4.3.5	Show particles	39
4.3.6	Show walls	39
5	Results	41
5.1	Discrete results	41
5.1.1	Funnel	41
5.1.2	Impingement	42
5.1.3	Plate flow	42
5.1.4	Hydraulic jump	42
5.1.5	Conclusion	45
5.2	Coarse graining parameters	45
5.2.1	Typical volume fraction	45
5.2.2	Height	47
5.2.3	Speed	47
5.2.4	Conclusion	48
5.3	Steady state	49
5.3.1	Definition of steady state	49
5.3.2	Number of particles	49
5.3.3	Time averaged statistics	50
5.3.4	Conclusion	52
5.4	Knudsen number	52
5.5	Froude number	53
5.6	Flow Height	53
5.6.1	Top view	53
5.6.2	Cross sectional views	54
5.6.3	Conclusion	54
5.7	Characteristics of the enclosed region	54
5.7.1	Length of the enclosed region	55
5.7.2	Width of the enclosed region	55
5.7.3	Conclusion	55
5.8	Parameter study	55
5.8.1	Inclination angle	55
5.8.2	Falling height	57
5.8.3	Conclusions	57
5.9	Highly kinetic flow	58
5.9.1	Setup parameters	58
5.9.2	Mass flow	58
5.9.3	Plate flow	58
5.9.4	Critical transition	59
5.9.5	Froude number	59
5.9.6	Height of the flow	59
5.9.7	Impingement	61
5.9.8	Conclusions	62
6	Parallelisation	63
6.1	Profiler	63
6.2	OpenMP	65
6.2.1	Introduction into OpenMP	65
6.2.2	Parallelising Mercury	66
7	Conclusion and discussion	69
	Bibliography	72

Nomenclature

S.	Description	Units
\underline{B}	Body forces	$[\text{kg m s}^{-2}]$
D	Funnel diameter	$[\text{m}]$
\mathcal{D}	Number of dimensions	$[-]$
Fr	Froude number	$[-]$
H	Typical flow depth	$[\text{m}]$
H_f	Falling height	$[\text{m}]$
I_i	Inertia of particle i	$[\text{kg m}^2]$
Kn	Knudsen number	$[-]$
L	Length of the plate	$[\text{m}]$
N	Number of particles	$[-]$
P	Momentum	$[\text{kg m}^{-2} \text{s}^{-1}]$
$\ U\ $	Macroscopic speed	$[\text{m s}^{-1}]$
V	Control volume	$[\text{m}^3]$
W	Width of the plate	$[\text{m}]$
X	the length of the x domain	$[\text{m}]$
Y	the length of the y domain	$[\text{m}]$
Z	the length of the z domain	$[\text{m}]$
\mathcal{W}	Coarse graining function	$[\text{m}^{-\mathcal{D}}]$
b	Basal coordinate	$[\text{m}]$
\underline{b}_{ij}	Branch vector	$[\text{m}]$
\underline{c}	Location of the contact point	$[\text{m}]$
d	Particle's diameter	$[\text{m}]$
e	Coefficient of restitution	$[-]$
\underline{f}	Force	$[\text{kg m s}^{-2}]$
g	Gravitational constant	$[\text{m s}^{-2}]$
h	Height of the flow	$[\text{m}]$
k	Linear stiffness coefficient	$[\text{kg s}^{-2}]$

Table 1: Latin symbols (1)

S.	Description	Units
m_i	Mass of particle i	[kg]
n_z	Number of particles along funnel side	[–]
\underline{n}	Unit normal vector	[–]
p	Pressure	[kg m ⁻¹ s ⁻¹]
\underline{r}_i	Position of particle i	[m]
s	Surface coordinate	[m]
t	Time	[s]
t_c	Collision time	[s]
\underline{t}_i	Torque acting on particle i	[kg m ² s ⁻²]
u	Velocity component in x direction	[m s ⁻¹]
\underline{u}	Velocity	[m s ⁻¹]
v	Velocity component in y direction	[m s ⁻¹]
w	Velocity component in z direction	[m s ⁻¹]
w	Coarse graining width	[m]
x	Coordinate along the plate	[m]
x_0	Lower limit of the x domain	[m]
x_1	High limit of the x domain	[m]
y	Coordinate over the width of the plate	[m]
y_0	Lower limit of the y domain	[m]
y_1	High limit of the y domain	[m]
z	Coordinate perpendicular to the plate	[m]
z_0	Lower limit of the z domain	[m]
z_1	High limit of the z domain	[m]

Table 2: Latin symbols (2)

S.	Description	Units
Δ	Length of the normal vector	[m]
α	Funnel angle	[–]
γ	Linear dissipation coefficient	[kg s ⁻¹]
δ	Basal angle of friction	[–]
δ_i	Dirac delta function for particle i	[–]
δ_{ij}	Overlap between particle i and j	[m]
ε	Ratio of the typical flow height and plate length	[–]
ζ	Inclination angle	[–]
η	Effective viscosity	[s ⁻¹]
θ	Rotational angle	[–]
λ	Mean free path	[m]
μ_c	Friction coefficient	[–]
ν	Volume fraction	[–]
ρ	Density	[kg m ⁻³]
$\underline{\sigma}$	Stress	[kg m ⁻¹ s ⁻²]
τ	Shear stress	[kg m ⁻¹ s ⁻²]
ϕ	Internal angle of friction	[–]
φ	Typical volume fraction	[–]
ω	Frequency	[s ⁻¹]
Δt	Measurable time increment	[s]
∂V	Surface of the control volume	[m ²]

Table 3: Greek and other symbols

Chapter 1

Introduction

Granular materials have a multiphase behaviour as they can behave like solids, fluids or gases. A good example is sand: one can walk on the beach (as on a solid) compressing many grains at a time but the wind can also lift up several grains, forming a cloud. Therefore, different boundary conditions or loadings require different approaches in solving the given problem or phenomenon. Other examples exist in industrial applications such as grains within a silo. These grains are able to exert big stresses perpendicular to the wall due to force-chains whereas a fluid is only able to exert a hydrostatic pressure. Describing a flow of grains is phenomenological different from the flow of typical fluids due to, for instance, the presence of friction and existing continuum models need modifications to capture these flows. Many experiments and simulations are performed on granular materials to understand their behaviour in all kinds of phases and some examples are shown in [2, 6, 11–13, 17, 19, 21, 30].

In general, there are two approaches in the simulation of flowing granular materials. People either use the finite volume method which is based on the granular shallow flow equations to obtain two-dimensional results or the discrete particle method (DPM) which solves the flow particle-wise, providing fully three-dimensional details of the flow. The former has the advantage that it is significantly faster than the latter due to the assumptions made. However, a closure relation for the friction in the system is needed, it only produces two-dimensional output and boundary conditions must be stated yielding a decrease of the output's accuracy. Using a time-dependent three-dimensional inflow, such as a funnel, is therefore not possible and estimated models are used to fit those conditions. The discrete particle method, on the other hand, is very computationally expensive due to the particle-wise solution method, i.e. Newton's equations of motion need to be solved with a very small time-step to produce accurate results. However, the method has the big advantage that the three-dimensional flow is simulated with all of its details included allowing for a detailed investigation of these complex three-dimensional flows.

This study considers a test-problem where a granular jet impinges on an inclined plane resulting in a hydraulic shock enclosing a region of thin fast-flowing flow, see figure 1.1. Such a jet is formed by millions of particles and the problem can thus be considered as a very computationally expensive problem from a DPM point of view. The problem was first studied in 1914, when Lord Rayleigh [18] investigated an inviscid fluid impinging perpendicular on a horizontal plane, generating a thin, circular region of rapid radial flow which is surrounded by a static hydraulic shock. Hereafter, many others extended this problem in several ways from which the investigated fluid properties like viscosity [28] or surface tension [3] are examples. Replacement of the fluid by a granular material [2] or the replacement of the horizontal plane by an inclined plane [17] are other examples. On the theoretical side, models are developed providing an analytic solution for these flows [1, 4, 10, 25]. Particle based methods are also developed to obtain a fully three-dimensional discrete set of results [20, 21, 26]. Furthermore, statistical methods [8, 30] are developed to compare the discrete results to the analytical models.

The granular jet impinging on an inclined plane has experimentally been observed by Johnson and Gray [17] and these observations are verified in the same work with the finite volume method [29] based on the closure relations proposed by Pouliquen and Forterre [24] for shallow granular flow. However, the applied model lacks the full details of the three-dimensional flow near, e.g. the impingement zone due to the assumption that the flow satisfies the depth-averaged granular shallow flow equations in all regions. Important details of the flow thus still missing and the discrete particle method [21] is applied to this problem, resolving the missing details. This method simulates the movement of individual particles over many time-steps, where the movement of the particles changes due to collisions with other particles or objects. The resulting flow allows for steady states in which 1) static, 2) sub- and

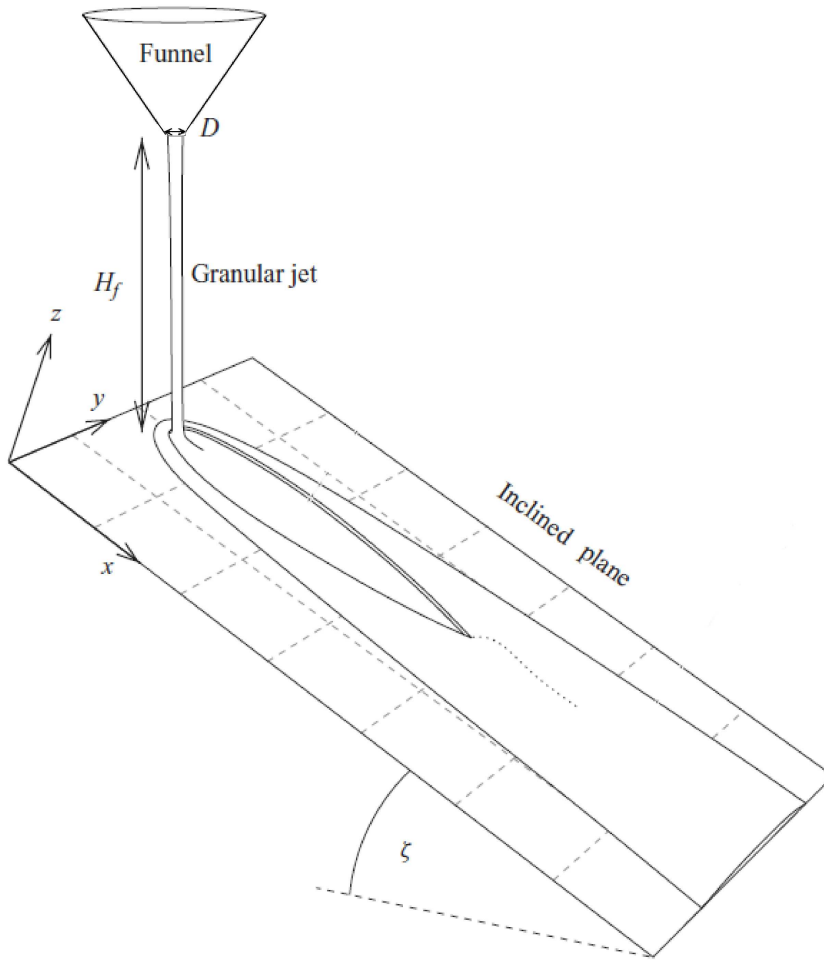


Figure 1.1: Experimental setup [17]

3) supercritical flow can be observed in different parts of the domain which is shown in figure 1.1. This figure shows the setup of the problem as used by Johnson and Gray for their experiments. The occurrence of different flow regimes is, among other parameters, dependent on the height of the funnel, H_f , from which the granular medium is released and the angle, ζ , at which the plane is inclined. For large drop heights or angles, a teardrop-shaped shock is formed while lower values result in a blunted shock. Mass flow is controlled by setting the diameter of the funnel, D . Note that the results of the DPM simulations performed will significantly depend on the mass flow used but that it is limited by the available CPU power. The main scientific research question is stated as: *Up to which level of detail is DPM capable of simulating a granular jet impinging on an inclined plane, confirming both the experiments as well the finite volume results from Johnson and Gray [17]?* Answering this question will be done by answering the following set of sub-questions:

- Does the flow profile within the impingement zone as found with the DPM model satisfy the assumptions made in the granular shallow layer equations?
- Is the DPM method capable of capturing a phenomenon similar to the hydraulic shock observed in the original work?
- Can both typical solutions, found in the experiments and finite volume results, for the enclosed region be found with the DPM method?

- Is the DPM method capable of describing the fully three-dimensional flow at the down-slope edge of the enclosed region?
- Can the computational time of the DPM method as used in the open source software Mercury [26] significantly be reduced by applying the OpenMP parallelisation method?

Answering the listed questions requires analysing the mathematical foundation containing the Discrete Particle Method, the derivation of the granular shallow flow equations and the statistical method as shown in chapter 2. The simulation setup as it is used in the DPM simulations is shown in chapter 3 which is followed by a description of the visualisation method in chapter 4. This method is based on an OpenGL engine, VMD [16], which is modified to represent DPM simulations in a fully three-dimensional environment, allowing for detailed inspections of the three-dimensional flow. The outcome of the simulations is shown in chapter 5 where all aspects of the flow are discussed for multiple setups. The fifth research question is addressed by a preliminary study on the OpenMP parallelisation method as shown in chapter 6. All findings are concluded and discussed in chapter 7 which concludes this thesis.

Chapter 2

Theoretical background

The first topic described in this chapter is the Discrete Particle Method (§2.1) explaining the numerical model which predicts the movement of the particles by solving Newton's second law. Secondly, a detailed derivation of the depth-averaged shallow granular flow equations (§2.2) is given, explaining the continuum approach to the problem. Thereafter, a coarse-graining method (§2.3) is worked out which is applied on the discrete results to find a continuous solution. The section concludes with a dimensional analysis (§2.4), identifying relevant dimensionless groups.

2.1 Discrete Particle Method

The Discrete Particle Method (DPM) is used to simulate the movement of individual particles or atoms. It is assumed that a particle's trajectory may only change due to external forces acting on this particle. The movement due to these forces can be described by Newton's equation of motion for the translational and rotational degrees of freedom [21],

$$m_i \frac{d^2}{dt^2} \underline{r}_i = m_i \ddot{\underline{r}}_i = \underline{f}_i, \quad \text{and} \quad I_i \frac{d^2}{dt^2} \underline{\theta}_i = I_i \ddot{\underline{\theta}}_i = \underline{t}_i, \quad (2.1)$$

with the mass m_i of particle i , its position \underline{r}_i and the total force \underline{f}_i for the translational set of equations. The rotational set of equations make use of the particle's moment of inertia I_i , its rotational position $\underline{\theta}_i$ and the total torque \underline{t}_i . Note that underlined variables indicate \mathcal{D} dimensional vectors in space. The forces and torques acting on particle i are described in §2.1.1. The total set of equations form a set of coupled ordinary differential equations which can be time integrated numerically as described in §2.1.2.

2.1.1 Contact model

This section gives a detailed description of the applied force model. The force model in a DPM simulation can cover long range interactions like electrostatic, Lennard-Jones or Van der Waals interactions for nano-scale DPM simulations, or contact forces in grain simulations. Body forces such as gravity, external magnetic fields or drag forces can also be included. The problem at hand considers sand where particle interactions can be described by a short range force model and such a model is implemented in Mercury [26], a DPM simulation tool developed by the Multi Scale Mechanics group of the University of Twente. The linear spring-dashpot interaction model [7] is such a short range force model where binary particle collisions are modelled by an elastic and dissipative force. This section starts with a detailed description of the normal component of this model. The analytical solution of this component is used to derive a collision time and restitution coefficient which are typical DPM parameters. The model is extended by modelling forces acting in tangential direction which requires the solving of Newton's equations of motion for both the translational and rotational degrees of freedom of the particles. Figure 2.1 shows two particles (i, j) interacting by the proposed interaction model in which the springs and dashpots are clearly visible and a general split of the forces,

$$\underline{f}_{ij} = \underline{f}_{ij}^n + \underline{f}_{ij}^t, \quad (2.2)$$

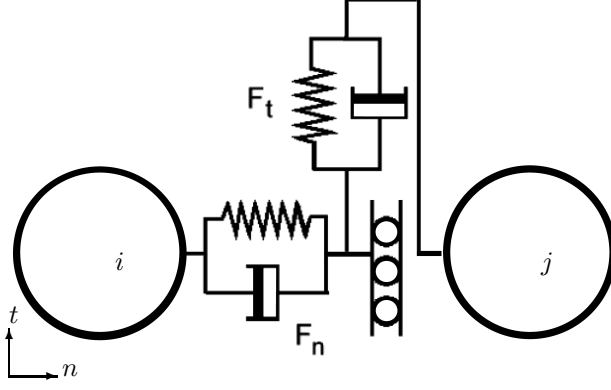


Figure 2.1: The contact forces for a particle-particle collision involving normal and tangential springs and dashpots.

is allowed by superposition. The total forces acting on particle i can be described as,

$$\underline{f}_i = \underline{B} + \sum_{j=1}^{N_m} \underline{f}_{ij}, \quad (2.3)$$

where \underline{B} are body forces like gravity. The rotational degrees of freedom can be calculated by solving the second equation in (2.1) with the use of,

$$\underline{t}_i = \sum_{j=1}^{N_m} \underline{b}_{ij} \times \underline{f}_{ij}. \quad (2.4)$$

Next, the particle-particle contact model is described in normal direction.

Spring-dashpot interaction model in normal direction

The standard spring-dashpot interaction model [21,30] assumes that the particles are soft and spherical. Furthermore, it is assumed that particle pairs in contact have a single contact point \underline{c}_{ij} . The properties of particle i are its diameter d_i , mass m_i , position $\underline{r}_i(t)$ and angular velocity $\dot{\underline{\theta}}_i(t)$. Each pair of particles has a relative distance $\underline{r}_{ij} = \underline{r}_i - \underline{r}_j$, a unit normal vector $\underline{n}_{ij} = \underline{r}_{ij} / \|\underline{r}_{ij}\|$ and an overlap $\delta_{ij} = (d_i + d_j)/2 - \|\underline{r}_{ij}\|$ if the particles are in contact. These definitions make use of the Euclidian norm which is denoted by $\|A\|$ and the definition of the overlap is used to derive,

$$\dot{\delta}_{ij} = \frac{d\delta_{ij}}{dt} = -\frac{d}{dt} \|\underline{r}_{ij}\| = -\frac{d}{dt} \sqrt{\underline{r}_{ij} \cdot \underline{r}_{ij}} = -\frac{\underline{r}_{ij} \cdot \dot{\underline{r}}_{ij}}{\|\underline{r}_{ij}\|} = -\dot{\underline{r}}_{ij} \cdot \underline{n}_{ij}. \quad (2.5)$$

$$\ddot{\delta}_{ij} = \frac{d\dot{\delta}_{ij}}{dt} = -\dot{\underline{r}}_{ij} \cdot \dot{\underline{n}}_{ij}, \quad (2.6)$$

where the Greek subscript α denote the α direction in space on which Einstein's summation convention is applied. The normal component of the forces, f_{ij}^n in a one-dimensional system consisting of two particles can be stated as,

$$f_{ij}^n = -k^n \delta_{ij} - \gamma^n \dot{\delta}_{ij}, \quad \text{if } \delta_{ij} \geq 0 \quad (2.7)$$

with the linear spring constant k^n , linear damping coefficient γ^n in normal direction. Newton's third law ($f_{ij}^n = -f_{ji}^n$) is applied while substituting (2.7) into (2.1) for both particles,

$$m_i \ddot{r}_i = -k \delta_{ij} - \gamma \dot{\delta}_{ij}, \quad (2.8)$$

$$m_j \ddot{r}_j = k \delta_{ij} + \gamma \dot{\delta}_{ij}. \quad (2.9)$$

Introducing an equivalent mass $m_{eq} = m_i m_j / (m_i + m_j)$ and subtracting $m_i \times (2.9)$ from $m_j \times (2.8)$ yields,

$$\begin{aligned} m_i m_j \ddot{r}_i - m_i m_j \ddot{r}_j &= (m_i + m_j)(-k \delta_{ij} - \gamma \dot{\delta}_{ij}), \\ m_{eq} \ddot{\delta}_{ij} &= -k \delta_{ij} - \gamma \dot{\delta}_{ij}, \\ \ddot{\delta}_{ij} + 2\eta \dot{\delta}_{ij} + \omega_0^2 \delta_{ij} &= 0, \end{aligned} \quad (2.10)$$

which is the equation of motion for a damped harmonic oscillator [19, 22] with natural frequency ($\omega_0 = \sqrt{k/m_{eq}}$) and effective viscosity ($\eta = \gamma/2m_{eq}$).

Analytical solution

Equation 2.10 can be solved analytically with the standard solution [22],

$$\delta(t) = A \exp(st), \quad \dot{\delta}(t) = sA \exp(st), \quad \ddot{\delta}(t) = s^2 A \exp(st). \quad (2.11)$$

Substitution of (2.11) into (2.10) yields the characteristic equation,

$$s^2 + 2\eta s + \omega_0^2 = 0, \quad (2.12)$$

with the solution,

$$s_{1,2} = -\eta \pm \sqrt{\eta^2 - \omega_0^2}, \quad (2.13)$$

so that the solution of the equation of motion is,

$$\delta(t) = A_1 \exp\left(\left(-\eta + \sqrt{\eta^2 - \omega_0^2}\right)t\right) + A_2 \exp\left(\left(-\eta - \sqrt{\eta^2 - \omega_0^2}\right)t\right). \quad (2.14)$$

This equation can be simplified with the use of $\omega' = \sqrt{\eta^2 - \omega_0^2} = i\omega$ where $\omega = \sqrt{\omega_0^2 - \eta^2}$ and assuming $\eta < \omega_0$. Substitution yields,

$$\delta(t) = (A_1 \exp(i\omega t) + A_2 \exp(-i\omega t)) \exp(-\eta t). \quad (2.15)$$

The constants A_1 and A_2 can be found by using the initial conditions $\delta(0) = 0$ and $\dot{\delta}(0) = u_0$ meaning that the contact starts at $t = 0$ with no overlap and that the initial overlap velocity is equal to u_0 . Applying the first initial condition yields,

$$\delta(0) = A_1 + A_2 = 0, \quad A_1 = -A_2 = A, \quad (2.16)$$

which allows the simplification of (2.15) when Euler's formula is used,

$$\delta(t) = A (\exp(i\omega t) - \exp(-i\omega t)) \exp(-\eta t) = 2iA \exp(-\eta t) \sin(\omega t) = A' \exp(-\eta t) \sin(\omega t), \quad (2.17)$$

where A' can be found by using the second initial condition,

$$\dot{\delta}(t) = \omega A' \exp(-\eta t) \cos(\omega t) - \eta A' \exp(-\eta t) \sin(\omega t), \quad (2.18)$$

$$\dot{\delta}(0) = \omega A' = u_0, \quad A' = \frac{u_0}{\omega}. \quad (2.19)$$

The solution for the equation of motion can then be written as,

$$\delta(t) = \frac{u_0}{\omega} \exp(-\eta t) \sin(\omega t). \quad (2.20)$$

Spring-dashpot interaction model in tangential direction

The tangential part of the interaction is also based on the assumption that the contact force is described by linear elastic and dissipative contributions,

$$\underline{f}_{ij}^t = k^t \underline{\delta}_{ij}^t + \gamma^t \underline{\dot{\delta}}_{ij}^t, \quad (2.21)$$

with the linear tangential stiffness k^t and dissipation coefficient γ^t . The overlap in tangential direction is given by the implicit relation [30],

$$\frac{\underline{\delta}_{ij}^t}{dt} = \underline{\dot{r}}_{ij}^t - \frac{(\underline{\delta}_{ij}^t \cdot \underline{\dot{r}}_{ij}^t) \underline{n}_{ij}}{r_{ij}}, \quad (2.22)$$

and the relative tangential velocity at the contact point $\underline{\dot{r}}_{ij}^t$ is given by [30],

$$\underline{\dot{r}}_{ij}^t = \underline{\dot{r}}_{ij} - \underline{\dot{r}}_{ij} \cdot \underline{n}_{ij} - \underline{\dot{\theta}}_i \times \underline{b}_{ij} + \underline{\dot{\theta}}_j \times \underline{b}_{ji}, \quad (2.23)$$

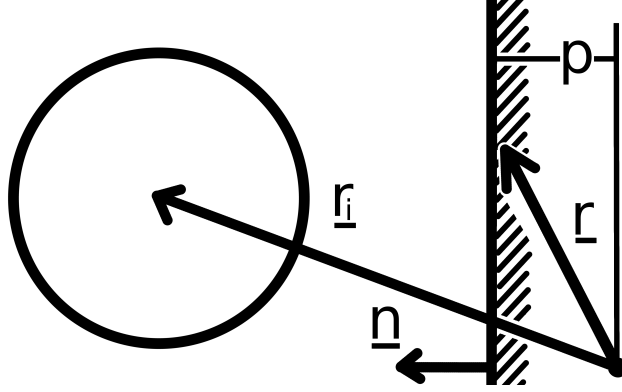


Figure 2.2: Schematic overview for a particle-wall collision.

with \underline{b}_{ij} the branch vector which is given by $\underline{b}_{ij} = -((d_i - \delta_{ij}^n)/2)\underline{n}_{ij}$ for poly-disperse systems and reduces to $\underline{b}_{ij} = -\underline{r}_{ij}/2$ for mono-disperse systems. This branch vector originates in the centre of mass of a particle, its length is the distance up to the contact point and it is orientated towards this contact point. Note that tangential forces in particle simulations should represent the particle roughness in experiments. For rough particles, the model for the tangential forces as shown in (2.21) should be able to model stick-slip behaviour. Particles will slip on each others surfaces when the ratio between tangential and normal forces due to this contact is bigger than the friction coefficient μ_c ,

$$\|\underline{f}_{ij}^t\| \leq \mu_c \|\underline{f}_{ij}^n\|. \quad (2.24)$$

Wall interactions

Walls can be built from fixed particles, a flat (planar) wall or a combination of the two. Fixed particles are particles with an infinite mass and therefore, they cannot be moved. These particles cause a normal overlap as explained in the previous section. A planar wall has the same contact properties as a fixed particle and an example is shown in figure 2.2. The wall can thus exert both normal and tangential forces and it is given by all points \underline{r} which satisfy,

$$\underline{r} \cdot \underline{n} = p, \quad (2.25)$$

where \underline{n} is the outward unit normal of the wall and p the position of the wall. The overlap resulting from a collision with particle i located at \underline{r}_i and the wall is then calculated by,

$$\delta_i = (\underline{r}_i \cdot \underline{n} - p) - \frac{d_i}{2} \quad \text{if } \delta_i \leq 0. \quad (2.26)$$

Conclusion

The movement of the particles can now be calculated by solving (2.3) and (2.4) in which the normal and tangential force contributions are calculated by (2.7) and (2.21) respectively. Furthermore, a collision time (2.36) and restitution coefficient (2.37) are derived and are used as input parameters in the DPM solver.

2.1.2 Time integration

Time integration of the equations of motion can be performed by several numerical schemes such as the Forward Euler, Verlet or Runge-Kutta schemes. The choice of a scheme is based on the needed accuracy and availability of calculation time. The Forward Euler scheme is not symplectic and hence energy is not conserved, while the Runge-Kutta assumes that the force model is a smooth function of the particle's degrees of freedom. The time integration method is therefore chosen to be the second order accurate and symplectic Velocity Verlet method which is a variant of the normal Verlet method with the advantage that the velocities are calculated as well. These velocities are needed in the calculation of the dissipative forces, influencing the acceleration of the particles. The scheme can be constructed

with use of Taylor expansions for position and rotational angle at $t + \Delta t$ up to the second order of Δt , where it is only shown for the position here,

$$\underline{r}(t + \Delta t) = \underline{r}(t) + \dot{\underline{r}}(t)\Delta t + \frac{1}{2}\ddot{\underline{r}}(t)\Delta t^2 + \mathcal{O}(\Delta t^3), \quad (2.27)$$

A second Taylor expansion is needed for the velocity at $t = t + 1/2\Delta t$,

$$\dot{\underline{r}}(t + \frac{1}{2}\Delta t) = \dot{\underline{r}}(t) + \frac{1}{2}\ddot{\underline{r}}(t)\Delta t + \mathcal{O}(\Delta t^2), \quad (2.28)$$

where the substitution of (2.28) into (2.27) lead to,

$$\underline{r}(t + \Delta t) = \underline{r}(t) + \dot{\underline{r}}(t + \frac{1}{2}\Delta t)\Delta t + \mathcal{O}(\Delta t^3), \quad (2.29)$$

A more complex scheme is used for the accelerations of the particles by using four additional Taylor expansions for the velocities,

$$\dot{\underline{r}}(t + \Delta t) = \dot{\underline{r}}(t) + \ddot{\underline{r}}(t)\Delta t + \mathcal{O}(\Delta t^2), \quad (2.30)$$

$$\dot{\underline{r}}(t) = \dot{\underline{r}}(t + \Delta t) - \ddot{\underline{r}}(t + \Delta t)\Delta t + \mathcal{O}(\Delta t^2), \quad (2.31)$$

$$(2.32)$$

which can be pairwise subtracted and divided by two to get,

$$\dot{\underline{r}}(t + \Delta t) = \dot{\underline{r}}(t) + \frac{\ddot{\underline{r}}(t) + \ddot{\underline{r}}(t + \Delta t)}{2}\Delta t + \mathcal{O}(\Delta t^2), \quad (2.33)$$

in which (2.28) can be substituted,

$$\dot{\underline{r}}(t + \Delta t) = \dot{\underline{r}}(t + \frac{1}{2}\Delta t) + \frac{1}{2}\ddot{\underline{r}}(t + \Delta t)\Delta t + \mathcal{O}(\Delta t^2), \quad (2.34)$$

Mercury [26] applies this time integration method for the position of the particles by first calculating (2.28) while neglecting higher order terms. This computation is followed by (2.29) and the accelerations of the particles are calculated as described in §2.1.1. Equation (2.34) is thereafter executed, closing the cycle.

Collision time and restitution coefficient

The time integration method makes use of a discretized time scale based on a time step Δt . This method needs to cover all movements and interactions in the system. A sensible choice for the time-step is therefore based on analytical solution found in (2.20) which describes the overlap as a function of time for a one-dimensional collinear collision. It can be found by solving (2.20) for $\delta(t_c) = 0$ with $t_c \neq 0$, thus,

$$t_c = \pi/\omega. \quad (2.35)$$

Pseudocode 1 Time integration

Require: Initial positions

Begin

for $t = t_0 \rightarrow t_{max}$ **do**

$$\dot{\underline{r}} = \dot{\underline{r}} + \frac{1}{2}\ddot{\underline{r}}\Delta t$$

$$\dot{\underline{\theta}} = \dot{\underline{\theta}} + \frac{1}{2}\ddot{\underline{\theta}}\Delta t$$

$$\underline{r} = \underline{r} + \dot{\underline{r}}\Delta t$$

$$\underline{\theta} = \underline{\theta} + \dot{\underline{\theta}}\Delta t$$

$$\ddot{\underline{r}} \leftarrow \text{Force routine}$$

$$\ddot{\underline{\theta}} \leftarrow \text{Force routine}$$

$$\dot{\underline{r}} = \dot{\underline{r}} + \frac{1}{2}\ddot{\underline{r}}\Delta t$$

$$\dot{\underline{\theta}} = \dot{\underline{\theta}} + \frac{1}{2}\ddot{\underline{\theta}}\Delta t$$

$$t = t + \Delta t$$

end for

End

Extension to other types of collisions and dimensions result in slower collisions from which enduring collisions are an example. Capturing the full details of the movement of the particle during the collision is then ensured by a time-step of,

$$\Delta t = \frac{t_c}{50}, \quad (2.36)$$

which is used in the time integration method described in §2.1.2. The restitution coefficient, which is used to characterize the granular material, can also be determined by the equations of motion of the 1D collinear collision. This coefficient is given by the ratio of the relative velocity of the particles before and after collision [19],

$$e_n = \frac{\dot{\delta}_{ij}(t_c)}{\dot{\delta}_{ij}(0)} = \frac{u_0 \exp(-\eta t_c)}{u_0} = \exp(-\eta t_c), \quad (2.37)$$

and describes the momentum loss due to one collision.

2.2 Derivation of shallow granular flow equations

This section shows the derivation of shallow granular flow equations, starting from an arbitrary finite volume, also known as the control volume. The changes in some quantity $F(t)$ are considered resulting in Reynolds transport theorem (§2.2.1), which is used to derive Cauchy's equations for mass (§2.2.2) and momentum (§2.2.3). From this point on, further assumptions (§2.2.4) are made resulting in a set of partial differential equations which are subject to several boundary conditions (§2.2.5). Both, the set of partial differential equations and the boundary conditions are scaled (§2.2.6) and depth averaged (§2.2.7) resulting in the depth-averaged shallow granular flow equations. The resulting set of equations consist of several variables which need a mathematical description before the system of equations can be solved. These descriptions are the so-called closure relations and shown in §2.2.8. The section concludes with the jump conditions (§2.2.9) which are needed in order to solve discontinuities in the system.

2.2.1 Reynolds transport theorem

Consider the control volume as shown in figure 2.3, showing an arbitrary finite volume, $V(t)$, which is part of a certain flow in a cartesian coordinate system, $\{x, y, z\}$. This flow is bounded by a fixed base, $b(x, y, t)$, for example an inclined plate and a free surface, $s(x, y, t)$. Underlined variables in this figure indicate vectors in three-dimensional space $\{x, y, z\}$ e.g. the velocity at which the volume is moving is stated as $\underline{u} = \{u, v, w\}$. Furthermore, $\underline{u}_{\partial V}(\underline{x}, t)$, denotes the velocity of the boundary and is a function of place and time. The volume is enclosed by the boundary $S(\underline{x})$ and has an outward unit normal vector perpendicular to this boundary which is denoted as \underline{n} . The cartesian coordinate system is chosen such that the x direction is aligned with and the z direction aligned perpendicular to the base of the system allowing for a curve-linear coordinate system along the base of the plate. The gravity vector makes an angle ζ with the z axis and it is perpendicular to the y axis. It is assumed that the flow can be considered as a continuum, which implies that the Knudsen number must satisfy equation (2.38) with λ as the distance travelled by a particle in-between two collisions and L is a typical length scale of the system such as the funnel diameter,

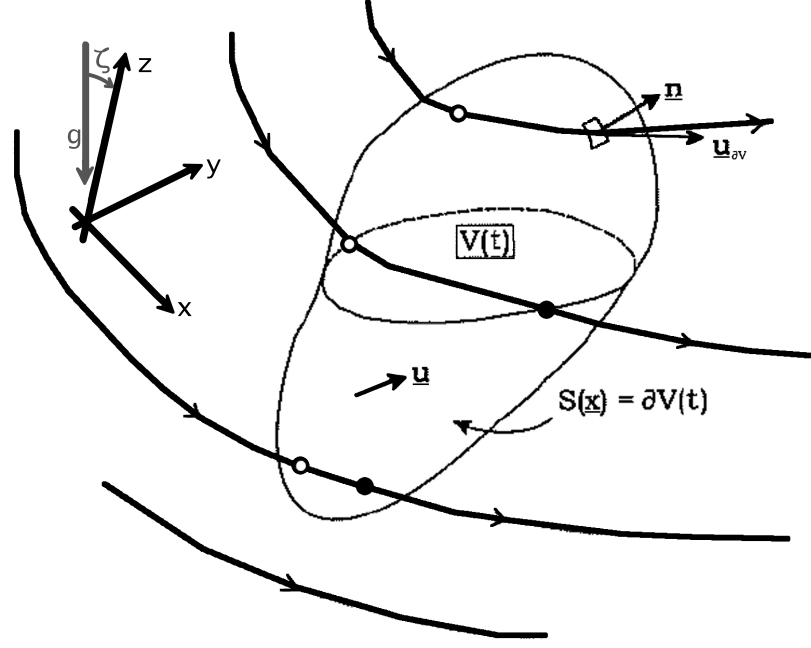
$$Kn = \frac{\lambda}{L} \ll 1, \quad (2.38)$$

Consider $F(t)$ being the total amount of some quantity $f(\underline{x}, t)$ within the control volume

$$F(t) = \iiint_V f(\underline{x}, t) dV, \quad (2.39)$$

having $[\mathcal{F}]$ as units. It is assumed that this quantity f and its time derivative ($\partial f / \partial t$) are continuous within the control volume. The quantity is allowed to change over time due to three effects:

1. Volumetric sinks or sources, S_f , in the control volume $[\mathcal{F}m^{-3}s^{-1}]$;
2. Phenomena acting at the surface, ∂V , resulting in a flux vector, \underline{J}_f , over this boundary $[\mathcal{F}m^{-2}/s^{-1}]$;

Figure 2.3: The control volume, $V(t)$, enclosed by $S(\underline{x})$ [15]

3. Inflow of the quantity through the boundary, ∂V , of the volume.

Therefore, the total amount of $f(\underline{x}, t + \Delta t)$ can be written as,

$$F(t + \Delta t) = F(t) + \int_t^{t+\Delta t} \left[\iiint_V S_f dV - \iint_{\partial V} \underline{J}_f \cdot \underline{n} dS - \iint_{\partial V} f(\underline{x}, t') [\underline{u} - \underline{u}_{\partial V}] \cdot \underline{n} dS \right] dt', \quad (2.40)$$

and rewritten in the general form of a difference quotient (left hand side) and the mean value theorem (right hand side):

$$\frac{F(t + \Delta t) - F(t)}{\Delta t} = \frac{1}{\Delta t} \int_t^{t+\Delta t} \left[\iiint_V S_f dV - \iint_{\partial V} \underline{J}_f \cdot \underline{n} dS - \iint_{\partial V} f(\underline{x}, t') [\underline{u} - \underline{u}_{\partial V}] \cdot \underline{n} dS \right] dt', \quad (2.41)$$

where the mean value theorem is stated as,

$$\frac{1}{\Delta t} \int_t^{t+\Delta t} f(\underline{x}, t') dt' = f(\underline{x}, t + \gamma \Delta t) \text{ with } 0 \leq \gamma \leq 1. \quad (2.42)$$

Taking the limit of $\Delta t \rightarrow 0$, inserting equation (2.39) and bringing the inflow term to the left hand side results in Reynolds transport theorem under the assumption that the integrands are integrable and stating,

$$\frac{\partial}{\partial t} \iiint_V f(\underline{x}, t) dV + \iint_{\partial V} f(\underline{x}, t) [\underline{u} - \underline{u}_{\partial V}] \cdot \underline{n} dS = \iiint_V S_f dV - \iint_{\partial V} \underline{J}_f \cdot \underline{n} dS. \quad (2.43)$$

2.2.2 Conservation of mass

Conservation of mass is achieved by setting $f(\underline{x}, t)$ to $\rho(\underline{x}, t)$ in equation (2.43) and assuming that there are no volumetric sources of mass in V nor diffusion of mass across ∂V . This implies that both S_f and \underline{J}_f are equal to zero and that the units of the equation are kg s^{-1} , resulting in

$$\frac{\partial}{\partial t} \iiint_V \rho dV + \iint_{\partial V} \rho [\underline{u} - \underline{u}_{\partial V}] \cdot \underline{n} dS = 0. \quad (2.44)$$

Analysis of the resulting equation (2.44) is done with the use of Leibniz's rule (2.45) and the Gauss' Divergence theorem (2.46) under the assumption that the general quantity, A , is replaced by an integrable continuous function with continuous time derivative within the control volume.

$$\frac{\partial}{\partial t} \iiint_V A \, dV = \iiint_V \frac{\partial A}{\partial t} \, dV + \iint_{\partial V} A \underline{u}_{\partial V} \cdot \underline{n} \, dS, \quad (2.45)$$

$$\iint_{\partial V} \underline{A} \cdot \underline{n} \, dS = \iiint_V \underline{\nabla} \cdot \underline{A} \, dV. \quad (2.46)$$

Applying Leibniz's rule to the first term of eq. (2.44) yields,

$$\frac{\partial}{\partial t} \iiint_V \rho \, dV = \iiint_V \frac{\partial \rho}{\partial t} \, dV + \iint_{\partial V} \rho \underline{u}_{\partial V} \cdot \underline{n} \, dS. \quad (2.47)$$

Canceling out the moving of the boundary in the surface integral in eq. (2.44), resulting in,

$$\iiint_V \frac{\partial \rho}{\partial t} \, dV + \iint_{\partial V} \rho \underline{u} \cdot \underline{n} \, dS = 0. \quad (2.48)$$

Applying Gauss' Divergence theorem (2.46) to the surface integral in (2.48) yields,

$$\iint_{\partial V} \rho \underline{u} \cdot \underline{n} \, dS = \iiint_V \underline{\nabla} \cdot \rho \underline{u} \, dV. \quad (2.49)$$

Allowing the gathering of both terms in one integral,

$$\iiint_V \frac{\partial \rho}{\partial t} + \underline{\nabla} \cdot \rho \underline{u} \, dV = 0. \quad (2.50)$$

Note that the control volume, V , was chosen arbitrarily. This implies that the integral can only be zero if the integrand itself is zero for any point in the volume, and thus stating,

$$\frac{\partial \rho}{\partial t} + \underline{\nabla} \cdot \rho \underline{u} = 0. \quad (2.51)$$

This formulation is only valid if each term in (2.51) exists. Use the definition of the material derivative,

$$\frac{D}{Dt}(\cdot) \equiv \frac{\partial}{\partial t}(\cdot) + \underline{u} \cdot \underline{\nabla}(\cdot), \quad (2.52)$$

to get Cauchy's equation (eq. (2.53)) for mass,

$$\begin{aligned} \frac{\partial \rho}{\partial t} + \underline{\nabla} \cdot \rho \underline{u} &= \frac{\partial \rho}{\partial t} + \rho \underline{\nabla} \cdot \underline{u} + \underline{u} \cdot \underline{\nabla} \rho, \\ &= \frac{D\rho}{Dt} + \rho (\underline{\nabla} \cdot \underline{u}), \\ \frac{D\rho}{Dt} + \rho (\underline{\nabla} \cdot \underline{u}) &= 0. \end{aligned} \quad (2.53)$$

2.2.3 Conservation of momentum

Conservation of momentum is derived by replacing f in equation (2.43) with the momentum vector $\rho \underline{u}$,

$$\frac{\partial}{\partial t} \iiint_V \rho \underline{u} \, dV + \iint_{\partial V} \rho \underline{u} [\underline{u} - \underline{u}_{\partial V}] \cdot \underline{n} \, dS = \iiint_V S_f \, dV - \iint_{\partial V} \underline{J}_f \cdot \underline{n} \, dS, \quad (2.54)$$

where the units of this equation are Newton. Therefore, the right hand side terms should represent volumetric and surface forces yielding,

$$\frac{\partial}{\partial t} \iiint_V \rho \underline{u} \, dV + \iint_{\partial V} \rho \underline{u} [\underline{u} - \underline{u}_{\partial V}] \cdot \underline{n} \, dS = \iiint_V \rho \underline{B} \, dV + \iint_{\partial V} \underline{\underline{\sigma}} \cdot \underline{n} \, dS, \quad (2.55)$$

in which \underline{B} is an acceleration vector and $\underline{\underline{\sigma}}$ the symmetric stress tensor consisting of a hydrostatic and a deviatoric part. Applying Leibniz's rule (2.45) on the first in (2.55) term yields,

$$\frac{\partial}{\partial t} \iiint_V \rho \underline{u} \, dV = \iiint_V \frac{\partial(\rho \underline{u})}{\partial t} \, dV + \iint_{\partial V} \rho \underline{u} \underline{u}_{\partial V} \cdot \underline{n} \, dS, \quad (2.56)$$

cancelling out the moving of the boundary in the second term of eq. (2.55). Applying Gauss's Divergence theorem (2.46) to both of the surface integrals in (2.55),

$$\iint_{\partial V} \rho \underline{u} \cdot \underline{n} \, dS = \iiint_V \underline{\nabla} \cdot (\rho \underline{u}) \, dV, \quad (2.57)$$

$$\iint_{\partial V} \underline{\sigma} \cdot \underline{n} \, dS = \iiint_V \underline{\nabla} \cdot \underline{\sigma} \, dV, \quad (2.58)$$

allows the gathering of all left hand side terms in one integral and all right hand side terms in one integral, resulting in the weak formulation of conservation of momentum:

$$\iiint_V \frac{\partial(\rho \underline{u})}{\partial t} + \underline{\nabla} \cdot (\rho \underline{u}) \, dV = \iiint_V \rho \underline{B} + \underline{\nabla} \cdot \underline{\sigma} \, dV. \quad (2.59)$$

Note that an arbitrarily control volume, V , was chosen, implying that the integral can only be zero if the integrand itself is zero for any point in the volume and therefore resulting in,

$$\frac{\partial(\rho \underline{u})}{\partial t} + \underline{\nabla} \cdot (\rho \underline{u}) = \rho \underline{B} + \underline{\nabla} \cdot \underline{\sigma}, \quad (2.60)$$

which is only valid if each individual term exist. This equation can be expanded, with the use of the product rule, in,

$$\frac{\partial(\rho \underline{u})}{\partial t} + \underline{u} \underline{\nabla} \cdot (\rho \underline{u}) + \rho \underline{u} \cdot \underline{\nabla} \underline{u} = \rho \underline{B} + \underline{\nabla} \cdot \underline{\sigma}, \quad (2.61)$$

and, with the use of the definition of the material derivative (2.52), combined to,

$$\frac{D(\rho \underline{u})}{Dt} + \rho \underline{u} \cdot \underline{\nabla} \underline{u} = \rho \underline{B} + \underline{\nabla} \cdot \underline{\sigma}. \quad (2.62)$$

Cauchy's equation for mass (2.53) multiplied with \underline{u} ,

$$\underline{u} \frac{D\rho}{Dt} = -\rho \underline{u} \underline{\nabla} \cdot \underline{u}, \quad (2.63)$$

is used to reduce equation (2.62) and yields Cauchy's equations for momentum (2.64),

$$\rho \frac{D\underline{u}}{Dt} = \rho \underline{B} + \underline{\nabla} \cdot \underline{\sigma}. \quad (2.64)$$

2.2.4 Further assumptions

With Cauchy's equations for mass (2.53) and momentum (2.64) at hand, further assumptions can be made to obtain a simpler set of equations for the volume described in figure 2.3. Therefore, the fluidized granular material is assumed to be incompressible (2.65) and homogeneous (2.66) resulting in a constant density ρ ,

$$\frac{D\rho}{Dt} = 0, \quad (2.65)$$

$$\underline{\nabla} \rho = 0. \quad (2.66)$$

Furthermore, the only body force acting is assumed to be gravity allowing the writing of \underline{B} as,

$$\underline{B} = (g \sin \zeta, 0, -g \cos \zeta)^T, \quad (2.67)$$

in which g is the gravitational constant and ζ as defined in figure 2.3. As stated in section 2.2.3, the stress tensor is symmetric and consists of a hydrostatic and deviatoric part and is therefore of the form,

$$\underline{\sigma} = -p \underline{I} + \underline{\sigma}_{Dev}, \quad (2.68)$$

in which p is the hydrostatic pressure, \underline{I} the identity matrix and $\underline{\sigma}_{Dev}$ has six individual components: σ_{xx} , σ_{yy} , σ_{zz} , σ_{xy} , σ_{xz} and σ_{yz} resulting from the conservation of angular momentum. The incompressible assumption reduces Cauchy's equation for mass to,

$$\frac{D\rho}{Dt} + \rho (\underline{\nabla} \cdot \underline{u}) = \rho (\underline{\nabla} \cdot \underline{u}), \quad (2.69)$$

which is equivalent with,

$$\nabla \cdot \underline{u} = \frac{\partial u}{\partial x} + \frac{\partial v}{\partial y} + \frac{\partial w}{\partial z} = 0. \quad (2.70)$$

Note that the vector notation changed to term-wise notation. Applying this notation change to Cauchy's equations for momentum yields,

$$\begin{aligned} \rho \left(\frac{\partial u}{\partial t} + u \frac{\partial u}{\partial x} + v \frac{\partial u}{\partial y} + w \frac{\partial u}{\partial z} \right) &= \rho g \sin \zeta + \frac{\partial \sigma_{xx}}{\partial x} + \frac{\partial \sigma_{xy}}{\partial y} + \frac{\partial \sigma_{xz}}{\partial z} - \frac{\partial p}{\partial x}, \\ \rho \left(\frac{\partial v}{\partial t} + u \frac{\partial v}{\partial x} + v \frac{\partial v}{\partial y} + w \frac{\partial v}{\partial z} \right) &= \frac{\partial \sigma_{xy}}{\partial x} + \frac{\partial \sigma_{yy}}{\partial y} + \frac{\partial \sigma_{yz}}{\partial z} - \frac{\partial p}{\partial y}, \\ \rho \left(\frac{\partial w}{\partial t} + u \frac{\partial w}{\partial x} + v \frac{\partial w}{\partial y} + w \frac{\partial w}{\partial z} \right) &= -\rho g \cos \zeta + \frac{\partial \sigma_{xz}}{\partial x} + \frac{\partial \sigma_{yz}}{\partial y} + \frac{\partial \sigma_{zz}}{\partial z} - \frac{\partial p}{\partial z}. \end{aligned} \quad (2.71)$$

These equations can be rewritten with the use equation (2.70) and the chain rule to,

$$\begin{aligned} \rho \left(\frac{\partial u}{\partial t} + \frac{\partial u^2}{\partial x} + \frac{\partial}{\partial y}(uv) + \frac{\partial}{\partial z}(uw) \right) &= \rho g \sin \zeta + \frac{\partial \sigma_{xx}}{\partial x} + \frac{\partial \sigma_{xy}}{\partial y} + \frac{\partial \sigma_{xz}}{\partial z} - \frac{\partial p}{\partial x}, \\ \rho \left(\frac{\partial v}{\partial t} + \frac{\partial}{\partial x}(uv) + \frac{\partial v^2}{\partial y} + \frac{\partial}{\partial z}(vw) \right) &= \frac{\partial \sigma_{xy}}{\partial x} + \frac{\partial \sigma_{yy}}{\partial y} + \frac{\partial \sigma_{yz}}{\partial z} - \frac{\partial p}{\partial y}, \\ \rho \left(\frac{\partial w}{\partial t} + \frac{\partial}{\partial x}(uw) + \frac{\partial}{\partial y}(vw) + \frac{\partial w^2}{\partial z} \right) &= -\rho g \cos \zeta + \frac{\partial \sigma_{xz}}{\partial x} + \frac{\partial \sigma_{yz}}{\partial y} + \frac{\partial \sigma_{zz}}{\partial z} - \frac{\partial p}{\partial z}. \end{aligned} \quad (2.72)$$

2.2.5 Boundary conditions

As described in section 2.2.1, the flow is bounded by free and basal surfaces. These surfaces must satisfy $z - s(x, y, t) = 0$ and $b(x, y, t) - z = 0$ in which the coordinate z is the height of the flow, perpendicular to the base. The boundaries are assumed to be impermeable. Therefore, the kinematic boundary conditions must hold at those surfaces,

$$\frac{D(s - z)}{Dt} = \frac{\partial s}{\partial t} + u^s \frac{\partial s}{\partial x} + v^s \frac{\partial s}{\partial y} - w^s = 0, \quad (2.73)$$

$$\frac{D(b - z)}{Dt} = \frac{\partial b}{\partial t} + u^b \frac{\partial b}{\partial x} + v^b \frac{\partial b}{\partial y} - w^b = 0, \quad (2.74)$$

in which the superscripts denote evaluation at the respective surface. The outward unit normals, \underline{n}^s and \underline{n}^b , are defined as,

$$\underline{n}^s \equiv \frac{\underline{n}^{s*}}{\Delta^s} \text{ with } \underline{n}^{s*} = \left\{ -\frac{\partial s}{\partial x}, -\frac{\partial s}{\partial y}, 1 \right\} \text{ and } \Delta^s \equiv \|\underline{n}^{s*}\|, \quad (2.75)$$

$$\underline{n}^b \equiv \frac{\underline{n}^{b*}}{\Delta^b} \text{ with } \underline{n}^{b*} = \left\{ \frac{\partial b}{\partial x}, \frac{\partial b}{\partial y}, -1 \right\} \text{ and } \Delta^b \equiv \|\underline{n}^{b*}\|. \quad (2.76)$$

Applying a traction-free condition at the free surface and assuming a Coulomb friction model for the basal surface implies,

$$\underline{\underline{\sigma}}^s \underline{n}^s = 0, \quad (2.77)$$

$$\underline{\underline{\sigma}}^b \underline{n}^b = \underline{t}^b, \quad (2.78)$$

in which the traction at the bottom, \underline{t}^b , can be decomposed in a tangential and normal part,

$$\underline{t}^b = \underline{t}_t^b + \underline{t}_n^b, \quad (2.79)$$

where the tangential part satisfies Coulomb friction law and the normal part acts in opposite direction with respect to the basal normal, \underline{n}^b , yielding,

$$\underline{t}_t^b = -\mu \|\underline{t}_n^b\| \frac{\underline{u}}{\|\underline{u}\|}, \quad (2.80)$$

$$\underline{t}_n^b = -\underline{n}^b \|\underline{t}_n^b\|. \quad (2.81)$$

Substitution of (2.81) into (2.79) and taking the dot product between the resulting equation and the basal normal yields,

$$\begin{aligned} -\underline{n}^b \underline{t}^b &= -\underline{n}^b \left[\underline{t}_t^b - \underline{n}^b \|\underline{t}_n^b\| \right], \\ -\underline{n}^b \underline{t}^b &= \|\underline{t}_n^b\|, \end{aligned} \quad (2.82)$$

allowing the writing of,

$$\|\underline{t}_n^b\| = -\underline{n}^b \cdot (\underline{\sigma}^b \underline{n}^b). \quad (2.83)$$

Combining equations (2.78)-(2.81) and (2.83) results in the traction boundary condition at the basal surface,

$$\underline{\sigma}^b \underline{n}^b = (\underline{n}^b \cdot \underline{\sigma}^b \underline{n}^b) \left(\mu \frac{\underline{u}^b}{\|\underline{u}^b\|} + \underline{n}^b \right). \quad (2.84)$$

2.2.6 Dimensionless form

The obtained conservation equations (2.70), (2.72) and the boundary conditions (2.73), (2.74), (2.77) and (2.84) are scaled with the use of the gravitational constant, g , and the flow depth, H , length, L , and density, ρ . This allows the writing of a dimensionless aspect ratio $\varepsilon = H/L$ assuming $H \ll L$ and thus simplification of the equations. The rescaling of the variables is done with the following set of equations,

$$\begin{aligned} \{x, y, z\} &= L\{\hat{x}, \hat{y}, \varepsilon \hat{z}\}, & p &= \rho g H \hat{p}, \\ \{u, v, w\} &= \sqrt{gL}\{\hat{u}, \hat{v}, \varepsilon \hat{w}\}, & \{\sigma_{xy}, \sigma_{xz}, \sigma_{yz}\} &= \varepsilon^\gamma \rho g H \{\hat{\sigma}_{xy}, \hat{\sigma}_{xz}, \hat{\sigma}_{yz}\}, \\ t &= \sqrt{L/g} \hat{t}, & \{\sigma_{xx}, \sigma_{yy}, \sigma_{zz}\} &= \rho g H \{\hat{\sigma}_{xx}, \hat{\sigma}_{yy}, \hat{\sigma}_{zz}\}, \end{aligned} \quad (2.85)$$

following the scalings as proposed in Bokhove and Thornton [1] extended in three dimensions with the use of the scalings in Gray *et. al.* [12]. Variables with a hat denote dimensionless variables and γ is a scaling factor in the range $(0, 1)$. Applying this set of dimensionless forms to equation (2.70) yields,

$$\begin{aligned} \frac{\partial u}{\partial x} + \frac{\partial v}{\partial y} + \frac{\partial w}{\partial z} &= \frac{\sqrt{gL}}{L} \left(\frac{\partial \hat{u}}{\partial \hat{x}} + \frac{\partial \hat{v}}{\partial \hat{y}} \right) + \frac{\varepsilon \sqrt{gL}}{H} \frac{\partial \hat{w}}{\partial \hat{z}} \\ &= \frac{\sqrt{gL}}{L} \left(\frac{\partial \hat{u}}{\partial \hat{x}} + \frac{\partial \hat{v}}{\partial \hat{y}} + \frac{\partial \hat{w}}{\partial \hat{z}} \right) \\ &= \frac{\partial \hat{u}}{\partial \hat{x}} + \frac{\partial \hat{v}}{\partial \hat{y}} + \frac{\partial \hat{w}}{\partial \hat{z}} = 0. \end{aligned} \quad (2.86)$$

Following the same analogy to achieve the dimensionless form of the conservation of momentum results, after division by ρg , in,

$$\begin{aligned} \frac{\partial \hat{u}}{\partial \hat{t}} + \frac{\partial \hat{u}^2}{\partial \hat{x}} + \frac{\partial}{\partial \hat{y}}(\hat{u}\hat{v}) + \frac{\partial}{\partial \hat{z}}(\hat{u}\hat{w}) &= \sin \zeta + \varepsilon \frac{\partial \hat{\sigma}_{xx}}{\partial \hat{x}} + \varepsilon^{\gamma+1} \frac{\partial \hat{\sigma}_{xy}}{\partial \hat{y}} + \varepsilon^\gamma \frac{\partial \hat{\sigma}_{xz}}{\partial \hat{z}} - \varepsilon \frac{\partial \hat{p}}{\partial \hat{x}}, \\ \frac{\partial \hat{v}}{\partial \hat{t}} + \frac{\partial}{\partial \hat{x}}(\hat{u}\hat{v}) + \frac{\partial \hat{v}^2}{\partial \hat{y}} + \frac{\partial}{\partial \hat{z}}(\hat{v}\hat{w}) &= \varepsilon^{\gamma+1} \frac{\partial \hat{\sigma}_{xy}}{\partial \hat{x}} + \varepsilon \frac{\partial \hat{\sigma}_{yy}}{\partial \hat{y}} + \varepsilon^\gamma \frac{\partial \hat{\sigma}_{yz}}{\partial \hat{z}} - \varepsilon \frac{\partial \hat{p}}{\partial \hat{y}}, \\ \varepsilon \left(\frac{\partial \hat{w}}{\partial \hat{t}} + \frac{\partial}{\partial \hat{x}}(\hat{u}\hat{w}) + \frac{\partial}{\partial \hat{y}}(\hat{v}\hat{w}) + \frac{\partial \hat{w}^2}{\partial \hat{z}} \right) &= -\cos \zeta + \varepsilon^{\gamma+1} \frac{\partial \hat{\sigma}_{xz}}{\partial \hat{x}} + \varepsilon^{\gamma+1} \frac{\partial \hat{\sigma}_{yz}}{\partial \hat{y}} + \frac{\partial \hat{\sigma}_{zz}}{\partial \hat{z}} - \frac{\partial \hat{p}}{\partial \hat{z}}. \end{aligned} \quad (2.87)$$

Applying the scaling for the free, s , and basal, b , surface coordinates,

$$s(x, y, t) = H \hat{s}(\hat{x}, \hat{y}, \hat{t}), \quad b(x, y, t) = H \hat{b}(\hat{x}, \hat{y}, \hat{t}), \quad (2.88)$$

rewriting the outward normal vectors,

$$\hat{\underline{n}}^s = \frac{\hat{\underline{n}}^{s*}}{\hat{\Delta}^s} \text{ with } \hat{\underline{n}}^{s*} = \left\{ -\varepsilon \frac{\partial \hat{s}}{\partial \hat{x}}, -\varepsilon \frac{\partial \hat{s}}{\partial \hat{y}}, 1 \right\} \text{ and } \hat{\Delta}^s = \|\hat{\underline{n}}^{s*}\|, \quad (2.89)$$

$$\hat{\underline{n}}^b = \frac{\hat{\underline{n}}^{b*}}{\hat{\Delta}^b} \text{ with } \hat{\underline{n}}^{b*} = \left\{ \varepsilon \frac{\partial \hat{b}}{\partial \hat{x}}, \varepsilon \frac{\partial \hat{b}}{\partial \hat{y}}, -1 \right\} \text{ and } \hat{\Delta}^b = \|\hat{\underline{n}}^{b*}\|, \quad (2.90)$$

defining the dimensionless stress tensor,

$$\underline{\hat{\sigma}} = \begin{bmatrix} \hat{\sigma}_{xx} - \hat{p} & \varepsilon^\gamma \hat{\sigma}_{xy} & \varepsilon^\gamma \hat{\sigma}_{xz} \\ \varepsilon^\gamma \hat{\sigma}_{xy} & \hat{\sigma}_{yy} - \hat{p} & \varepsilon^\gamma \hat{\sigma}_{yz} \\ \varepsilon^\gamma \hat{\sigma}_{xz} & \varepsilon^\gamma \hat{\sigma}_{yz} & \hat{\sigma}_{zz} - \hat{p} \end{bmatrix} \quad (2.91)$$

and the dimensionless friction term in equation (2.84),

$$\mu \frac{\underline{u}^b}{\|\underline{u}^b\|} = \mu \frac{\underline{\hat{u}}^b}{\|\underline{\hat{u}}^b\|}, \quad (2.92)$$

allows the scaling of the boundary conditions. The free surface conditions then becomes (2.73), (2.77),

$$\frac{D(s-z)}{Dt} = \frac{\partial \hat{s}}{\partial \hat{t}} + \hat{u}^s \frac{\partial \hat{s}}{\partial \hat{x}} + \hat{v}^s \frac{\partial \hat{s}}{\partial \hat{y}} - \hat{w}^s = 0, \quad (2.93)$$

$$\begin{aligned} -\varepsilon (\hat{\sigma}_{xx}^s - \hat{p}^s) \frac{\partial \hat{s}}{\partial \hat{x}} - \varepsilon^{\gamma+1} \hat{\sigma}_{xy}^s \frac{\partial \hat{s}}{\partial \hat{y}} + \varepsilon^\gamma \hat{\sigma}_{xz}^s &= 0, \\ -\varepsilon^{\gamma+1} \hat{\sigma}_{xy}^s \frac{\partial \hat{s}}{\partial \hat{x}} - \varepsilon (\hat{\sigma}_{yy}^s - \hat{p}^s) \frac{\partial \hat{s}}{\partial \hat{y}} + \varepsilon^\gamma \hat{\sigma}_{yz}^s &= 0, \\ -\varepsilon^{\gamma+1} \hat{\sigma}_{xz}^s \frac{\partial \hat{s}}{\partial \hat{x}} - \varepsilon^{\gamma+1} \hat{\sigma}_{yz}^s \frac{\partial \hat{s}}{\partial \hat{y}} + \hat{\sigma}_{zz}^s - \hat{p}^s &= 0, \end{aligned} \quad (2.94)$$

and the basal conditions (2.74), (2.84),

$$\frac{D(b-z)}{Dt} = \frac{\partial \hat{b}}{\partial \hat{t}} + \hat{u}^b \frac{\partial \hat{b}}{\partial \hat{x}} + \hat{v}^b \frac{\partial \hat{b}}{\partial \hat{y}} - \hat{w}^b = 0, \quad (2.95)$$

$$\begin{aligned} \varepsilon (\hat{\sigma}_{xx}^b - \hat{p}^b) \frac{\partial \hat{b}}{\partial \hat{x}} + \varepsilon^{\gamma+1} \hat{\sigma}_{xy}^b \frac{\partial \hat{b}}{\partial \hat{y}} - \varepsilon^\gamma \hat{\sigma}_{xz}^b &= \left(\hat{\underline{n}}^b \cdot \underline{\hat{\sigma}}^b \hat{\underline{n}}^b \right) \left(\hat{\Delta}^b \mu \frac{\hat{u}^b}{\|\hat{\underline{u}}^b\|} + \varepsilon \frac{\partial \hat{b}}{\partial \hat{x}} \right), \\ \varepsilon^{\gamma+1} \hat{\sigma}_{xy}^b \frac{\partial \hat{b}}{\partial \hat{x}} + \varepsilon (\hat{\sigma}_{yy}^b - \hat{p}^b) \frac{\partial \hat{b}}{\partial \hat{y}} - \varepsilon^\gamma \hat{\sigma}_{yz}^b &= \left(\hat{\underline{n}}^b \cdot \underline{\hat{\sigma}}^b \hat{\underline{n}}^b \right) \left(\hat{\Delta}^b \mu \frac{\hat{v}^b}{\|\hat{\underline{u}}^b\|} + \varepsilon \frac{\partial \hat{b}}{\partial \hat{y}} \right), \\ \varepsilon^{\gamma+1} \hat{\sigma}_{xz}^b \frac{\partial \hat{b}}{\partial \hat{x}} + \varepsilon^{\gamma+1} \hat{\sigma}_{yz}^b \frac{\partial \hat{b}}{\partial \hat{y}} - (\hat{\sigma}_{zz}^b - \hat{p}^b) &= \left(\hat{\underline{n}}^b \cdot \underline{\hat{\sigma}}^b \hat{\underline{n}}^b \right) \left(\hat{\Delta}^b \mu \frac{\varepsilon \hat{w}^b}{\|\hat{\underline{u}}^b\|} - 1 \right). \end{aligned} \quad (2.96)$$

2.2.7 Depth-averaged modelling

The spatial coordinate perpendicular to the base, z , is integrated out of the non-dimensional mass (2.86) and momentum equations (2.87) when these are depth-averaged. To do so, a depth-averaged variable, \bar{f} , is defined as,

$$\bar{f} = \frac{1}{h} \int_b^s f(z) dz \quad \text{with } h = s - b. \quad (2.97)$$

Note that the hats are omitted from this point on. Furthermore, the general form of Leibniz rule is needed in the depth-averaging of the mass and momentum equations and is given by (2.98). It requires that both f and its derivative in α are continuous on the interval $[a(\alpha), b(\alpha)]$,

$$\frac{\partial}{\partial \alpha} \int_{a(\alpha)}^{b(\alpha)} f(z, \alpha) dz = \frac{\partial b(\alpha)}{\partial \alpha} f(b(\alpha), \alpha) - \frac{\partial a(\alpha)}{\partial \alpha} f(a(\alpha), \alpha) + \int_{a(\alpha)}^{b(\alpha)} \frac{\partial f(z, \alpha)}{\partial \alpha} dz, \quad (2.98)$$

It defines the differential of an integral when the boundaries, a and b , as well as the function, f , depend on the same variable α . Term wise integration over the dimensionless depth, z , of the dimensionless mass equation, applying Leibniz rule to the first two integrals, using the dimensionless kinematic

boundary conditions (2.93), (2.95) and introduction of the, on equation (2.97) based, depth-averaged variables \bar{u} and \bar{v} yields,

$$\begin{aligned} \int_b^s \frac{\partial u}{\partial x} + \frac{\partial v}{\partial y} + \frac{\partial w}{\partial z} dz &= \int_b^s \frac{\partial u}{\partial x} dz + \int_b^s \frac{\partial v}{\partial y} dz + \int_b^s \frac{\partial w}{\partial z} dz \\ &= \frac{\partial}{\partial x} \int_b^s u dz - \frac{\partial s}{\partial x} u^s + \frac{\partial b}{\partial x} u^b + \frac{\partial}{\partial y} \int_b^s v dz - \frac{\partial s}{\partial y} v^s + \frac{\partial b}{\partial y} v^b + w^s - w^b \\ &= \frac{\partial h}{\partial t} + \frac{\partial}{\partial x} (h\bar{u}) + \frac{\partial}{\partial y} (h\bar{v}) = 0, \end{aligned} \quad (2.99)$$

which is the depth-averaged mass equation. Depth-averaging the momentum equations is done in a similar way resulting in,

$$\begin{aligned} \frac{\partial}{\partial t} (h\bar{u}) + \frac{\partial}{\partial x} (h\bar{u}^2) + \frac{\partial}{\partial y} (h\bar{u}\bar{v}) - \left[u \left(\frac{\partial z}{\partial t} + u \frac{\partial z}{\partial x} + v \frac{\partial z}{\partial y} - w \right) \right]_b^s = \\ h \sin \zeta + \varepsilon \frac{\partial}{\partial x} (h(\bar{\sigma}_{xx} - \bar{p})) + \varepsilon^{\gamma+1} \frac{\partial}{\partial y} (h\bar{\sigma}_{xy}) - \left[\varepsilon \frac{\partial z}{\partial x} (\sigma_{xx} - p) + \varepsilon^{\gamma+1} \frac{\partial z}{\partial y} \sigma_{xy} - \varepsilon^\gamma \sigma_{xz} \right]_b^s, \end{aligned} \quad (2.100)$$

for the momentum equation in x direction, and,

$$\begin{aligned} \frac{\partial}{\partial t} (h\bar{v}) + \frac{\partial}{\partial x} (h\bar{u}\bar{v}) + \frac{\partial}{\partial y} (h\bar{v}^2) - \left[v \left(\frac{\partial z}{\partial t} + u \frac{\partial z}{\partial x} + v \frac{\partial z}{\partial y} - w \right) \right]_b^s = \\ \varepsilon^{\gamma+1} \frac{\partial}{\partial x} (h\bar{\sigma}_{xy}) + \varepsilon \frac{\partial}{\partial y} (h(\bar{\sigma}_{yy} - \bar{p})) - \left[\varepsilon^{\gamma+1} \frac{\partial z}{\partial x} \sigma_{xy} + \varepsilon \frac{\partial z}{\partial y} (\sigma_{yy} - p) - \varepsilon^\gamma \sigma_{yz} \right]_b^s, \end{aligned} \quad (2.101)$$

for the momentum equation in y direction. Substitution of the kinematic boundary conditions in the first square bracketed term and the traction boundary conditions in the last square bracketed term of equations (2.100) yields,

$$\begin{aligned} \frac{\partial}{\partial t} (h\bar{u}) + \frac{\partial}{\partial x} (h\bar{u}^2) + \frac{\partial}{\partial y} (h\bar{u}\bar{v}) = \\ h \sin \zeta + \varepsilon \frac{\partial}{\partial x} (h(\bar{\sigma}_{xx} - \bar{p})) + \varepsilon^{\gamma+1} \frac{\partial}{\partial y} (h\bar{\sigma}_{xy}) + (\underline{n}^b \cdot \underline{\underline{\sigma}}^b \underline{n}^b) \left(\mu \Delta^b \frac{u^b}{\|\underline{u}^b\|} + \varepsilon \frac{\partial b}{\partial x} \right), \end{aligned} \quad (2.102)$$

for the x direction and equivalent substitutions in the y direction lead to,

$$\begin{aligned} \frac{\partial}{\partial t} (h\bar{v}) + \frac{\partial}{\partial x} (h\bar{u}\bar{v}) + \frac{\partial}{\partial y} (h\bar{v}^2) = \\ \varepsilon^{\gamma+1} \frac{\partial}{\partial x} (h\bar{\sigma}_{xy}) + \varepsilon \frac{\partial}{\partial y} (h(\bar{\sigma}_{yy} - \bar{p})) + (\underline{n}^b \cdot \underline{\underline{\sigma}}^b \underline{n}^b) \left(\mu \Delta^b \frac{v^b}{\|\underline{u}^b\|} + \varepsilon \frac{\partial b}{\partial y} \right). \end{aligned} \quad (2.103)$$

The fact that the length of a granular flow is often much bigger than the height is not exploited at this point. This means that the fraction $\varepsilon \ll 1$ and therefore, terms of order greater than ε may be neglected. Reducing (2.102), (2.103) is allowed when $\mu = \mathcal{O}(\varepsilon^\gamma)$ is stated allowing the reduction of $\underline{n}^b \cdot \underline{\underline{\sigma}}^b \underline{n}^b$ to only the leading order terms. Consider therefore,

$$\underline{\underline{\sigma}}^b \underline{n}^b = \left\{ \begin{array}{ccc} \varepsilon \frac{\partial b}{\partial x} (\sigma_{xx}^b - p^b) & + & \varepsilon^{\gamma+1} \frac{\partial b}{\partial y} \sigma_{xy}^b & - & \varepsilon^\gamma \sigma_{xz}^b \\ \varepsilon^{\gamma+1} \frac{\partial b}{\partial x} \sigma_{xy}^b & + & \varepsilon \frac{\partial b}{\partial y} (\sigma_{yy}^b - p^b) & - & \varepsilon^\gamma \sigma_{yz}^b \\ \varepsilon^{\gamma+1} \frac{\partial b}{\partial x} \sigma_{xz}^b & + & \varepsilon^{\gamma+1} \frac{\partial b}{\partial y} \sigma_{yz}^b & - & (\sigma_{zz}^b - p^b) \end{array} \right\}, \quad (2.104)$$

and also,

$$\underline{n}^b \cdot \underline{\underline{\sigma}}^b \underline{n}^b = \sigma_{zz}^b - p^b + \mathcal{O}(\varepsilon^{\gamma+1}). \quad (2.105)$$

in which an expression for $\sigma_{zz}^b - p^b$ is still needed. This expression can be found by neglecting the $\mathcal{O}(\varepsilon)$ terms in the momentum equation in z direction,

$$\frac{\partial}{\partial z} (\sigma_{zz} - p) = \cos \zeta + \mathcal{O}(\varepsilon), \quad (2.106)$$

and integration over depth,

$$\int_b^s \frac{\partial}{\partial z} (\sigma_{zz} - p) dz = \int_b^s \cos \zeta + \mathcal{O}(\varepsilon) dz, \quad (2.107)$$

$$(\sigma_{zz}^s - p^s) - (\sigma_{zz}^b - p^b) = (s - b) \cos \zeta + \mathcal{O}(\varepsilon). \quad (2.108)$$

Note that the leading order term in the dimensionless traction condition at the free surface in z direction (2.94) is equal to $(\sigma_{zz}^s - p^s)$, implying that this term is equal to 0. Furthermore the definition of h (2.97) is implemented in (2.108), leading to,

$$\sigma_{zz}^b - p^b = -h \cos \zeta + \mathcal{O}(\varepsilon). \quad (2.109)$$

Furthermore, the basal length of the outward normal vector, Δ^b , is given by,

$$\Delta^b = \sqrt{1 + \varepsilon^2 \left(\left(\frac{\partial b}{\partial x} \right)^2 + \left(\frac{\partial b}{\partial y} \right)^2 \right)} \quad (2.110)$$

and can be expanded with a Taylor series in,

$$\Delta^b \approx 1 + \frac{1}{2} \varepsilon^2 \left(\left(\frac{\partial b}{\partial x} \right)^2 + \left(\frac{\partial b}{\partial y} \right)^2 \right) + \mathcal{O}(\varepsilon^4) \quad (2.111)$$

$$= 1 + \mathcal{O}(\varepsilon^2). \quad (2.112)$$

Combining (2.105) with (2.109) and implementation in (2.102) and (2.103) while taking (2.112) into account and neglecting terms of order $\varepsilon^{\gamma+1}$ and higher, yields,

$$\begin{aligned} \frac{\partial}{\partial t} (h\bar{u}) + \frac{\partial}{\partial x} (h\bar{u}^2) + \frac{\partial}{\partial y} (h\bar{u} \bar{v}) = \\ h \sin \zeta + \varepsilon \frac{\partial}{\partial x} (h(\bar{\sigma}_{xx} - \bar{p})) - h \cos \zeta \left(\mu \frac{u^b}{\|\underline{u}^b\|} + \varepsilon \frac{\partial b}{\partial x} \right) + \mathcal{O}(\varepsilon^{\gamma+1}), \end{aligned} \quad (2.113)$$

$$\begin{aligned} \frac{\partial}{\partial t} (h\bar{v}) + \frac{\partial}{\partial x} (h\bar{u} \bar{v}) + \frac{\partial}{\partial y} (h\bar{v}^2) = \\ \varepsilon \frac{\partial}{\partial y} (h(\bar{\sigma}_{yy} - \bar{p})) - h \cos \zeta \left(\mu \frac{v^b}{\|\underline{u}^b\|} + \varepsilon \frac{\partial b}{\partial y} \right) + \mathcal{O}(\varepsilon^{\gamma+1}). \end{aligned} \quad (2.114)$$

The equations above can be further simplified by using the Boussinesq assumption [13] which states that the tangential velocity components are independent of the depth in a first order approximation,

$$\bar{u} = u^b + \mathcal{O}(\varepsilon^{\gamma+1}), \quad \bar{v} = v^b + \mathcal{O}(\varepsilon^{\gamma+1}). \quad (2.115)$$

Furthermore, plug flow is assumed allowing for the factorization of the squared averages,

$$\overline{u^2} = \bar{u}^2 + \mathcal{O}(\varepsilon^{\gamma+1}), \quad \overline{v^2} = \bar{v}^2 + \mathcal{O}(\varepsilon^{\gamma+1}), \quad \|\underline{u}^b\| = \sqrt{\bar{u}^2 + \bar{v}^2} + \mathcal{O}(\varepsilon^{\gamma+1}) = \|\underline{u}\|. \quad (2.116)$$

The momentum equations can then be further simplified into,

$$\begin{aligned} \frac{\partial}{\partial t} (h\bar{u}) + \frac{\partial}{\partial x} (h\bar{u}^2) + \frac{\partial}{\partial y} (h\bar{u} \bar{v}) = \\ h \sin \zeta + \varepsilon \frac{\partial}{\partial x} (h(\bar{\sigma}_{xx} - \bar{p})) - h \cos \zeta \left(\mu \frac{\bar{u}}{\|\underline{u}\|} + \varepsilon \frac{\partial b}{\partial x} \right) + \mathcal{O}(\varepsilon^{\gamma+1}), \end{aligned} \quad (2.117)$$

$$\begin{aligned} \frac{\partial}{\partial t} (h\bar{v}) + \frac{\partial}{\partial x} (h\bar{u} \bar{v}) + \frac{\partial}{\partial y} (h\bar{v}^2) = \\ \varepsilon \frac{\partial}{\partial y} (h(\bar{\sigma}_{yy} - \bar{p})) - h \cos \zeta \left(\mu \frac{\bar{v}}{\|\underline{u}\|} + \varepsilon \frac{\partial b}{\partial y} \right) + \mathcal{O}(\varepsilon^{\gamma+1}). \end{aligned} \quad (2.118)$$

No assumptions are made on the stresses nor on the friction in the system. Solving the set of equations is thus still impossible. Therefore, closure relations are sought.

2.2.8 Closure relations

As stated in §2.2.7 the system of equations is still not closed; there are more unknown variables than there are equations. This section will provide constitutive relations for the friction coefficient and the stresses closing the system of equations.

Friction coefficient

The basal friction coefficient μ , which relates the normal and tangential forces on a particle is first used in the definition of the tangential traction (2.80). It is based on the assumption that a Coulomb friction law is present and thus implies that it is constant and equal to $\mu = \tan \delta$ where δ is the basal angle of friction. Experiments show that this assumption is not valid on rough beds or high inclination angles. Pouliquen [23] stated an empirical friction law which was characterized by two angles. The first is the angle at which the material comes to rest, δ_1 and a second at which the material starts to accelerate, δ_2 . The limit of $\delta_1 \rightarrow \delta_2$ results in steady flow which is equal to the original Coulomb friction law. The software used, Mercury, is not able to handle this Pouliquen friction law and therefore Coulombs model is used resulting in a friction coefficient of 0.5.

Earth pressure coefficient

Closure relations for the stresses, linking σ_{xx} and σ_{yy} to σ_{zz} together. This topic is still subject of current research [10] and, in general, there are two common routes to solve the problem. The first route follows the original Savage and Hutter paper [25], where the Mohr-Coulomb assumption made in (2.80) is extended to determine a so-called earth pressure coefficient K . It was assumed that the material behaves as a Mohr-Coulomb material at yield, implying that the stresses in normal and tangential directions in each plane are related with a Mohr-Coulomb yield criterion,

$$\tau = \sigma \tan \phi, \quad (2.119)$$

where ϕ is the internal angle of friction. This allows the construction of a Mohr's circle for plane stress situations. The earth pressure coefficient relates the limiting normal stresses in x and z directions for a two dimensional system in a linear way; $K = \sigma_{xx}/\sigma_{zz}$. This coefficient can be related to the stresses with the use of the Mohr circle. Hence [1, 10],

$$K = \frac{2 \mp 2\sqrt{1 - \frac{\cos^2 \phi}{\cos^2 \delta}}}{\cos^2 \phi} - 1, \quad (2.120)$$

with δ the basal angle of friction. The two options (\mp) refer to respectively the active and passive stress states the material can behave. The former implies that the whole material forming a heap and the latter implies that the bulk material is flowing down the plate. This approach in closing the stress relation makes rigorous assumptions, resulting in a rather complex but still inaccurate definition for the earth pressure coefficient K . Extension for a fully three dimensional granular system is also performed even lowering the accuracy of this coefficient. On the other hand, a simpler model is assumed in the second route. The flowing granular material is then assumed to behave like an inviscid fluid, implying $K = 1$ [1, 10]. It is known that this assumption also not holds but Weinhart *et. al.* [30] showed that the value for the earth pressure coefficient is approximately 1 with a small dependence on the inclination angle. Therefore, the closure relation for the pressures will be taken according to the second route, resulting in,

$$\sigma_{xx} = \sigma_{yy} = \sigma_{zz}. \quad (2.121)$$

Equations (2.117) and (2.118) can then be simplified with the use of (2.109). To do so, (2.109) is depth-averaged resulting in,

$$\bar{\sigma}_{zz} - \bar{p} = \int_b^s -h \cos \zeta + \mathcal{O}(\varepsilon) dz = -\frac{h^2}{2} \cos \zeta + \mathcal{O}(\varepsilon), \quad (2.122)$$

hence,

$$\bar{\sigma}_{xx} - \bar{p} = \bar{\sigma}_{yy} - \bar{p} = \bar{\sigma}_{zz} - \bar{p} = -\frac{h^2}{2} \cos \zeta + \mathcal{O}(\varepsilon). \quad (2.123)$$

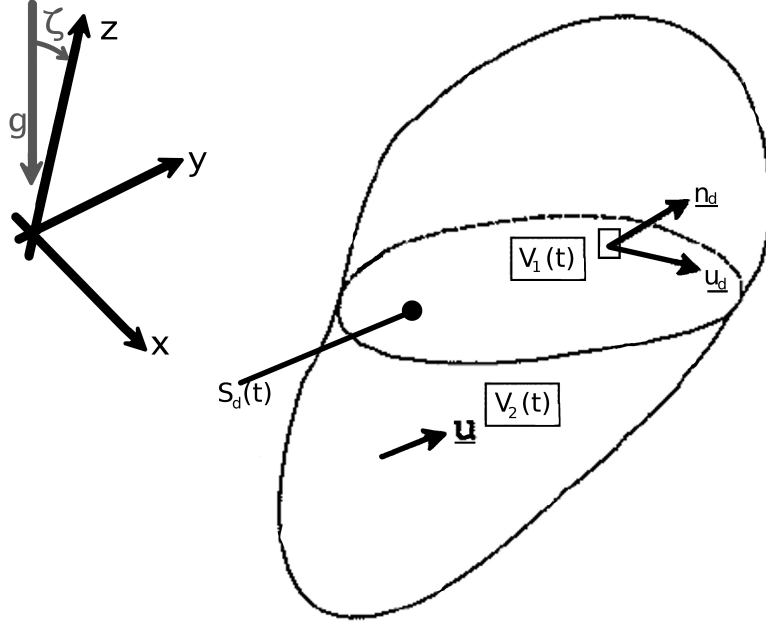


Figure 2.4: The control volume separated in two volumes V_1 and V_2 by a moving surface of discontinuity. [15]

Substitution of (2.123) into (2.117) and (2.118) while omitting the bars and higher order terms in ε yields a closed system of equations,

$$\frac{\partial}{\partial t} (hu) + \frac{\partial}{\partial x} (hu^2) + \frac{\partial}{\partial y} (huv) = h \sin \zeta - \varepsilon \cos \zeta \frac{\partial}{\partial x} \left(\frac{h^2}{2} \right) - h \cos \zeta \left(\mu \frac{u}{\|\underline{u}\|} + \varepsilon \frac{\partial b}{\partial x} \right), \quad (2.124)$$

$$\frac{\partial}{\partial t} (hv) + \frac{\partial}{\partial x} (huv) + \frac{\partial}{\partial y} (hv^2) = -\varepsilon \cos \zeta \frac{\partial}{\partial y} \left(\frac{h^2}{2} \right) - h \cos \zeta \left(\mu \frac{v}{\|\underline{u}\|} + \varepsilon \frac{\partial b}{\partial y} \right). \quad (2.125)$$

2.2.9 Jump conditions

The system of equations given by (2.99), (2.124) and (2.125) are based on the assumption that the flow is continuous and differentiable on the whole domain. At a hydraulic jump, these conditions are not met since it can be considered as an area of discontinuity. Nevertheless, jump conditions can be derived from the original set of equations. Figure 2.4 shows a fixed control volume with a moving surface of discontinuity. The integral form of the continuity equation (2.44) for the two parts of the volume is given by,

$$\begin{aligned} \frac{\partial}{\partial t} \iiint_{V_1} \rho \, dV_1 + \iint_{\partial V_1} \rho \underline{u} \cdot \underline{n} \, dS + \iint_{S_d^-} \rho (\underline{u} - \underline{u}_d) \cdot \underline{n}_d \, dS + \\ \frac{\partial}{\partial t} \iiint_{V_2} \rho \, dV_2 + \iint_{\partial V_2} \rho \underline{u} \cdot \underline{n} \, dS - \iint_{S_d^+} \rho (\underline{u} - \underline{u}_d) \cdot \underline{n}_d \, dS = 0, \end{aligned} \quad (2.126)$$

where the last term in both lines represent the change of $\rho \underline{u}$ due to the movement of the surface of discontinuity. The S_d^- and S_d^+ represent both sides of the surface and the equation can be reduced to,

$$\iint_{S_d} \llbracket \rho (\underline{u} - \underline{u}_d) \cdot \underline{n}_d \rrbracket \, dS = 0, \quad (2.127)$$

after subtraction of the continuity equation for $V_1 + V_2$ and introduction of the jump brackets. Note that S_d can be an arbitrary part of this surface of discontinuity. Therefore, the integrand itself should be equal to zero on S_d ,

$$\llbracket \rho (\underline{u} - \underline{u}_d) \cdot \underline{n}_d \rrbracket = 0. \quad (2.128)$$

This equation can be simplified under the assumption that the density is constant. Furthermore the velocity can be made dimensionless with the equations introduced in (2.85) and the equation can be depth-averaged. Hence,

$$\llbracket h(\bar{\mathbf{u}} - \bar{\mathbf{u}}_d) \cdot \mathbf{n}_d \rrbracket = 0. \quad (2.129)$$

Similarly, the jump condition for the momentum equations is derived as,

$$\llbracket h\bar{\mathbf{u}}(\bar{\mathbf{u}} - \bar{\mathbf{u}}_d) \cdot \mathbf{n}_d \rrbracket + \llbracket {}^{1/2}\varepsilon h^2 \cos(\zeta) \rrbracket \mathbf{n}_d = 0. \quad (2.130)$$

2.3 Statistics

Coupling of the discontinuous solution method described in §2.1 and the continuous approach described in §2.2 is done with the use of statistical mechanics. This section starts with the basic idea behind this coupling method (§2.3.1). Thereafter, it is shown that the definitions stated in this section satisfy both the continuity equation (§2.3.2) and conservation of momentum (§2.3.3).

2.3.1 Basic idea

Molecular dynamics simulations are based on individual particles and its properties, whereas continuum simulations like Finite Volume simulations consider for example finite volumes which can be combined to get the continuous solution. Averaging the particle properties over time and/or space is a way to translate the discrete results into the continuous domain. This process is also known as coarse-graining or smoothing of the discrete results. The coarse-graining will be applied on density, momentum and velocity results from the DPM simulation. These coarse-grained properties can be combined to satisfy continuity and conservation of momentum. The simplest way to compute those averages is by linking them to the centre of mass of each particle. A continuous mass density function is the first of these three quantities which is described in this section. To do so, a singular microscopic mass density [8] function at the position of the centre of mass of the particle \underline{r} and time t can then be defined as,

$$\rho^{mic}(\underline{r}, t) \equiv \sum_{i=1}^{N_m} m_i \delta_i(\underline{r}). \quad (2.131)$$

which is equal to the sum over all moving particles i of the particle's mass m_i multiplied with a Dirac delta function located in the centre of mass of particle i , $\delta_i(\underline{r}) = \delta(\underline{r} - \underline{r}_i(t))$. The total number of moving particles is indicated by N_m and fixed particles do not contribute to this density function. This microscopic mass density is singular due to the use of a Dirac delta function and a non-singular mass density in terms of a smooth distribution is therefore needed. This smooth distribution is chosen to be a Gaussian distribution in \mathcal{D} dimensions and is given by [30],

$$\mathcal{W}(\underline{r} - \underline{r}_i(t)) = \frac{1}{(\sqrt{2\pi} w)^\mathcal{D}} \exp\left(-\frac{|\underline{r} - \underline{r}_i(t)|^2}{2w^2}\right). \quad (2.132)$$

This distribution has a variance w^2 and it is differentiable on $\mathbb{R}^\mathcal{D}$. A non-singular definition of the mass density can be stated with the use of a convolution integral which is, in the general 1D case, given by,

$$(f \otimes g)(r) \equiv \int_{-\infty}^{\infty} f(r')g(r - r') dr', \quad (2.133)$$

and after replacement of one of the functions with a Dirac delta function located at $r_i(t)$ yields,

$$(\delta_i \otimes g)(r) = \int_{-\infty}^{\infty} \delta_i(r')g(r - r') dr', \quad (2.134)$$

from which the solution can be found using integration by parts, which is in general given by,

$$\int_a^b \frac{\partial f}{\partial x} g dx = (fg) \Big|_a^b - \int_a^b f \frac{\partial g}{\partial x} dx, \quad (2.135)$$

where f is replaced by the primitive of the Dirac delta function and g is maintained as an arbitrary function located at $r - r'$,

$$f = \mathcal{P}(\delta_i(r')) \equiv H_i(r'), \quad g = g(r - r'). \quad (2.136)$$

The $H_i(r')$ is the Heaviside function which is a step function with amplitude 1 and it is located at $r' = r_i(t)$. The derivative of the Heaviside function is the Dirac delta function by definition. Therefore, the convolution integral (2.134) can be rewritten as

$$\begin{aligned} \int_{-\infty}^{\infty} \delta_i(r')g(r - r')dr' &= \lim_{z \rightarrow \infty} \left(g(r - r')H_i(r') \right) \Big|_{-z}^z - \int_{-\infty}^{\infty} \frac{\partial g(r - r')}{\partial r'} H_i(r') dr', \\ &= \lim_{z \rightarrow \infty} g(r - z) - \int_{r_i(t)}^{\infty} \frac{\partial g(r - r')}{\partial r'} dr', \\ &= g(r - r_i(t)). \end{aligned} \quad (2.137)$$

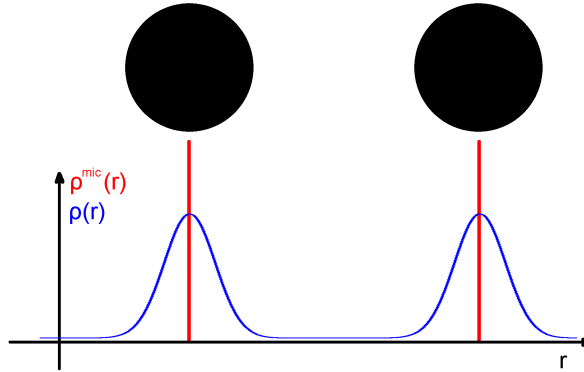


Figure 2.5: Mass density functions in 1D

A similar analogy for the \mathcal{D} dimensional case, indicated by the bars, holds [8] stating that,

$$\int \delta_i(\underline{r}')g(\underline{r} - \underline{r}')d\underline{r}' = g(\underline{r} - \underline{r}_i(t)). \quad (2.138)$$

Knowing this, a smooth mass density can be defined as the combination of the microscopic mass density (2.131) and the Gaussian distribution (2.132) with the use of a convolution integral,

$$\rho(\underline{r}, t) \equiv \int \rho^{mic}(\underline{r}, t) \mathcal{W}(\underline{r} - \underline{r}')d\underline{r}' = \int \sum_{i=1}^{N_m} (m_i \delta_i(\underline{r})) \mathcal{W}(\underline{r} - \underline{r}')d\underline{r}'. \quad (2.139)$$

Note that the order of summation and integration may be interchanged due to fact that the summation is coordinate independent and that the remaining term can be replaced by (2.137). This results in a non-singular definition of the density function. Figure 2.5 shows both the singular microscopic and non-singular mass density functions for two identical and stationary particles in a one dimensional system.

$$\rho(\underline{r}, t) = \sum_{i=1}^{N_m} m_i \int_{-\infty}^{\infty} \delta_i(\underline{r}') \mathcal{W}(\underline{r} - \underline{r}')d\underline{r}' = \sum_{i=1}^{N_m} m_i \mathcal{W}(\underline{r} - \underline{r}_i(t)). \quad (2.140)$$

Three continuous and non-singular quantities are needed to describe the complete discrete results in a continuous manner. The mass density function given by (2.140) is the first of the three. Similar to this function, a coarse grained momentum density, $P_\alpha(\underline{r}, t)$, can be defined as,

$$P_\alpha(\underline{r}, t) \equiv \sum_{i=1}^{N_m} m_i u_{i\alpha} \mathcal{W}(\underline{r} - \underline{r}_i(t)). \quad (2.141)$$

where $u_{i\alpha}$ denotes the particles velocity in each cartesian direction α . The last of the three quantities is the macroscopic velocity $\underline{U}(\underline{r}, t)$. This velocity is a continuous field showing a weighted average of velocities and it is defined as [8, 30],

$$U_\alpha(\underline{r}, t) \equiv \frac{P_\alpha(\underline{r}, t)}{\rho(\underline{r}, t)}. \quad (2.142)$$

The three macroscopic quantities as described in (2.140), (2.141) and (2.142) of a one dimensional system consisting of two identical particles with opposite velocities performing a purely collinear elastic collision are shown in figure 2.6 and 2.7. The figures show the same system at different times: t_0 is the initial situation, t_1 is a time during collision, t_2 is at the maximum overlap in the collision and t_3 is the moment that the particles reach their initial position again. The particles having a radius of 0.2 are initially located at 0.2 and 0.8 and the Gaussian width w is set to 0.1 in figure 2.6 and 0.025 in figure 2.7. Furthermore, the particles have the same mass of 1, stiffness of 60 and velocities ± 0.9 . All numbers listed above are purely illustrative and non-dimensional. The macroscopic velocity can be considered as a weighted average of the particle velocities causing a jump with a finite gradient in this quantity. This jump will be steeper for distributions which are less wide [14], which can be seen when comparing figure 2.6 to figure 2.7. A steeper jump is also present when the particles are further away, this is clearly visible from the sub figures within either of the two figures.

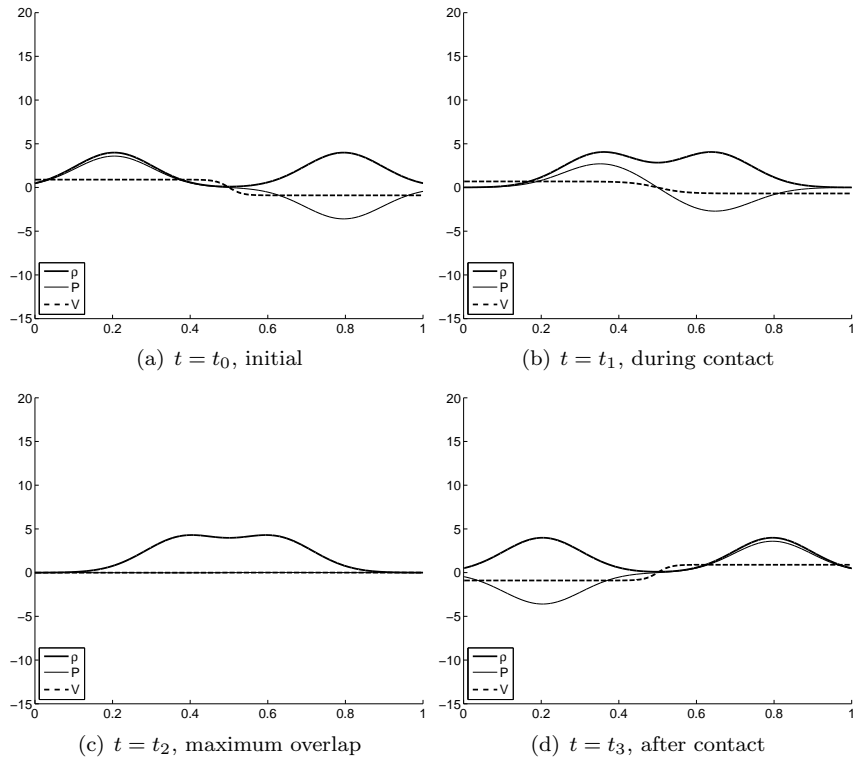


Figure 2.6: Macroscopic mass, momentum and velocity functions for a 1D system with two identical particles having opposite velocities for four different times and a Gaussian width of $w = 0.1$.

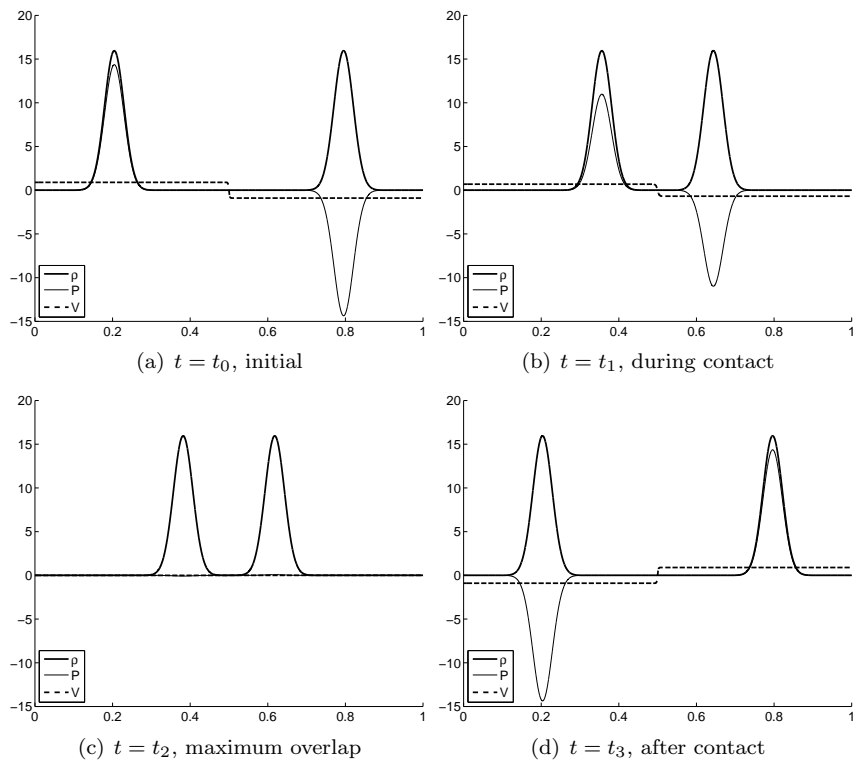


Figure 2.7: Macroscopic mass, momentum and velocity functions for a 1D system with two identical particles having opposite velocities for four different times and a Gaussian width of $w = 0.025$.

2.3.2 Continuity

Continuity (2.51) should be satisfied by the smooth functions shown in (2.140) and (2.141). This can be shown by differentiating (2.140) to time and (2.141) to r_α . This differentiation makes use of,

$$\frac{\partial \mathcal{W}(\underline{r} - \underline{r}_i(t))}{\partial r_\alpha} = \frac{\partial \mathcal{W}(\underline{h})}{\partial r_\alpha} = \frac{\partial \mathcal{W}(\underline{h})}{\partial h_\beta} \frac{\partial h_\beta}{\partial r_\alpha} = \frac{\partial \mathcal{W}(\underline{h})}{\partial h_\alpha}, \quad (2.143)$$

where Einstein's summation convention is applied to Greek subscripts (α, β) which denote the spatial components of the complete argument $\underline{h} = \underline{r} - \underline{r}_i(t)$. Furthermore,

$$\frac{\partial \mathcal{W}(\underline{r} - \underline{r}_i(t))}{\partial t} = \frac{\partial(r_\alpha - r_{i\alpha}(t))}{\partial t} \frac{\partial \mathcal{W}(\underline{r} - \underline{r}_i(t))}{\partial h_\alpha} = -u_{i\alpha} \frac{\partial \mathcal{W}(\underline{r} - \underline{r}_i(t))}{\partial r_\alpha}, \quad (2.144)$$

is allowed where $\underline{h} = \underline{r} - \underline{r}_i(t)$ and (2.143) is used in the last step. Differentiating (2.140) with respect to time yields,

$$\frac{\partial \rho(\underline{r}, t)}{\partial t} = \frac{\partial}{\partial t} \sum_{i=1}^{N_m} m_i \mathcal{W}(\underline{r} - \underline{r}_i(t)) = \sum_{i=1}^{N_m} m_i \frac{\partial}{\partial t} \mathcal{W}(\underline{r} - \underline{r}_i(t)), \quad (2.145)$$

where interchanging the differential and summation operators is allowed by the sum rule of differentiation. The derivative of (2.141) with respect to space yields,

$$\frac{\partial P_\alpha(\underline{r}, t)}{\partial r_\alpha} = \frac{\partial}{\partial r_\alpha} \sum_{i=1}^{N_m} m_i u_{i\alpha} \mathcal{W}(\underline{r} - \underline{r}_i(t)) = \sum_{i=1}^{N_m} m_i u_{i\alpha} \frac{\partial}{\partial r_\alpha} \mathcal{W}(\underline{r} - \underline{r}_i(t)). \quad (2.146)$$

With these two derivatives at hand and using (2.144), the continuity equation (2.51) can be stated as,

$$\frac{\partial \rho(\underline{r}, t)}{\partial t} = -\frac{\partial P_\alpha(\underline{r}, t)}{\partial r_\alpha}, \quad (2.147)$$

conservation of mass therefore holds for the statistical averaged DPM results.

2.3.3 Conservation of momentum

The macroscopic functions for density (2.140), momentum (2.141) and velocity (2.142) should conserve momentum (2.61) to match the continuous solution. This can be shown by differentiating the momentum density function (2.141) with respect to time,

$$\begin{aligned} \frac{\partial P_\alpha(\underline{r}, t)}{\partial t} &= \frac{\partial}{\partial t} \sum_{i=1}^{N_m} m_i u_{i\alpha} \mathcal{W}(\underline{r} - \underline{r}_i(t)), \\ &= \underbrace{\sum_{i=1}^{N_m} m_i a_{i\alpha} \mathcal{W}(\underline{r} - \underline{r}_i(t))}_{A_\alpha} + \underbrace{\sum_{i=1}^{N_m} m_i u_{i\alpha} \frac{\partial}{\partial t} \mathcal{W}(\underline{r} - \underline{r}_i(t))}_{B_\alpha}, \end{aligned} \quad (2.148)$$

where $a_{i\alpha}$ is the acceleration of particle i in α direction. Due to the complexity of both terms, A_α and B_α , these will be discussed individually. Applying Newton's second law to A_α yields,

$$A_\alpha = \sum_{i=1}^{N_m} m_i a_{i\alpha} \mathcal{W}(\underline{r} - \underline{r}_i(t)) = \sum_{i=1}^{N_m} f_{i\alpha} \mathcal{W}(\underline{r} - \underline{r}_i(t)), \quad (2.149)$$

where $f_{i\alpha}$ is the force acting on particle i in α direction. This force can be written as the the summation of all forces acting on particle i and can be split in three types of forces. The first type is due to pairs of moving particles $f_{ij\alpha}$ where j denotes the second moving particle in the pair. The second sum of forces is based on particle pairs built with one fixed and one moving particle $f_{ik\alpha}^w$ where k denotes the fixed particle and the last force is the gravitational body force,

$$f_{i\alpha} = \sum_{j=1}^{N_m} f_{ij\alpha} + \sum_{k=1}^{N_f + N_w} f_{ik\alpha}^w + m_i g_\alpha. \quad (2.150)$$

Note that there is no force when the particle is compared with itself; $f_{ii\alpha} \equiv 0$ and that N_f is the total number of fixed particles. The interactions between moving particles and smooth walls is also included in the middle term with N_w denoting the total number of walls. Implementing (2.150) into (2.149) yields,

$$A_\alpha = \sum_{i=1}^{N_m} \sum_{j=1}^{N_m} f_{ij\alpha} \mathcal{W}_i + \sum_{i=1}^{N_m} \sum_{k=1}^{N_f+N_w} f_{ik\alpha}^w \mathcal{W}_i + \sum_{i=1}^{N_m} m_i g_\alpha \mathcal{W}_i, \quad (2.151)$$

where the sum is split over the different contributions on the total force on particle i and where the notation $\mathcal{W}_i = \mathcal{W}(\underline{r} - \underline{r}_i(t))$ is used. Furthermore, the last term can be simplified to ρg_α with the use of (2.140). Swapping indices in the first term in (2.151) and applying Newton's third law ($f_{ij\alpha} = -f_{ji\alpha}$) yields,

$$\begin{aligned} A_\alpha &= \sum_{j=1}^{N_m} \sum_{i=1}^{N_m} f_{ji\alpha} \mathcal{W}_j + \sum_{i=1}^{N_m} \sum_{k=1}^{N_f+N_w} f_{ik\alpha}^w \mathcal{W}_i + \rho g_\alpha, \\ &= - \sum_{i=1}^{N_m} \sum_{j=1}^{N_m} f_{ij\alpha} \mathcal{W}_i + \sum_{i=1}^{N_m} \sum_{k=1}^{N_f+N_w} f_{ik\alpha}^w \mathcal{W}_i + \rho g_\alpha. \end{aligned} \quad (2.152)$$

Adding (2.151) and (2.152) while dividing by 2 results in,

$$A_\alpha = \frac{1}{2} \sum_{i=1}^{N_m} \sum_{j=1}^{N_m} f_{ij\alpha} (\mathcal{W}_i - \mathcal{W}_j) + \sum_{i=1}^{N_m} \sum_{k=1}^{N_f+N_w} f_{ik\alpha}^w \mathcal{W}_i + \rho g_\alpha. \quad (2.153)$$

From (2.61) one needs to identify a stress tensor in order to achieve a consistent notation of the conservation of momentum. Therefore, a divergence operator (the ' $\underline{\nabla} \cdot$ ' in (2.61)) is needed within A_α . This operator can be implemented in A_α by introducing a linear integration method for the two coarse graining functions \mathcal{W}_j and \mathcal{W}_i in A_α ,

$$\mathcal{W}_i - \mathcal{W}_j = - \int_0^1 \frac{\partial}{\partial s} \mathcal{W}(\underline{r} - \underline{r}_i + s \underline{r}_{ij}) ds, \quad (2.154)$$

with $\underline{r}_{ij} = \underline{r}_i - \underline{r}_j$ and time dependencies omitted. The divergence is found when the chain rule, similar to (2.143), is applied to (2.154),

$$\mathcal{W}_i - \mathcal{W}_j = -r_{ij\beta} \frac{\partial}{\partial r_\beta} \int_0^1 \mathcal{W}(\underline{r} - \underline{r}_i + s \underline{r}_{ij}) ds. \quad (2.155)$$

Note that the divergence is independent of s and can thus be moved in front of the integral. Substitution of (2.155) into (2.153) yields,

$$A_\alpha = -\frac{1}{2} \sum_{i=1}^N \sum_{j=1}^N f_{ij\alpha} r_{ij\beta} \frac{\partial}{\partial r_\beta} \int_0^1 \mathcal{W}(\underline{r} - \underline{r}_i + s \underline{r}_{ij}) ds + \sum_{i=1}^{N_m} \sum_{k=1}^{N_f+N_w} f_{ik\alpha}^w \mathcal{W}_i + \rho g_\alpha, \quad (2.156)$$

where first term represents the contact stresses for pairs of moving particles due to the presence of the divergence. The middle term can be identified as being the interaction force density IFD [31] which is constructed in such a way that it satisfies Newton's third law. This IFD is positioned at the centre of mass of the moving particles due to \mathcal{W}_i which is not the physical location of the boundary. Therefore, the IFD is moved to the contact points $c_{ik\alpha}$, with the use of $\underline{r}_{ik}^c = \underline{r} - \underline{c}_{ik}$. Hence,

$$\mathcal{W}_{ik} - \mathcal{W}_i = r_{ik\beta}^c \frac{\partial}{\partial r_\beta} \int_0^1 \mathcal{W}(\underline{r} - \underline{r}_i + s \underline{r}_{ik}^c) ds, \quad (2.157)$$

with $\mathcal{W}_{ik} = \mathcal{W}(\underline{r} - \underline{c}_{ik})$. This movement operator introduces a divergence operator on the interactions between fixed and moving particles resulting in a contribution to the stress tensor. Rewriting this movement and substitution in the middle term of (2.153) yields,

$$\begin{aligned} \sum_{i=1}^{N_m} \sum_{k=1}^{N_f+N_w} f_{ik\alpha}^w \mathcal{W}_i &= \sum_{i=1}^{N_m} \sum_{k=1}^{N_f+N_w} f_{ik\alpha}^w \left(\mathcal{W}_{ik} - r_{ik\beta}^c \frac{\partial}{\partial r_\beta} \int_0^1 \mathcal{W}(\underline{r} - \underline{r}_i + s \underline{r}_{ik}^c) ds \right), \\ &= \sum_{i=1}^{N_m} \sum_{k=1}^{N_f+N_w} f_{ik\alpha}^w \mathcal{W}_{ik} - \sum_{i=1}^{N_m} \sum_{k=1}^{N_f+N_w} f_{ik\alpha}^w r_{ik\beta}^c \frac{\partial}{\partial r_\beta} \int_0^1 \mathcal{W}(\underline{r} - \underline{r}_i + s \underline{r}_{ik}^c) ds. \end{aligned} \quad (2.158)$$

from which the IFD is identified as being,

$$t_\alpha = \sum_{i=1}^{N_m} \sum_{k=1}^{N_f+N_w} f_{ik\alpha}^w \mathcal{W}_{ik}. \quad (2.159)$$

A_α can then be stated as,

$$A_\alpha = -\frac{1}{2} \sum_{i=1}^{N_m} \sum_{j=1}^{N_m} f_{ij\alpha} r_{ij\beta} \frac{\partial}{\partial r_\beta} \int_0^1 \mathcal{W}(\underline{r} - \underline{r}_i + s \underline{r}_{ij}) ds + \rho g_\alpha \\ - \sum_{i=1}^{N_m} \sum_{k=1}^{N_f+N_w} f_{ik\alpha}^w r_{ik\beta}^c \frac{\partial}{\partial r_\beta} \int_0^1 \mathcal{W}(\underline{r} - \underline{r}_i + s \underline{r}_{ik}^c) ds + t_\alpha. \quad (2.160)$$

In order to identify the second term in the conservation of momentum (2.61), the expression for B_α needs to be rewritten. Equation (2.144) is therefore substituted into B_α and (2.146) allows the interchanging of the summation and differentiation operators. Hence,

$$B_\alpha = \sum_{i=1}^{N_m} m_i u_{i\alpha} \frac{\partial}{\partial t} \mathcal{W}_i = - \sum_{i=1}^{N_m} m_i u_{i\alpha} u_{i\beta} \frac{\partial \mathcal{W}_i}{\partial r_\beta} = - \frac{\partial}{\partial r_\beta} \sum_{i=1}^{N_m} m_i u_{i\alpha} u_{i\beta} \mathcal{W}_i, \quad (2.161)$$

where the product of the momentum and velocity is present but it is stated in terms of the particle velocities. The second term in (2.61) is based on the macroscopic velocity $\underline{U}(\underline{r}, t)$. Therefore, a fluctuation velocity [8] is introduced and it relates the velocity of a particle i with the macroscopic velocity (2.142),

$$\underline{u}'_i \equiv \underline{u}_i - \underline{U}(\underline{r}, t). \quad (2.162)$$

Coarse graining this quantity should make it vanish since it only exist in the discrete notation. This can be proofed by applying the coarse graining function on this velocity fluctuation. Note that the macroscopic velocity is independent of the particle and can thus be moved in front of the sum,

$$\sum_{i=1}^{N_m} m_i \underline{u}'_i \mathcal{W}_i = \sum_{i=1}^{N_m} m_i (\underline{u}_i - \underline{U}) \mathcal{W}_i, \\ = \sum_{i=1}^{N_m} m_i \underline{u}_i \mathcal{W}_i - \underline{U} \sum_{i=1}^{N_m} m_i \mathcal{W}_i, \\ = \underline{P} - \rho \underline{U} = 0. \quad (2.163)$$

Applying the velocity fluctuation to (2.161) yields,

$$B_\alpha = - \frac{\partial}{\partial r_\beta} \left[\sum_{i=1}^{N_m} m_i (u'_{i\alpha} + U_\alpha)(u'_{i\beta} + U_\beta) \mathcal{W}_i \right], \quad (2.164)$$

where the brackets can be worked out with the fact that the macroscopic velocity is particle independent and can thus be moved in front of the sum,

$$B_\alpha = - \frac{\partial}{\partial r_\beta} \left[U_\alpha U_\beta \sum_{i=1}^{N_m} m_i \mathcal{W}_i + 2U_\alpha \sum_{i=1}^{N_m} m_i u'_{i\beta} \mathcal{W}_i + \sum_{i=1}^N m_i u'_{i\alpha} u'_{i\beta} \mathcal{W}_i \right]. \quad (2.165)$$

The middle term is equal to zero, see (2.163), and (2.140) used to simplify the first term in order to get the final expression for B_α . This expression covers the second term in the conservation of momentum (2.61) and introduces another stress term,

$$B_\alpha = - \frac{\partial (\rho U_\alpha U_\beta)}{\partial r_\beta} - \frac{\partial}{\partial r_\beta} \sum_{i=1}^N m_i u'_{i\alpha} u'_{i\beta} \mathcal{W}_i. \quad (2.166)$$

With the rewritten versions of A_α and B_α at hand, equation (2.148) can be written as,

$$\frac{\partial P_\alpha}{\partial t} + \frac{\partial (\rho U_\alpha U_\beta)}{\partial r_\beta} = - \frac{1}{2} \sum_{i=1}^N \sum_{j=1}^N f_{ij\alpha} r_{ij\beta} \frac{\partial}{\partial r_\beta} \int_0^1 \mathcal{W}(\underline{r} - \underline{r}_i + s \underline{r}_{ij}) ds + \rho g_\alpha \\ - \sum_{i=1}^{N_m} \sum_{k=1}^{N_f+N_w} f_{ik\alpha}^w r_{ik\beta}^c \frac{\partial}{\partial r_\beta} \int_0^1 \mathcal{W}(\underline{r} - \underline{r}_i + s \underline{r}_{ik}^c) ds + t_\alpha - \frac{\partial}{\partial r_\beta} \sum_{i=1}^N m_i u'_{i\alpha} u'_{i\beta} \mathcal{W}_i. \quad (2.167)$$

Combining all right hand side terms with a divergence operator allows the identification of the stress tensor $\sigma_{\alpha\beta}$ [8, 14, 30, 31].

$$\begin{aligned} \sigma_{\alpha\beta} = & -\frac{1}{2} \sum_{i=1}^N \sum_{j=1}^N f_{ij\alpha} r_{ij\beta} \int_0^1 \mathcal{W}(r - r_i + sr_{ij}) ds \\ & - \sum_{i=1}^{N_m} \sum_{k=1}^{N_f+N_w} f_{ik\alpha}^w r_{ik\beta}^c \int_0^1 \mathcal{W}(r - r_i + sr_{ik}^c) ds - \sum_{i=1}^N m_i u'_{i\alpha} u'_{i\beta} \mathcal{W}_i. \end{aligned} \quad (2.168)$$

Note that conservation of momentum is still satisfied when an arbitrary function with a divergence of zero is added to this stress term. Therefore, it is not a unique definition of stress, see Wajnryb *et al.* [27] and the references therein. Due to the fact that the stress tensor is only used to check the conservation of mass, and thus only is used with a divergence operator applied to it, it can still be used. The former term in (2.168) represents the contact stress between two moving particles, the middle term the contact stress due to particle-boundary interactions and the latter the streaming stress [4] which is also known as kinetic stress. This streaming stress is associated with the transportation of momentum. Two extreme cases in a system without boundaries and/or fixed particles can be identified; the stresses in a very dense system of particles are dominated by the contact stresses since the velocity fluctuations are expected to be very small. On the other hand, the contribution of contact stresses in very dilute systems will be very small due the small number of contacts in these systems. The streaming stress will then be dominant due to the high velocity fluctuations. Identifying the stresses as (2.168) allows the rewriting of (2.167) into,

$$\frac{\partial P_\alpha}{\partial t} + \frac{\partial(\rho U_\alpha U_\beta)}{\partial r_\beta} = \frac{\partial \sigma_{\alpha\beta}}{\partial r_\beta} + \rho g_\alpha + t_\alpha \quad (2.169)$$

which represents conservation of momentum as shown in (2.61) and implies that the momentum, while travelling with the flow, may change due to body forces and stresses. Note that this expression differs from (2.61) due to the presence of the interaction force density term. The momentum in the same 1D example as shown previously will only change due to the contact stresses between the two moving particles and the streaming stress since there are no boundaries nor gravitational body forces present. Where the streaming stresses can be solved in a straight forward manner, the contact stresses need more attention. The contact stresses are analytically solved with the use of the one-dimensional coarse graining function which is equivalent to the one given in (2.132),

$$\mathcal{W}_i = \frac{1}{w\sqrt{2\pi}} \exp\left(-\frac{(r - r_i)^2}{2w^2}\right), \quad (2.170)$$

and the definition of an error function,

$$\text{erf}(z) \equiv \frac{2}{\sqrt{\pi}} \int_0^z \exp(-x^2) dx, \quad (2.171)$$

which allows the writing of

$$\text{erf}(b) - \text{erf}(a) = \frac{2}{\sqrt{\pi}} \int_a^b \exp(-x^2) dx, \quad (2.172)$$

and can be applied to the integral within the contact stress if it is stated that,

$$\begin{aligned} x &= \frac{r - r_i + sr_{ij}}{w\sqrt{2}}, & ds &= \frac{w\sqrt{2}}{r_i - r_j} dx, \\ a = x(s=0) &= \frac{r - r_i}{w\sqrt{2}}, & b = x(s=1) &= \frac{r - r_j}{w\sqrt{2}}. \end{aligned} \quad (2.173)$$

Hence,

$$\begin{aligned} \int_0^1 \mathcal{W}(r - r_i + sr_{ij}) ds &= \frac{1}{w\sqrt{2\pi}} \int_0^1 \exp\left(-\frac{(r - r_i + sr_{ij})^2}{2w^2}\right) ds, \\ &= \frac{1}{w\sqrt{2\pi}} \int_a^b \exp\left(-\frac{(r - r_i + sr_{ij})^2}{2w^2}\right) \frac{w\sqrt{2}}{r_i - r_j} dx, \\ &= \frac{1}{2(r_i - r_j)} \left(\text{erf}\left(\frac{r - r_j}{w\sqrt{2}}\right) - \text{erf}\left(\frac{r - r_i}{w\sqrt{2}}\right) \right). \end{aligned}$$

The stresses for the systems corresponding to figures 2.6 and 2.7 are shown in figure 2.8 ($w = 0.1$) and 2.9 ($w = 0.025$) respectively. Sub figures (a) show the initial setup where the two particles are far from each other, resulting in zero contact stress (there is no contact) and very small streaming stresses. The coarse graining functions for the system with wide distributions cause a fluctuation velocity with respect to the weighted average of particle velocities resulting in a streaming stress, even if the particles are not in contact. All the other subsequent sub figures of figure 2.9 show a streaming stress of approximately zero with an absolute maximum of $2.33 \cdot 10^{-5}$. These small values are due to the steepness of the coarse graining functions involved. The wider distributions cause a higher absolute maximum streaming stress of 1.46. A slightly further evolved time step, which corresponds to figure 2.6(b), is shown in 2.8(b) where the particles are in contact but still moving. Therefore, both contact and streaming stresses are present. The third sub figure, (c), corresponds to figure 2.6(c) and shows the system at maximum overlap. The particles do not have any velocity and therefore the contribution of the streaming stress is exactly zero. Furthermore, the overlap is maximum, resulting in an absolute maximum contact stress of -8.92 for the wide distribution and -9.86 for the narrow distribution. The last sub figure shows the system after collision where the particles are back in their initial positions. When the contact stresses between the individual sub figures within figures 2.8 and 2.9 are compared, one can see that the latter result in a steeper increase of this stresses. The stresses are distributed over the contact path between the two particles [14]. This means that wide Gaussian distributions cause a smooth transition in the contact stress. Narrow distributions result in a stress plateau due to the steepness of the individual error functions contributing to the contact stresses.

2.4 Dimensional analysis

Scientific problems like the problem at hand, see §3.1 for an overview, are usually described by a set of dimensionless numbers. These numbers have the advantage that they are scalable and can be used to determine the characteristics of the system. Interesting dimensionless numbers are sought with Buckingham's π theorem in §2.4.1 whereafter the relevant dimensionless numbers are described in more detail §2.4.2 - §2.4.4.

2.4.1 Buckingham's π theorem

Buckingham's π theorem states that D dimensionless groups can be formed based on the number of fundamental units U and V variables [32] for any problem,

$$D = V - U. \quad (2.174)$$

These groups can be found by defining all the independent variables and their corresponding units. Table 2.4.1 shows the 20 variables with 3 unique units, detailed explanations and typical values for the variables listed are shown in chapter 3. Buckingham's π theorem indicates that 17 independent dimensionless groups can be found. Therefore, typical scaling factors should be chosen for all of the unique units. The particle's diameter d is chosen for the length scale, $\sqrt{h/g}$ for the time scale and ρd^3 for the weight scale. The progress of making the dimensionless groups starts with a first guess in

S.	Description	Units	S.	Description	Units
d	Particle's diameter	[m]	h	Flow height	[m]
ρ	Density	[kg m ⁻³]	u	Velocity	[m s ⁻¹]
t_c	Collision time	[s]	$\dot{\theta}$	Rotational velocity	[s ⁻¹]
e^n	Coefficient of restitution	[-]	λ	Mean free path	[m]
μ_c	Friction coefficient	[-]	L	Length of the plate	[m]
k^t	Tangential stiffness	[kg s ⁻²]	W	Width of the plate	[m]
γ^t	Tangential dissipation coefficient	[m s ⁻¹]	H	Typical flow height	[m]
g	Gravitational constant	[m s ⁻²]	ζ	Inclination angle	[-]
D	Funnel diameter	[m]	α	Funnel angle	[-]
H_f	Falling height	[m]	n_z	# particles along funnel side	[-]

Table 2.1: Independent variables in the system with their corresponding symbols, descriptions and units

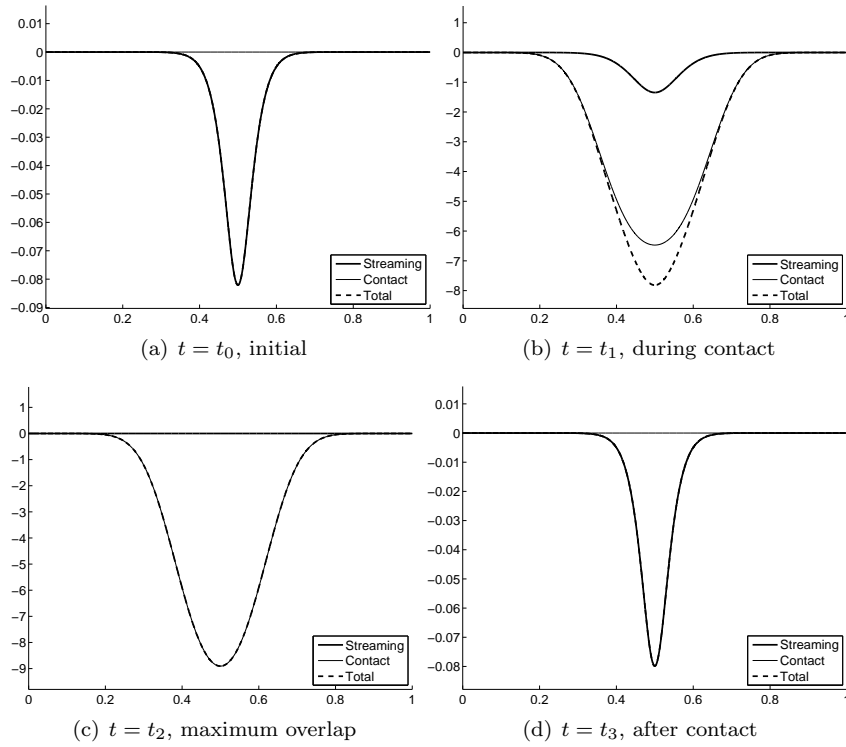


Figure 2.8: Streaming, contact and total stresses for a 1D system with two identical particles having opposite velocities for four different times and a Gaussian width of $w = 0.1$

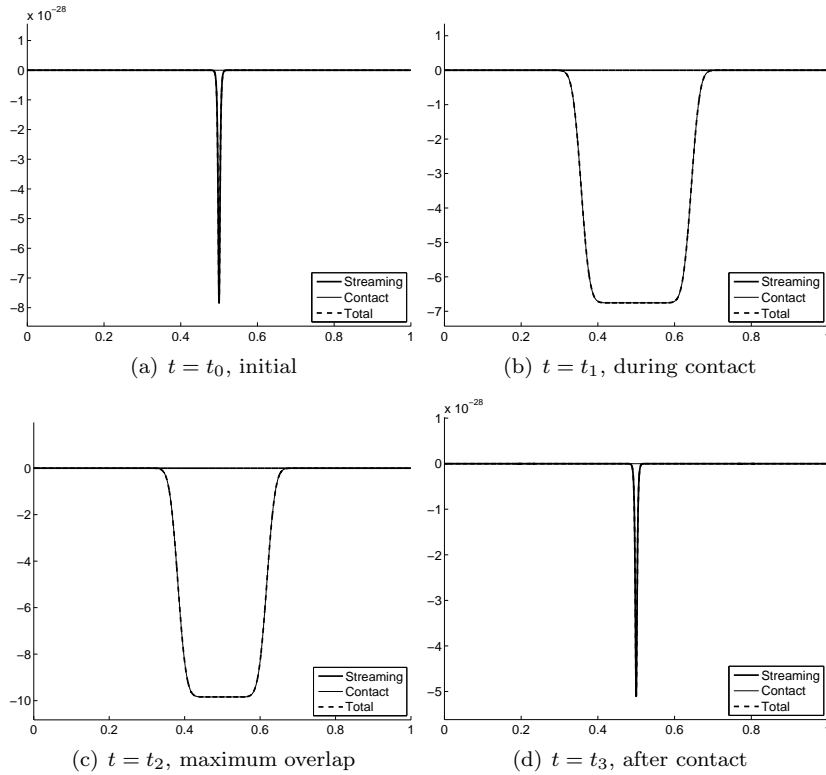


Figure 2.9: Streaming, contact and total stresses for a 1D system with two identical particles having opposite velocities for four different times and a Gaussian width of $w = 0.025$.

which all units are cancelled with the three quantities described above. This results in the following list of dimensionless groups,

$$\frac{t_c}{\sqrt{h/g}}, \epsilon_n, \mu_c, \frac{k^t h}{g \rho d^3}, \frac{\gamma^t \sqrt{h/g}}{\rho d^3}, \frac{D}{d}, \frac{H_f}{d}, \frac{h}{d}, \frac{u \sqrt{h/g}}{d}, \frac{\lambda}{d}, \dot{\theta} \sqrt{h/g}, \frac{L}{d}, \frac{W}{d}, \frac{H}{d}, \zeta, \alpha, n_z. \quad (2.175)$$

These groups are independent dimensionless groups which may be combined to form known dimensionless numbers like the Froude's number. Three of those groups are relevant for the problem at hand are discussed in the upcoming sections.

2.4.2 Dimensionless height

Several simplifications in the derivation of the granular shallow flow equations are based on the assumption that the ratio of the typical height of the flow and the length of the plate is small. This ratio is given by,

$$\varepsilon = \frac{H}{d} / \frac{L}{L} = \frac{H}{L}. \quad (2.176)$$

It is calculated for the system in §5.6 to validate the assumption.

2.4.3 Froude number

The Froude number describes the ratio of the flow velocity and the gravitational wave velocity. When this number is smaller than 1, $Fr < 1$, the flow is called 'sub-critical' meaning that information in the flow may propagate in the up-stream direction. Froude numbers bigger than 1, $Fr > 1$, are called 'super-critical' and information cannot propagate in up-stream direction. The speed of the flow $\|U\|$ and the gravitational wave velocity \sqrt{gh} are used in the calculation of the Froude number. The number can be constructed with use of the dimensionless groups listed in (2.175),

$$Fr = \frac{u \sqrt{h/g}}{d} / \frac{h}{d} = \frac{u}{\sqrt{gh}}, \quad (2.177)$$

which is the Froude number for any flow. Extension in terms of a granular flow over an inclined plane is done by taking the ratio of the dimensionless velocity and the dimensionless reduced gravitational wave velocity $\varepsilon h \cos(\zeta)$ [17].

$$Fr = \frac{u}{\sqrt{\varepsilon h \cos(\zeta)}}. \quad (2.178)$$

The Froude number is used in the characterisation of the kinetic region and the rest of the flow, see §5.5 where the number is calculated for the system.

2.4.4 Knudsen number

The derivation of the granular shallow flow equations starts with the assumption that the flow is a continuum. This assumption can be validated with the Knudsen number which describes the ratio of the mean free path λ and the characteristic length scale in the system. Since this number represents the chance of a collision in the flow, the characteristic length is chosen to be typical flow height H . The mean free path, which is needed for the Knudsen number, is calculated from the Enskog collision rate [20],

$$\lambda = t_E / u, \quad (2.179)$$

where t_E is the Enskog collision rate and u is the down-slope fluctuation velocity of the particles. The mean free path can then be written as,

$$\lambda = \frac{\sqrt{\pi} d}{2^{\mathcal{D}} \mathcal{D} \nu g_{\mathcal{D}}(\nu)}, \quad (2.180)$$

in which \mathcal{D} is the number of dimensions in the system, ν the volume fraction of particles and $g_{\mathcal{D}}(\nu)$ the height of the first peak in a normalized radial distribution function which is given by [20],

$$g_3(\nu) = \frac{1 - \frac{\nu}{2}}{(1 - \nu)^3}, \quad (2.181)$$

for a three dimensional system and ν is calculated by,

$$\nu = \sum_i^{N_m} v_i \mathcal{W}_i. \quad (2.182)$$

The Knudsen number can be constructed from the list of dimensionless groups (2.175),

$$Kn = \frac{\lambda}{d} \frac{d}{H} = \frac{\lambda}{H}, \quad (2.183)$$

and typical values for this number are shown in §5.4.

Chapter 3

Simulation setup

This chapter describes how the physical problem is translated in a simulation. Therefore, an overview of the problem is described in §3.1. The outcome of the DPM simulation depends on the particle properties and boundary conditions which are described in §3.2, followed by a description of the funnel (§3.3) and the bottom plate (§3.4). The method used to remove particles from the system (§3.5) concludes the section.

3.1 Overview

The problem at hand considers a granular jet, originating from a funnel, which impinges on an inclined plane. All aspects of the setup are discussed while following the flow, see from figure 3.1. Note that the cartesian coordinate system is chosen with the x coordinate over the length of the plate. The domain is then bounded by $x_0 \leq x \leq x_1$, $y_0 \leq y \leq y_1$ and $z_0 \leq z \leq z_1$ where the typical values of the limits are shown in table 3.1 and based on experience from preliminary simulations. The table also gives the limits for other system parameters like the falling height H_f , the funnel diameter D and the inclination angle ζ which originate from Johnson and Gray [17].

3.2 Particle properties

The particles have many properties in order to approach the used sand in the experiments closely. Some of these properties follow straight-forward from the work performed by Johnson and Gray [17] of which the particle diameter is a good example. Other properties are based on experience or work performed by others. Table 3.2 shows a detailed list of the particle properties.

3.3 Funnel properties

The granular jet produced in the experiments provided a steady outflow. Achieving a similar jet is done by adding a funnel to the system. The top part of this funnel is randomly filled with particles and, due to the collisions in this funnel, a dense and stable jet is formed. Such a funnel is created with the use of fixed particles which are placed in circles at a certain height and at the inclination angle of the plate. The orientation of the resulting outflow is then parallel with the orientation of the gravitational

S.	Low limit	High limit	Motivation
x	-0.021 m	0.250 m	Empirical
y	0.000 m	0.150 m	Empirical
z	0.000 m	0.069 m	Empirical
H_f	0.050 m	0.075 m	Johnson and Gray [17]
D	0.015 m	0.015 m	Johnson and Gray [17]
ζ	23.0°	29.0°	Johnson and Gray [17]

Table 3.1: System parameters and corresponding values

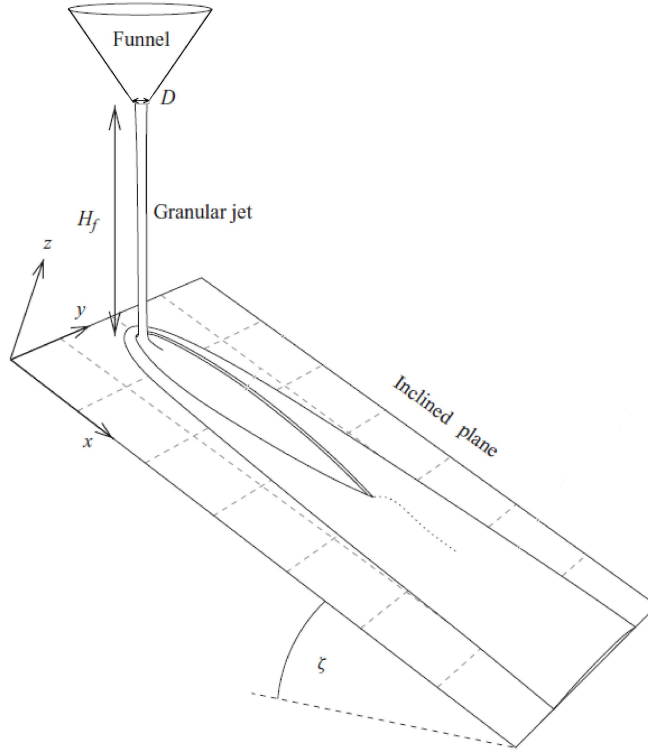


Figure 3.1: Overview of the problem [17]

body force. The funnel outlet diameter D and the falling height H_f originate from the work presented by Johnson and Gray [17] and are listed in table 3.1. Figure 3.2(a) shows a cross section of the funnel and the other parameters which define the funnel. These parameters are the funnel origin O , i.e. the location of the funnel in x and y directions of the plate, the growth angle a and the number of particles along the side of the funnel n_z . The origin is always located in the middle of the y domain and in the beginning of the x domain. The growth angle is set to 60° and n_z is set to 25 resulting in enough collisions to provide the required dense and stable flow.

3.4 Bottom plate

There are multiple options for the creation of the bottom plate. It is possible to use a planar wall as described in §2.1.1 or fixed particles. The second option is needed when a rough plate is required. In the case of a granular jet impinging on a plate such a roughness is required and fixed particles are thus created at $z = 0$ m. These particles can be ordered in a grid or placed randomly, where the gridlike

S.	Description	Value	Units	Motivation
d	Particle's diameter	0.006	[m]	Johnson and Gray [17]
μ_c	Friction coefficient	0.5	[-]	See §2.2.8
ρ	Density	1442	[kg m ⁻³]	Boudet <i>et.al</i> [2]
t_c	Collision time	4×10^{-4}	[s]	A.R. Thornton
e^n	Coefficient of restitution	0.6	[-]	T. Weinhart
k^t/k^n	Ratio of tangential and normal stiffness	2/7	[-]	Weinhart <i>et.al</i> [30]
γ^t/γ^n	Ratio of tangential and normal dissipation	2/7	[-]	T. Weinhart

Table 3.2: Particle properties showing the symbol, description, value, units and motivation

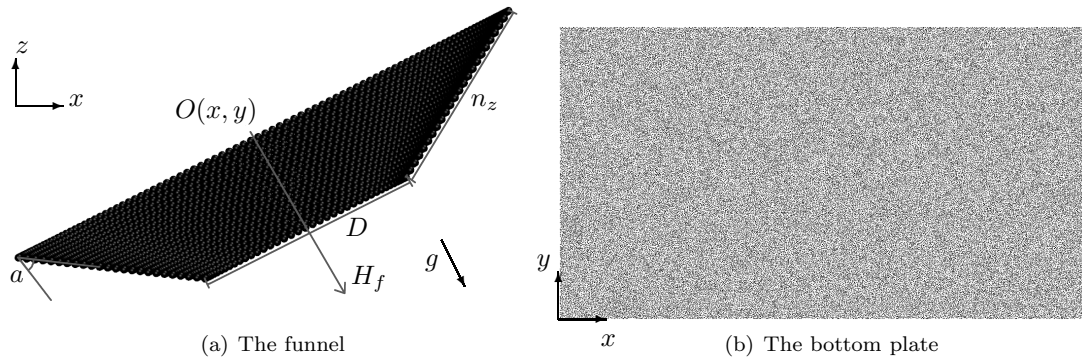


Figure 3.2: Cross section of the funnel and top view of the bottom plate.

placed particles stimulate the flow directions over the grid. Random placed particles are chosen for this reason, preventing preferred flow directions. A top view of the resulting bottom plate is shown in figure 3.2(b) where the particles in this plate have the same size as the flowing particles. Furthermore, a planar wall is placed below the fixed particles to prevent particles falling through.

3.5 Particle removal

Computational time can be significantly reduced when particles which have left the plate are removed. Therefore, particles flowing out of the x and y domain are deleted. It is thus assumed that no particles leave the system through the edges of the z domain.

Chapter 4

Visualisation

The DPM simulation results in a set of data containing all the positions and velocities for all particles at all saved time-steps. Visualisation of this data is performed with the OpenGL engine Visual Molecular Dynamics (VMD) as developed by Humphrey *et. al.* [16]. This tool is specialised in the visualisation of molecules, proteins and other related objects. An implementation to show DPM results with this software is developed within this thesis and the functionality of the code is therefore briefly discussed in this chapter. This implementation allows for a detailed and fully three-dimensional inspection of the DPM results and it is written as a script in the Tool Command Language (TCL): `DPM.tcl`. Launching the programme with the right input variables is performed with a second script, `dovmd` which is a bash script. Note that both scripts come with Mercury and are located in the scripts directory (`sc/`). This chapter starts with a general overview of the output produced by the DPM solver, Mercury [26] (§4.1) which is followed by the explanation of the launch script (§4.2) and the pseudocode for `DPM.tcl` (§4.3).

4.1 Output

The output generated by Mercury [26] contains multiple files, this section briefly describes the purposes and formats of the files. The main output is split into a `.data` file (§4.1.1) containing the particle positions and velocities and a `.fstat` file (§4.1.2) containing the force information. Other output files are the `.restart` file (§4.1.3) and the `.ene` file (§4.1.4). Note that all files are output by Mercury on default, but not all are needed in the visualisation.

4.1.1 Data file

The `.data` file contains all the information regarding the particle positions and velocities. It is a file in the format of 1 header and N lines per written time-step where N is the total number of particles in the system. The headers describe the current number of particles, the current simulation time and the domain. A header for a system with N particles at time t and the typical domain $x_0 \leq x \leq x_1$, $y_0 \leq y \leq y_1$ and $z_0 \leq z \leq z_1$ looks like: `N t x0 y0 z0 x1 y1 z1`. Lines regarding particle information consist of particle specific information, leading to `x y z u v w d/2 tx ty tz wx wy wz` containing positions, velocities, radius and angular positions and velocities. This file is loaded into the visualisation software to position all the particles on all written time-steps in the system.

4.1.2 Fstat file

The `.fstat` file contains all collisional information in the format of a header followed by a number of lines containing the collision information. This number of lines is equal to the number of collisions in the system where each particle-particle collision is written once per particle and particle-wall collisions once. The header looks like,

```
# 0 0
# x0 y0 z0 x1 y1 z1
# dmin/2 dmax/2 0 0 0 0
```

where the current time is written in the first line of the header. The last line contains the minimum and maximum radii appearing in the system and there are several zeros added additionally which do not

have a function. The rest of the lines look like: `t i j c d ts fn ft un ut` containing the current time t , the involved particles i and j the location of the contact \underline{c} , the overlap δ , the length of the tangential spring ts , the force in normal direction $\|\underline{f}^n\|$, the remaining force in tangential direction $\|\underline{f}^t\| = \|\underline{f} - \underline{f}^n\|$ and the normal \underline{n} and tangential \underline{t} unit vectors.

4.1.3 Restart file

The `.restart` file saves information of the last written time-step containing system information such as the orientation of the gravity vector or the location of the walls. The location of the particles and additional properties like the inverse mass and inverse inertia values are also given in this file. The file can therefore be used to restart a simulation from that point on. The visualisation method uses this file to determine the number of fixed particles in the system by searching for all particles with an infinite mass. It also reads the information about the walls which is used to visualise them.

4.1.4 Ene file

The `.ene` file stores the energy information at each time-step for the whole system. It therefore consist of the current time, the potential energy, the kinetic energy, the rotational energy, the gravitational energy and the position of the centre of mass in the system.

4.2 Launch script

The launch script is a bash script in which VMD is launched with the default ‘execute a script’ (`-e`) and the ‘read arguments’ (`-args`) options allowed, see pseudocode 2. The `DPM.tcl` script is added to the execute option and the file-name and other input arguments, listed in table 4.3.1, to the input arguments option.

Pseudocode 2 Launch script

Require: ProblemName, InputArguments

Execute: `vmd -e sc/DPM.tcl -args ProblemName InputArguments`

4.3 Visualisation script

Loading the discrete data into VMD is done in several stages. The first step reads the input arguments (§4.3.1) which is followed by the gathering of other parameters from the `.restart` file (§4.3.2). After this step, VMD is prepared for the loading of DPM results (§4.3.3) by creating files which VMD can load on default. The data from the `.data` file is then loaded (§4.3.4) to reposition all particles at all loaded time-steps and some visualisation scripts for the particles (§4.3.5) and walls (§4.3.6) conclude the loading process.

4.3.1 Read arguments

The input arguments which were given by the `-args` flag in the `dovmd` script are checked with a simple `if` statement. Possible input arguments and their values are shown in table 4.3.1. Note that each variable has a default value which is not visible to the user.

4.3.2 Gather parameters

With the input arguments and problem-name at hand, it is possible to open the restart file and gather more parameters. Pseudocode 3 shows the procedure followed for this part of the code.

4.3.3 Prepare VMD

VMD should be prepared for the loading of DPM results. Therefore, a ‘molecule’ is created based on the PSF file generated by pseudocode 3. Frames are then added with use of the PDB file, see pseudocode 4. After this step, the ‘molecule’ has N_{max} atoms located in the origin, i.e. $(0, 0, 0)$, for all visualised time-steps where N_{max} is the maximum number of particles in the system.

Argument	Possible values
-Fstart	Select the start frame v . Value should be: v or end-v with $v \in \mathbb{N}$.
-Fend	Select the last frame v . Value should be: v or end-v with $v \in \mathbb{N}$.
-IA	Provide initial angle v of simulation. Value should be: $0.00 < v < 360.00$.
-WAIT	Provide animation delay v . Value should be: $v \in \mathbb{R} > 0$.
-DEBUG	Load DPM.tcl in debug mode providing more output.
-NOINFO	Load DPM.tcl with as less information as possible.
-NEWRESTART	Create restart file based on the last information in time-step. Only works for mono-disperse systems.

Table 4.1: Possible input arguments and their values.

Pseudocode 3 Get input

Require: RestartFile**Open:** RestartFile**Save:** All time related and wall information, the current number of particles including the current number of fixed particles, inclination angle.**Create:** ‘Protein Structure File’ (PSF) and ‘Protein Data Bank’ (PDB) files containing the current number of particles in the origin and stating that no molecular structure exist.

Pseudocode 4 Prepare VMD

Require: PSF and PDB files, ProblemName, Fstart, Fend**Open:** PSF file**Add:** PDB file to the created ‘molecule’ for Fend–Fstart frames.

4.3.4 Load data

All the information from the `.data` file is passed into VMD with this function, see pseudocode 5. The function moves all particles according to the `.data` file. Note that this data is accessible in VMD by the `atomselect` command which is explained in the VMD user’s guide [16].

Pseudocode 5 Read data

Require: DataFile, Fstart, Fend**Open:** DataFile**Read and set:** fixed particle information and set it for all frames.**Read and set:** moving particle information per frame.

4.3.5 Show particles

The particle representations, as one can find in the “VMD>Graphics>Representations” menu, are split in one for fixed and one for moving particles. The VMD particle variable `user` is used to separate moving (`user ≥ 0`), fixed (`user = 1`) and unused particles (`user = 2`) from one-another. Moving particles are default coloured by speed, fixed particles are black and unused particles are hidden and located in the origin. The same menu allows the user to reduce the number of particles shown by adding logical expressions to the selection text. It is also possible to change the colouring method or render quality.

4.3.6 Show walls

The `DPM.tcl` script is also able to draw (finite) walls. Intersection points of the domain are calculated based on the normals and positions in the `.restart` file and used to draw multiple triangles per wall. By default all walls are hidden but, when the “VMD OpenGL Display” is active, they can be shown by pressing the `w` key.

Chapter 5

Results

The analysis of the output of the simulation based on the set of parameters shown in chapter 3 which ran for five days containing 500,000 particles simulating several seconds is shown in this chapter. The chapter starts with the discussion of the discrete results §5.1 which are compared to the original work by Johnson and Gray [17]. These discrete results are averaged in multiple directions by the coarse graining method as described in §2.3. The influence of the coarse graining width is discussed in §5.2 whereafter the method is applied. A steady state exist in the system, see §5.3, which allows for noise reduction by time averaging of the results. This is followed by the validation of the continuum assumption with use of the Knudsen number in §5.4. The enclosed region is identified by the Froude number (§5.5) whereafter the height of the flow is considered (§5.6). Combination of these two sections yield the characterisation of the enclosed region in §5.7. Note that the simulations up to this point are based on a simulation with inclination angle 26.7° and effective falling height of 5 cm which are equivalent with the published set of initial values in the original work. Simulations with different inclination angles and falling heights form a parameter study §5.8. This parameter study is even further extended to a highly kinetic flow which is discussed in §5.9.

5.1 Discrete results

Mercury [26] is used to apply the Discrete Particle Method onto the problem at hand. It is shown in chapter 3 that the inflow of particles is controlled by a set of fixed particles forming a truncated cone and thus a funnel. This section starts with the analysis of the particle flow through this funnel (§5.1.1) followed by the impingement of the resulting jet on the plane (§5.1.2). A complete overview of the discrete results is given in §5.1.3 which is followed by a more detailed look at the hydraulic jumps in §5.1.4. All the figures are in orthographic projection which is a form of parallel projection to represent three-dimensional results in two dimensions. The domain of the problem is limited by the values shown in table 3.1 with the x coordinate increasing in down-slope direction of the plate, the y coordinate increasing over the width of the plate and the z coordinate increasing in the perpendicular distance to the plate.

5.1.1 Funnel

The funnel is used to create a dense jet of particles originating from the falling height. A dense outflow is created when particles have several collisions before the end of the funnel is reached. Figure 5.1 shows a 7 mm deep cross sectional view of the funnel at four different times during the simulation in two colouring methods. These times represent the times in which the first particles are created ($t = 0.03$ s), the first particles are leaving the funnel ($t = 0.06$ s), a non-dense flow is leaving the funnel ($t = 0.12$ s) and the final dense flow is established after $t = 0.21$ s. One can see that the initial set of particles falls through the funnel without enough collisions with the funnel and other particles. Therefore, the initial outflow, shown in sub figures (c) and (g), is faster than the steady dense flow shown in sub figures (d) and (h). Additionally, the flow is fully formed by the initial set of particles. The dense flow is a mixture of particles where the particles which are created initially form the outside and the particles which are created in a later stage form the inside of the jet. This phenomenon is caused by the collisions in the lower regions of the funnel. These colliding particles decrease both the inflow speed and the effective inflow area which result in the dense and stable outflow with a velocity of approximately 0.30 m/s.

This velocity increases to approximately 1 m/s when it reaches the impingement zone due to the falling height of 5 cm. Such a velocity is equivalent with the jet velocity described by Johnson and Gray [17] and is in good agreement with the velocity estimated by conservation of energy.

5.1.2 Impingement

The dense flow originating from the funnel which is discussed in §5.1.1 should result in a relatively smooth transition in the direction of the flow at the impingement zone. Figure 5.2 shows a 5 mm deep cross section of this zone where the x direction is truncated at $x = 0.01$ m and $x = 0.05$ m, the y direction at $y = 0.075$ m and $y = 0.080$ m and the z direction at $z = 0.02$ m. The centre of the impingement region can be seen from (d) as being $x = 0.03$ m. From sub figures (a) and (b) one can see that the initial, non-dense flow causes a lot of particles to bounce off the plate, forming a sparse cloud. The smooth transition from the direction of the jet, which is the gravity direction, into the direction of the plate establishes as soon as the jet is dense enough. The impingement zone grows in the up-stream direction for approximately two seconds while the down-stream flow becomes steady directly. A proposed flow profile near the impingement region is shown in figure 5.3(a). This profile originates from Johnson and Gray [17] and it shows that the thickness of the flow in both up- and down-slope directions is dependent of the jet thickness. Furthermore, a neutral line shows the line where the particles collide perpendicular with the plate yielding a stagnation point. A corresponding figure based on the numerical results is shown in figure 5.3(b) where the particles are coloured based on their down-slope velocity. The stagnation point is the point where the neutral line coincide with the plate is also visible in the DPM results. It is caused by vertical pressure which is quickly build up above this point and the resulting flow after the stagnation point is radial. The flow through the impingement zone for the highly kinetic jet is coarse grained in §5.9.7 where lines of typical flow paths are added to validate the proposed model.

5.1.3 Plate flow

The flow after impingement forms a hydraulic jump in the down-slope direction of the plate. This can be clearly seen from figure 5.4 where the system is represented in a orthographic projection perpendicular to the plate resulting in a so-called ‘top view’ and the particles are coloured based on their speed. These figures show the system at six times with an interval of 0.6 s. Sub-figure (a) shows a small hydraulic jump with an open end in the down-slope direction of the flow. A slightly further evolved solution is shown in sub-figure (b) where the flow has grown in the both the down-slope and over the width of the plate. This region is formed by the existence of a hydraulic jump which is created in the up-slope direction of the impingement zone and a zoomed view is shown in figure 5.5. This jump then propagates in the down-slope direction while closing the region. An enclosed region can be identified after $t = 1.82$ s and the shape of the region does not change when time evolves. Therefore, it is expected that the flow near this region is in a steady state from this point on. One can also see that the flow further down the plate is not in steady state; the flow still widens. The characteristics of the enclosed region are discussed based on the coarse grained results in which it is more distinguishable and shown in §5.7.

5.1.4 Hydraulic jump

The flow in the enclosed region is discharged into a zone of lower velocity yielding the abrupt conversion of kinetic energy into potential energy. Theoretically, this conversion yields a sudden raise in the height of the flow which is known as a hydraulic shock. Finite volume methods can calculate these shocks while DPM cannot simulate infinite gradients. A hydraulic jump is therefore sought which has a finite gradient at the location of this discharging. Figure 5.6 shows 1 mm deep cross sectional views at four different times of the plate located at $x = 0.04$ m. This location corresponds with a slice of the plate which is located 1 cm in down-slope direction of the impingement location. Moving particles are coloured by their speed and the fixed particles are hidden. The figures show the establishment of such a jump with respect to time. Initially, see sub-figure (a), several airborne particles flow over the plate and eventually land (b) to form the base of the slow moving flow. From this point on, the fast flowing region then discharges into the slower flow allowing the hydraulic jump to grow in both width and height. The jump stops growing after $t = 0.97$ s for this location on the plate. One can see that the jump is not as steep as it is predicted by the finite volume results from which a typical example

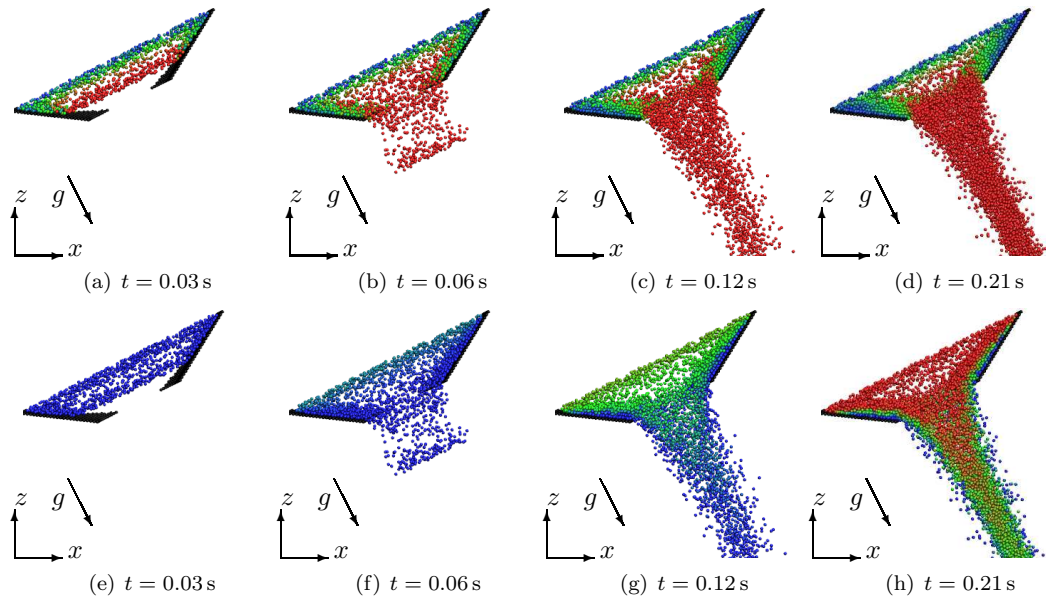


Figure 5.1: Cross sectional views of the flow through the funnel for $0.075 \text{ m} < y < 0.082 \text{ m}$. Fixed particles forming the funnel are coloured black and the moving particles are coloured based on speed in (a)-(d) increasing from $\|U\| = 0 \text{ m/s}$ (blue) to $\|U\| \leq 0.25 \text{ m/s}$ (red). The moving particles in figures (e)-(h) are coloured by moment of creation where blue particles correspond to $t = 0.00 \text{ s}$ and red to $t = 0.21 \text{ s}$.

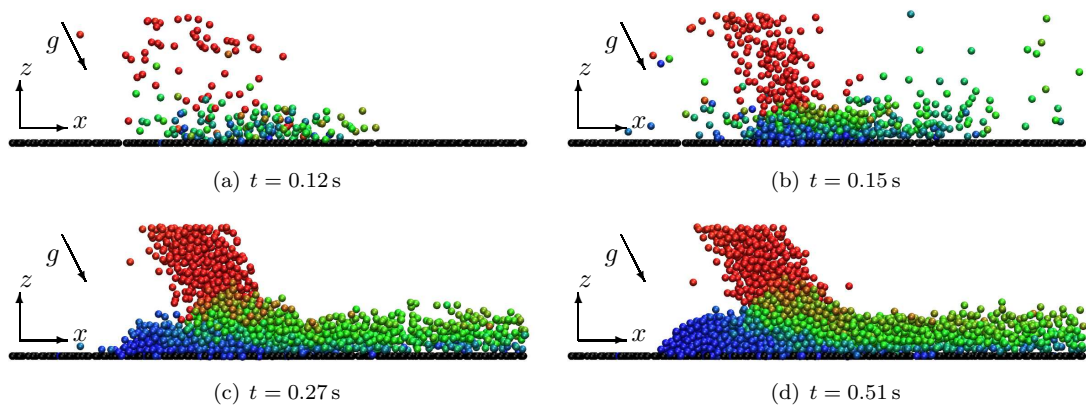


Figure 5.2: Cross sectional view of the impingement zone at four times for $0.075 \text{ m} < y < 0.080 \text{ m}$. Fixed particles are coloured black while moving particles are coloured by speed where red corresponds to a speed of 2 m/s , green to a speed of 1 m/s and blue to a speed of 0 m/s .

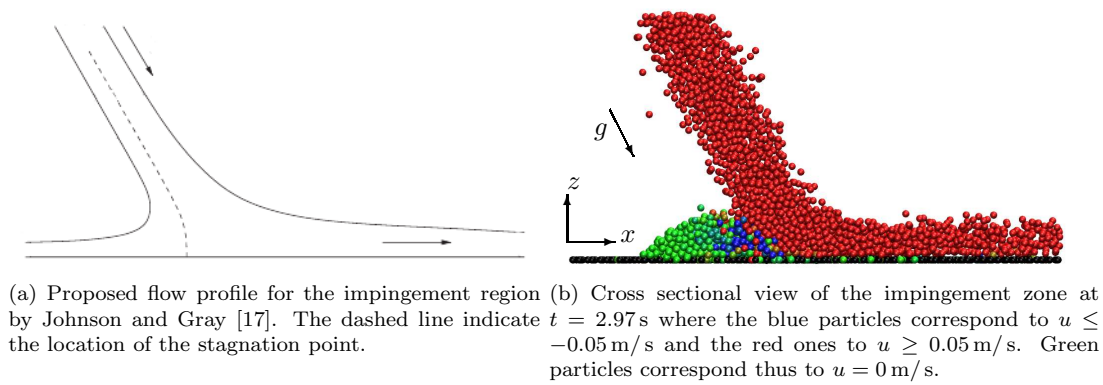
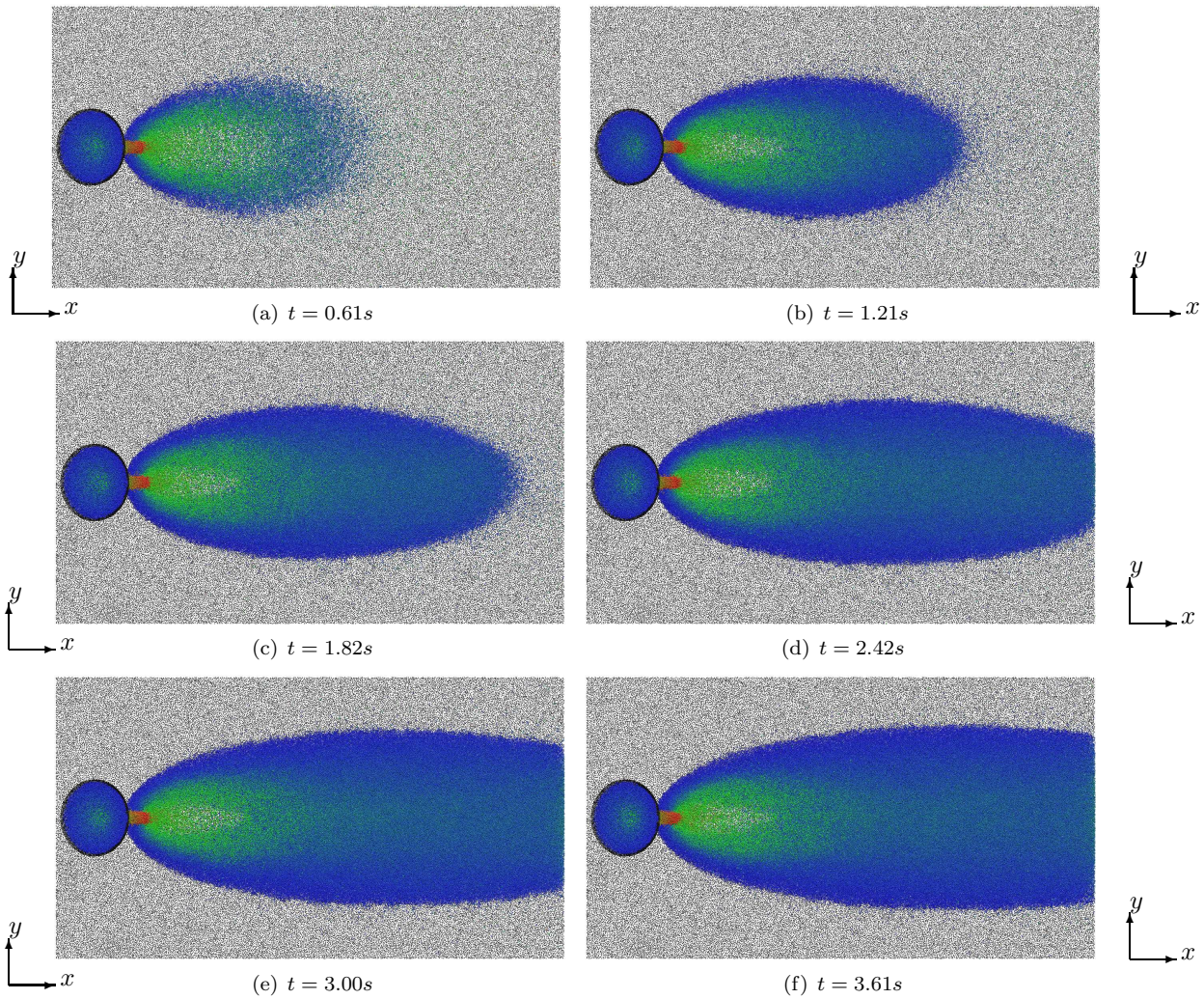


Figure 5.3: Flow profiles for the impingement region.

Figure 5.4: The top view of the numerical outcome of the flow over the plate at six different times where blue particles correspond to $\|U\| = 0\text{ m/s}$ and red particles to $\|U\| = 1\text{ m/s}$.

is shown in figure 5.7. This figure shows the height of the flow for a similar cross section. Further analyses, based on the coarse grained results, is needed to confirm the difference in the strength of the jump and is shown in §5.6.

5.1.5 Conclusion

Section 5.1.1 showed that the funnel is being filled such that the outflow is a dense and stable flow which is required in order to mimic the experiments. It is not likely that the less dense initial outflow has an influence on the simulation results in a later stage. The inspection of the flow at the impingement zone confirmed this hypothesis since the resulting shape of the flow is equivalent with the, by Johnson and Gray, proposed flow profile near the impingement zone. The transition caused a hydraulic jump which is the base for the final flow profile over the whole plate. Section 5.1.3 showed the flow over the plate where an enclosed region of thin fast-flowing flow is formed causing a hydraulic jump (§5.1.4). The encountered jump differs from the finite volume results in the strength of the jump. Comparable coarse grained results for the hydraulic jump are shown and further discussed in §5.6.

5.2 Coarse graining parameters

Applying the statistical method as described in §2.3 is only as accurate as the coarse graining width w . The influence of individual particles in a sparse cloud of particles is bigger when this width is small since individual particles then have a high contribution to the averaged solution. On the other hand, other phenomena with steep gradients are smoothed out when this width is chosen to be big. In order to achieve the right accuracy, a sensitivity study is performed on the statistical method resulting in a coarse graining width which is used in the rest of the thesis. This study shows three cases for the coarse graining width $w = 0.00500$ m, 0.00250 m and 0.00125 m which correspond to $w = 8.33d$, $4.17d$ and $2.08d$ respectively. The typical volume fraction φ is determined in §5.2.1 which is needed in the calculation of the height of the flow. The two sections thereafter consider this height h (§5.2.2) and the macroscopic speed $\|U\|$ (§5.2.3). A conclusion is drawn on the coarse graining width is drawn in §5.2.4.

5.2.1 Typical volume fraction

The incompressible assumption made in §2.2.4 should hold in the steady uniform flow which is formed outside the enclosed region. This assumption implies that the height of the flow h can be characterised by introducing a typical volume fraction φ based on the length of the z -domain Z ,

$$h = Z\bar{\nu}/\varphi, \quad (5.1)$$

where $\bar{\nu}$ is the depth-averaged volume fraction which is computed by depth-averaging the volume fraction ν ,

$$\nu = \sum_i^{N_m} v_i \mathcal{W}_i, \quad (5.2)$$

where v_i is the volume of particle i . From (2.122) it is known that,

$$\hat{\bar{\sigma}}_{zz} - \hat{\bar{p}} = -\frac{\hat{h}^2}{2} \cos \zeta + \mathcal{O}(\varepsilon), \quad (5.3)$$

should hold for the dimensionless system of equations. Note that dimensionless variables are indicated with a hat. However, the statistics are performed on the non-dimensionless results and an equivalent relation is found by back-substitution of the scale relations proposed (2.85) into (5.3) where H is replaced by Z . Furthermore, the first order error term is neglected, hence,

$$\frac{\bar{\sigma}_{zz} - \bar{p}}{\rho g Z} = -\frac{(h/Z)^2}{2} \cos \zeta. \quad (5.4)$$

The density used in this equation is the bulk density which is computed by $\rho = \rho_p \varphi$, i.e. it is assumed that the steady uniform flow has a constant density. A relation for the typical volume fraction is found by substituting (5.1) into (5.4). The notation for variables with dimensions is omitted, yielding,

$$\varphi = \frac{-\rho_p g \bar{\nu}^2 Z \cos(\zeta)}{2(\bar{\sigma}_{zz} - \bar{p})}. \quad (5.5)$$

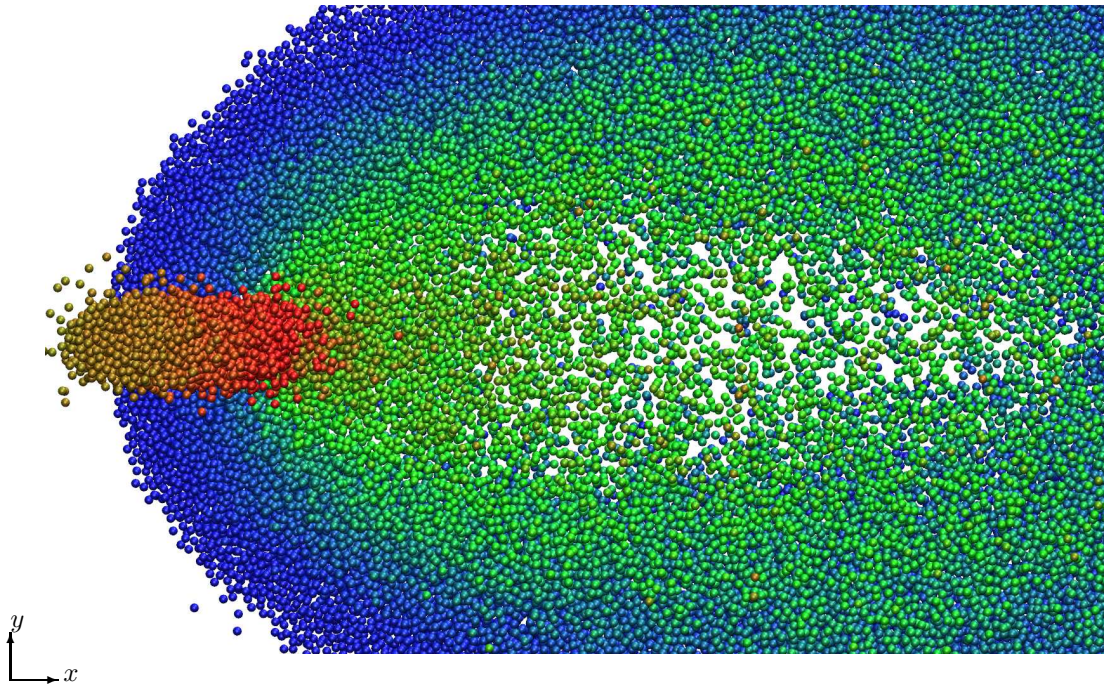


Figure 5.5: Zoomed top view of the enclosed region in which the moving particles are coloured by speed where blue particles correspond to a speed $\|U\| = 0$ m/s and red particles to $\|U\| = 1$ m/s. Fixed particles are hidden.

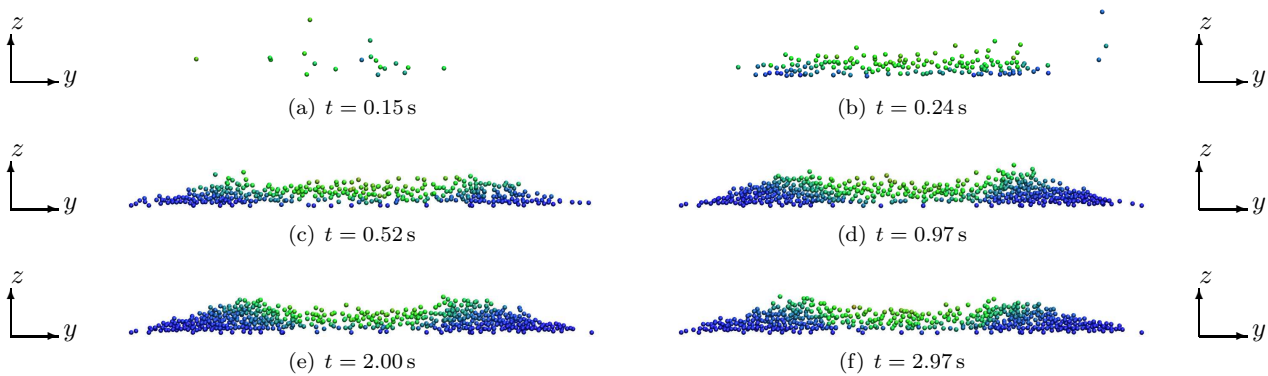


Figure 5.6: Cross sectional views from $x = 0.040$ m up to $x = 0.041$ m for the hydraulic jump in the system. Blue particles correspond to $\|U\| = 0$ m/s and red particles to $\|U\| = 1$ m/s. Fixed particles are hidden.

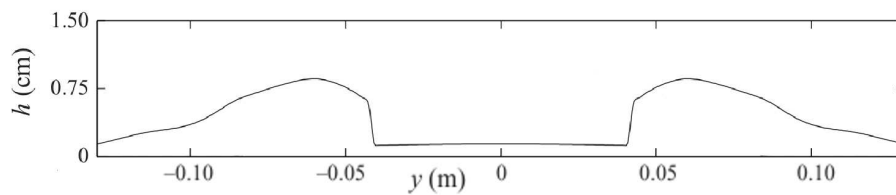


Figure 5.7: Cross sectional view of a typical height solution from the finite volume results in the original work [17].

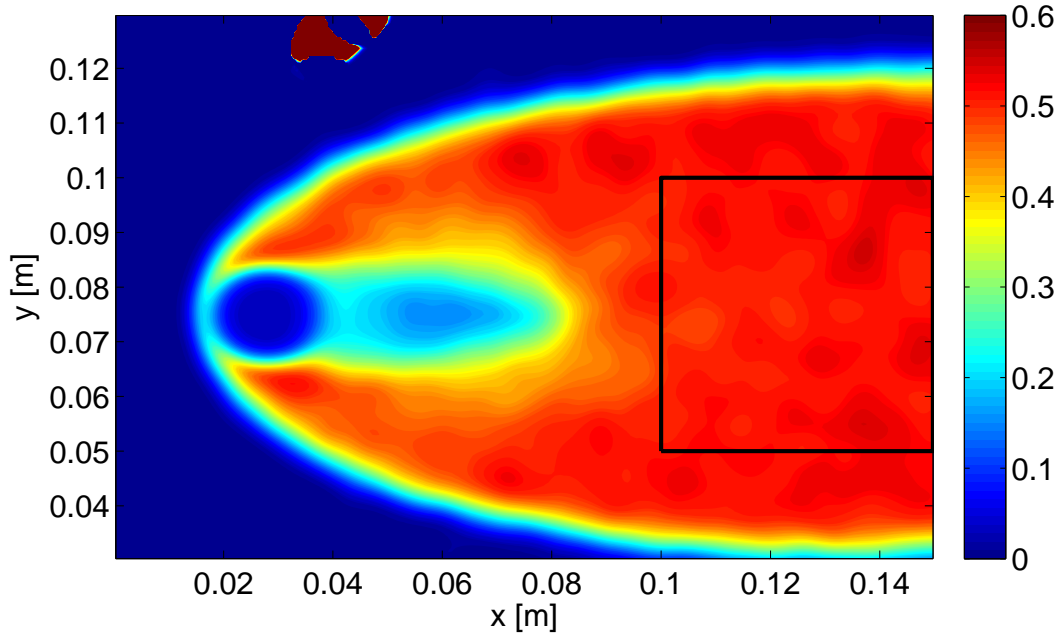


Figure 5.8: Contour plot of the typical volume fraction where the funnel is neglected and the coarse grained function is evaluated each 0.001 m in both x and y directions. The average value of the typical volume fraction is calculated by the values in the boxed area where the box is given by $0.10 \text{ m} \leq x \leq 0.15 \text{ m}$, $0.05 \text{ m} \leq y \leq 0.10 \text{ m}$.

This typical volume fraction is, due to the density assumption, only valid in regions of steady uniform flow [30]. Figure 5.2.1 shows a high resolution graph in which the typical volume fraction for a part of the domain is shown. The value is approximately constant in the black boxed area while it is not in the highly kinetic area. The average value of the typical volume fraction within the boxed area is 0.516 which is in agreement with values found in Weinhart *et al.* [30] for thin steady uniform flows. This value is therefore used in the calculation of the height of the flow.

5.2.2 Height

The height is defined as the height of the flow perpendicular to the plate and it can be calculated, see Eq. (5.1), under the assumption that the typical volume fraction φ in each cell is constant as explained in §5.2.1. Such a cell is fully determined by the size of the problem and the number of evaluated points in this system. Coarse grained flow heights at $t = 2.97 \text{ s}$ for the three coarse graining widths are shown in figures (a), (c) and (e) within figure 5.9. The small red region in the left side of the graph is due to the influence of the funnel. Further down the plate the enclosed region of thin flow can be identified and a steady avalanche is formed after this enclosed region. The coarse graining width has an influence on the visible gradients near the boundaries of the enclosed region which can be seen when the figures belonging to $w = 0.0025 \text{ m}$ and $w = 0.0050 \text{ m}$ are compared. The lowest value of the height in the enclosed region is also dependent on this coarse graining function.

5.2.3 Speed

The coarse grained velocity U is calculated by the ratio of the coarse grained momentum and the coarse grained density, see (2.142). A macroscopic speed, where fluctuations of the velocity component in z direction are neglected, is then defined as,

$$\|U\| = \sqrt{U_x^2 + U_y^2}, \quad (5.6)$$

and figures (b), (d) and (f) within figure 5.9 show the speed at $t = 2.97 \text{ s}$. One can see that the influence of the coarse graining width within the enclosed region is negligible when $w \leq 0.0025$. The

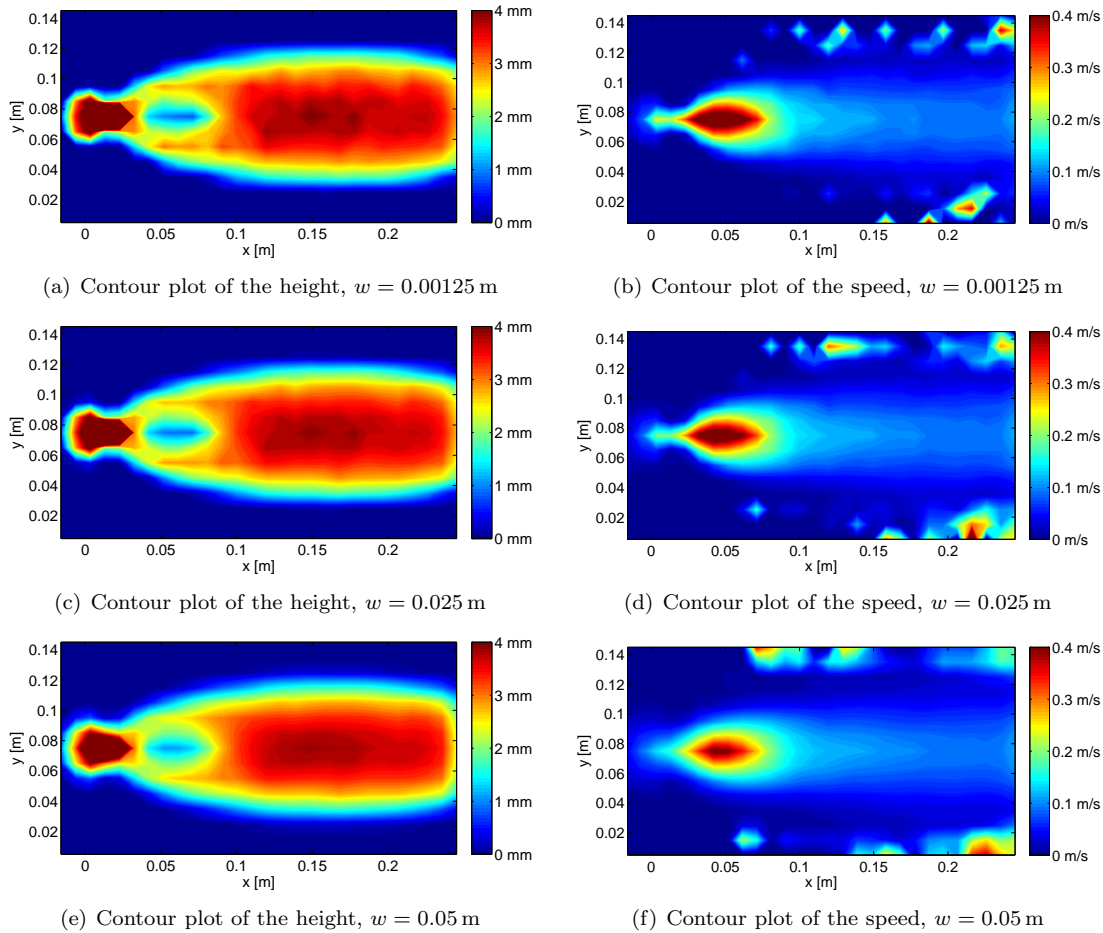


Figure 5.9: Typical coarse grained results for the projected and scaled height and velocity where the coarse grained values are evaluated with a grid spacing of 0.01 m in both x and y directions.

down stream results do not significantly change under the influence of the coarse graining width which is due to the many particles in that region. However, airborne particles have a high speed and are the only particles in several regions of the flow. This can be seen by the several high velocity regions on the sides of the plate and their influence localises with a smaller w .

5.2.4 Conclusion

The typical volume fraction of 0.516 is calculated in §5.2.1 and showed good agreements with predictions in Weinhart *et al.* [30]. The value is used in the calculation of the coarse grained height and speed of the flow. From the first of these, one could conclude that a coarse graining width of $w \leq 0.0025$ m is small enough to capture all the details of the height of the flow. The graphs of the speed confirmed this conclusion, especially when the influence of w within the enclosed region is considered. The few airborne particles causing the high speed peaks in the speed graphs can be neglected since they are not considered to be part of the flow. A coarse graining width of $w = 0.0025$ m is therefore chosen in further analysis of the results.

5.3 Steady state

The flow down the plate should form a steady state as it is implied in Johnson and Gray [17]. This section starts with the definition and general idea of a steady state §5.3.1. Thereafter, the growth of the number of particles in the system with respect to time is investigated in §5.3.2. A time-averaged solution for the height h and macroscopic velocity u are then compared to the solution at $t = 2.97s$ (§5.3.3).

5.3.1 Definition of steady state

A steady state for some quantity Q is achieved when the change of this quantity with respect to time is zero, or mathematically,

$$\frac{\partial Q}{\partial t} = 0. \quad (5.7)$$

Such a steady state normally arises after a transient state in which the problem is initialised. The problem at hand has such a transient state and from figure 5.4 it is estimated that solutions near the enclosed region stabilise around $t = 2s$ and that the flow further down the plate does not reach a steady state for the time it is simulated. This time will be taken in §5.3.3 where a time-averaged solution is compared to the solution at the last time step.

5.3.2 Number of particles

The total number of moving particles in the system is a quantity which should become steady implying that accumulation of particles should not happen. The widening of the flow, which can be seen from figure 5.4, indicate that accumulation takes place in several parts of the system after three seconds of simulation. A sub-domain, which stops after the kinetic regime, is therefore considered in the calculation of the mass flow. This sub-domain ranges over the full width of the plate and up to $x \leq 0.15$ m in the length of the plate. In general, the mass flow should satisfy,

$$\dot{N}_{acc} = \dot{N}_{in} - \dot{N}_{out}, \quad (5.8)$$

where the number of inserted particles until time t , $\dot{N}_{in}(t)$ should be equal to the outflow $\dot{N}_{out}(t)$ and accumulation $\dot{N}_{acc}(t)$ of particles. The rate of accumulation of particles should be zero in a steady state system. This yields that the inflow rate should be equal to the outflow of particles in the sub-domain from which the inflow can be derived from the total number of particles in the system which is shown in figure 5.10(a). One can see that the initial influence of a non-dense flow through the funnel is negligible and that a linear growth of particles is thereafter established. The linear growth rate is equal to 95,500 particles per second for the funnel with a diameter of 0.015 m which can be seen from the first plateau in figure 5.10(b) where the time derivative of figure 5.10(a) is shown. This time derivative can also be interpreted as the accumulation of particles and the drop in this curve is due to the outflow of particles over the edges of the domain in x and y direction. The remaining value of the curve at $t = 3$ s confirms that a steady state in the whole domain does not exist. Note that the mass flow in experiments is given by a scaling law [2],

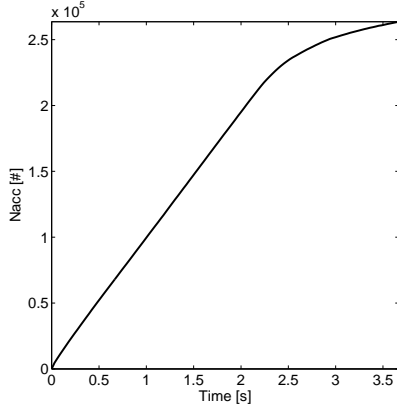
$$Q = \frac{0.29\pi\rho_p\sqrt{g}D^{5/2}}{m_p}, \quad (5.9)$$

yielding a inflow of approximately 700,000 particles per second for the same conditions. The number of particles flowing through cross sectional areas over the length and width of the plate per unit time is given by,

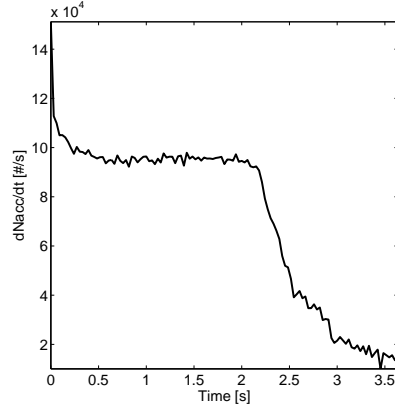
$$\dot{N}_{out}^x(x) = \int_{y_0}^{y_1} \int_{z_0}^{z_1} \frac{P_x}{m_p} dy dz, \quad (5.10)$$

$$\dot{N}_{out}^y(y) = \int_{x_0}^{x_1} \int_{z_0}^{z_1} \frac{P_y}{m_p} dx dz, \quad (5.11)$$

using the momentum P in the respective flow direction and m_p as the mass of a single particle. Figures 5.10(c) and 5.10(d) show the particle flow per second at $t = 2.97s$ where the outflow of particles is calculated for area's over the width and length of the plate respectively. The first figure shows that the particles are moving in $\pm y$ direction depending on their y coordinate with respect the the y coordinate of the impingement zone which is $y_{imp} = 0.075$ m. It also shows that the outflow of particles through



(a) Accumulation of particles against time



(b) Accumulation rate of particles against time

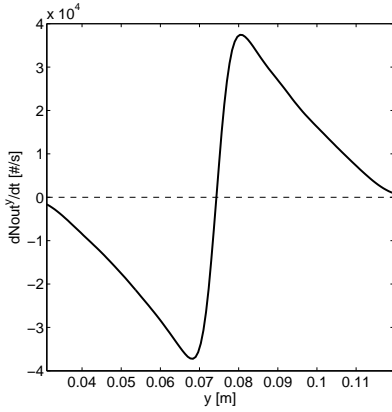
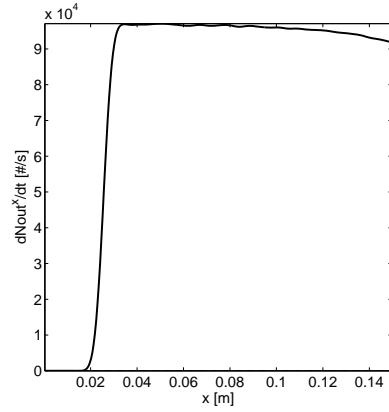
(c) Particle rate through a cross section of the domain perpendicular to the y axis at time $t = 2.97$ s(d) Particle rate through a cross section of the domain perpendicular to the x axis at time $t = 2.97$ s

Figure 5.10: Time dependency of the number of particles and the flow of particles over the boundaries in which dashed lines show the 0 line.

the domain edges, $y = 0.00$ m and $y = 0.15$ m, is negligible. On the other hand, figure 5.10(d) shows the flow of particle in the x domain where the outflow of particles through $x = 0.15$ m is calculated by taking the average flow in the range of $0.05 \text{ m} \leq x \leq 0.15 \text{ m}$ which corresponds to the steady uniform flow discussed in §5.1. This yields an outflow of approximately 96,500 which overestimates the inflow by 1% which is acceptable. Further analyses of the possible steady state within the sub-domain is shown in 5.3.3 where the resulting flow is compared with the time averaged flow.

5.3.3 Time averaged statistics

A second check is based on time averaging of the coarse grained results in which the results at $t = 2.97$ s are compared the time averaged results of the last second in the simulation. Figures (a) and (c) within figure 5.11 show top views of the sub-domain in which the height and velocity are plotted at $t = 2.97$ s. The coarse graining width used to produce these graphs is $w = 0.0025$ m and one can distinguish the kinetic regime by the low height and high velocity values. Figures (b) and (d) show similar graphs but now based on the time-averaged solution. Even though the height graphs ((a) and (b)) are very similar, significant differences can be identified when the velocity graphs ((c) and (d)) are compared. These differences are due to the airborne particles which have a high influence on the time-averaged statistics. The deviation of the final solution with respect to the time-averaged solution is then given by,

$$h_E = \frac{|h_{t=2.97} - h_{avg}|}{h_{avg}} * 100\%, \quad \|U\|_E = \frac{\| \|U\|_{t=2.97} - \|U\|_{avg} \|}{\|U\|_{avg}} * 100\%, \quad (5.12)$$

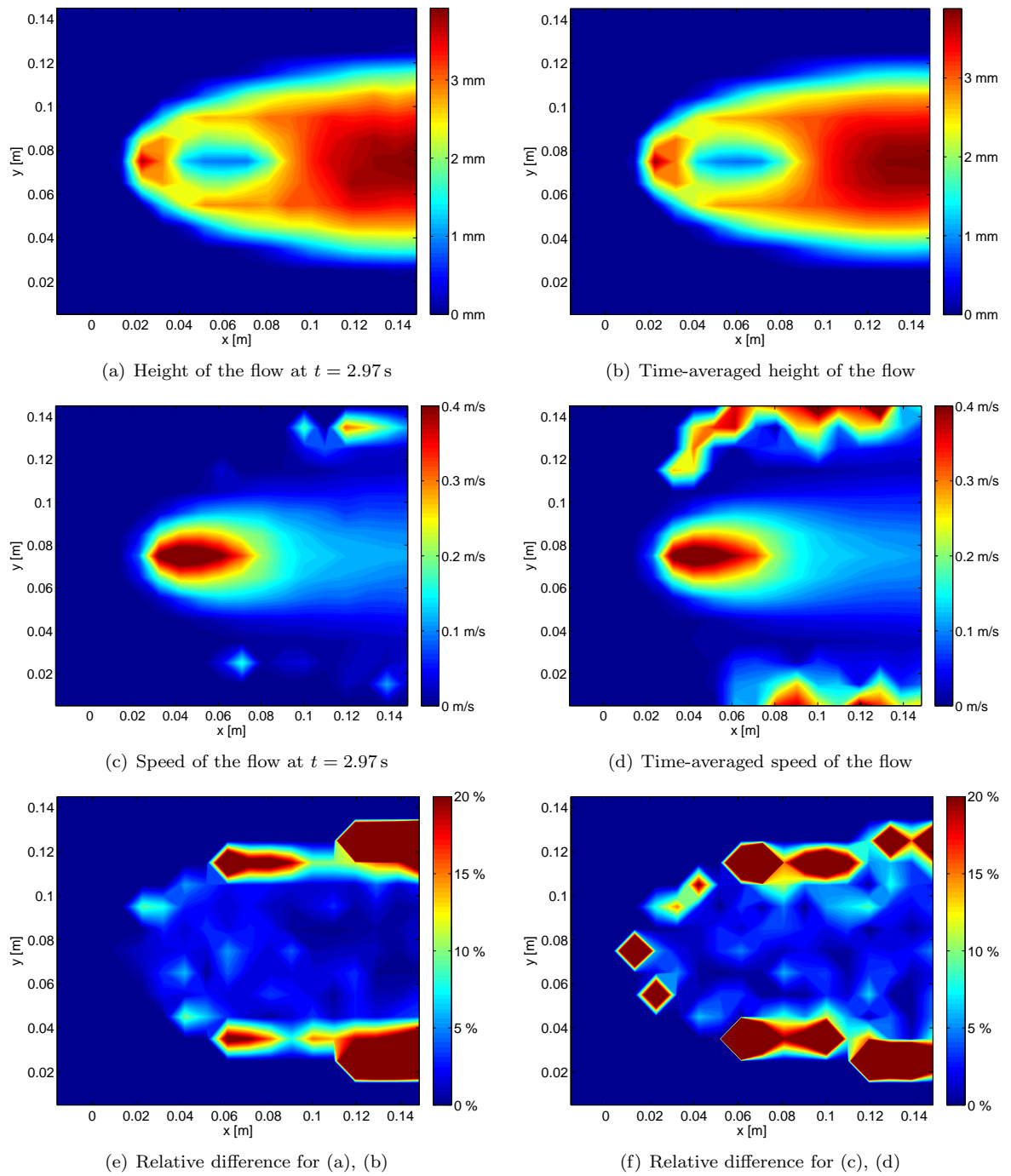


Figure 5.11: Coarse grained height and speed contour plots for the sub-domain in which cells with less than 10 particles are neglected in (e) and (f). The values are evaluated with a grid spacing of 0.01 m in both x and y direction.

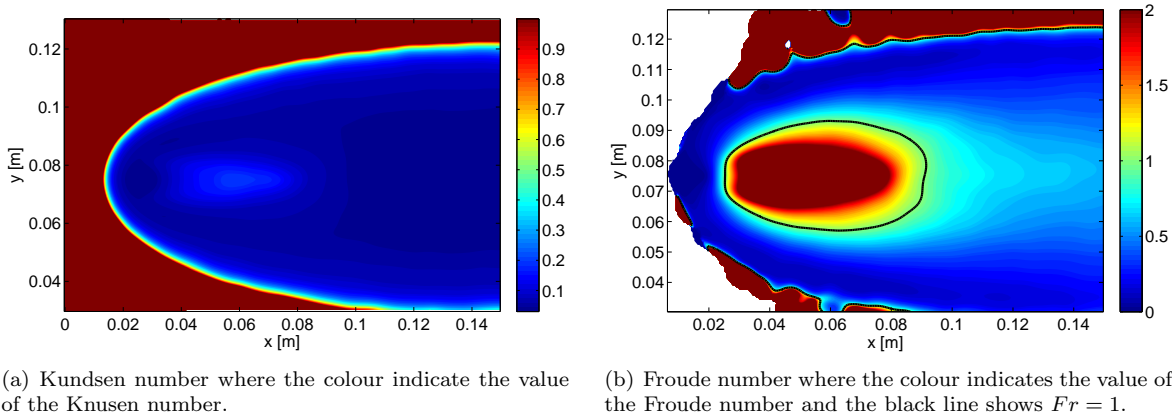


Figure 5.12: Top view of the Knudsen and Froude numbers in the flow for the sub-domain. The functions are evaluated on a x, y grid with a uniform spacing of 0.001 m.

and the corresponding values are shown in figures (e) and (f) within figure 5.11. Note that cells with less than 10 particles are neglected in the calculation of the differences where this number is calculated for mono-disperse systems by,

$$N_{cell} = \frac{v_{cell}}{v_{particle}} \nu = \frac{6}{\pi d^3} \frac{X}{n_x} \frac{Y}{n_y} \frac{Z}{n_z} \sum_{i=1}^{N_m} v_i \mathcal{W}_i, \quad (5.13)$$

in which n_x, n_y and n_z denote the number of cells in the respective direction, X, Y and Z the length of the corresponding domain edges and v_i the volume of particle i . One can see from the figures that the error in the enclosed region is lower than 10% for both graphs and that differences bigger than 20% occur on the boundary of flow. The former confirms the hypothesis that the enclosed region reaches a steady state within two seconds of simulation where the latter indicates that the flow is still widening.

5.3.4 Conclusion

This section discussed the definition of a steady state, the growth of the number of particles with respect to time and a comparison of the final solutions for height and speed with respect to a time-averaged solution. Even though the presence of accumulation of particles in the system it is concluded that a sub-domain exist in which the inflow of particles is balanced by the outflow of particles. Moreover, time-averaged solution strengthens the hypothesis that the enclosed region reaches a steady state. However, the flow within the sub-domain is still widening implying that the slower regions are not in a steady state yet. The results from this section allows the usage of time-averaged and coarse grained results for the enclosed region, causing a reduction of time dependent noise in the dense regions of the flow.

5.4 Knudsen number

The derivation of the granular shallow flow equations is based on the assumption a continuum is considered. The Knudsen number, as given in (2.38) and (2.183), is a measure to validate this assumption. It is defined as the ratio on the mean free path of a particle, which is the distance in-between two collisions, and the typical length scale, i.e., the maximum distance a particle may travel. The number should satisfy the condition $Kn \ll 1$ for continuous collisional flows and the results for the sub-domain are shown in figure 5.12(a). The figure clearly identifies that the flow in the whole domain can be considered as a continuum since it satisfies the stated condition in all regions containing a significant amount of particles.

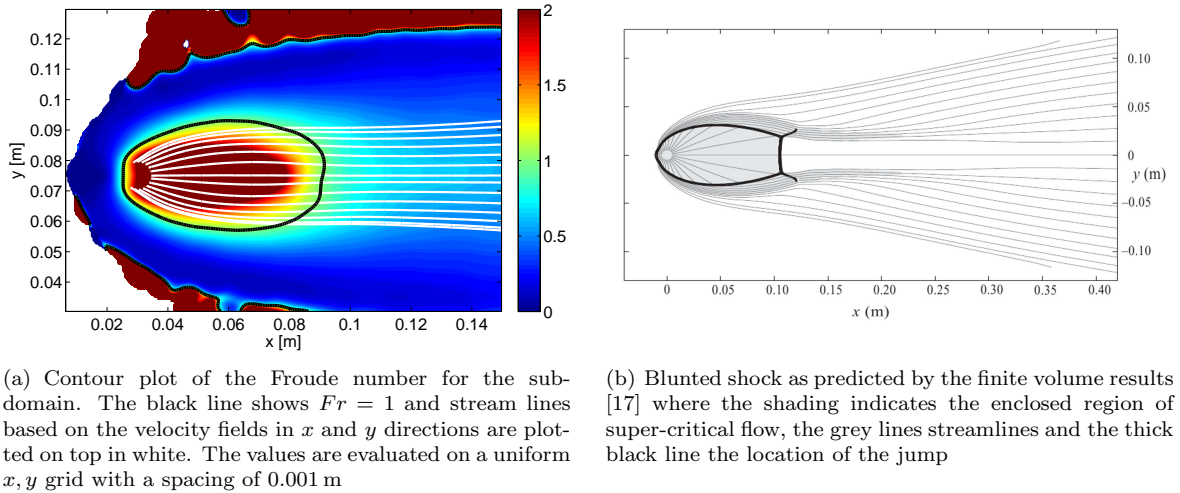


Figure 5.13: Comparison of DPM and finite volume results yielding a blunted shock.

5.5 Froude number

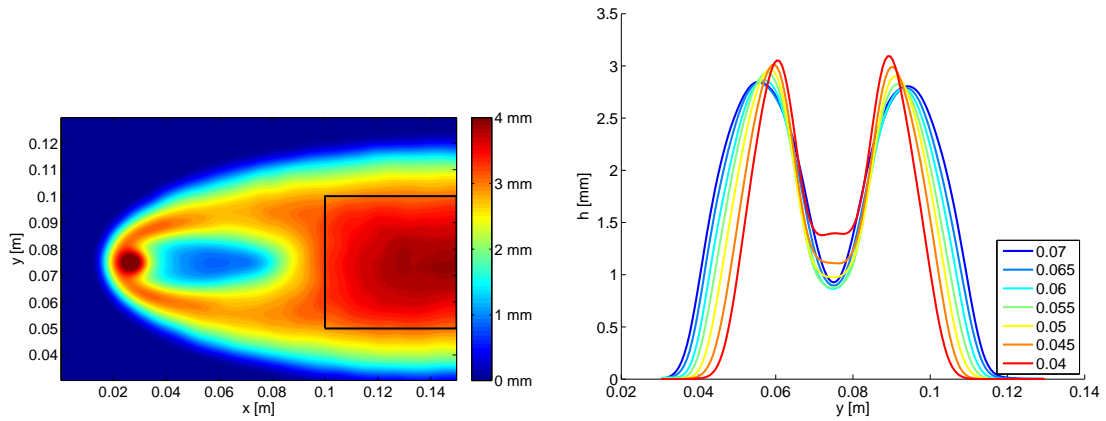
The Froude number is defined as the ratio of the flow velocity over the gravitational wave velocity as shown in (2.178). Therefore, it can be seen as a measure to distinguish ‘sub-’ from ‘super-’critical flow where the former corresponds to $Fr < 1$ and the latter to $Fr > 1$. The number identifies regions in which any kind of information can propagate in up-stream direction, i.e. the gravitational wave velocity is bigger than the flow velocity which is necessary for the formation of hydraulic jumps. The enclosed region is identified with a line corresponding to $Fr = 1$ since it is completely surrounded by a hydraulic jump. This jump identifies the places where the type of the flow changes from super- to sub-critical or visa versa. Figure 5.12(b) shows the top view of the sub-domain where the colour corresponds with the Froude number. Furthermore, the level at which the number is equal to unity is shown by a black line indicating the separation of the different types of flow. White area’s correspond to regions without particles and there are numerical artefacts present in area’s with low density. Another figure, where typical particle paths originating near the impingement zone are added to the top view of the Froude number, is shown in figure 5.13(a). One can see that the enclosed region is similar to the blunted shock as predicted by the finite volume results, see figure 5.13(b) and that the flow direction is radial within the enclosed region. Even though the three-dimensional trench, which is seen in the experiments and finite volume results, is absent in the down-stream end of the enclosed region, similarities with the finite volume results can be seen in the direction of the flow at this location. The particle paths through the middle of the blunted shock are parallel where the others show a diverging behaviour similar to the streamlines shown in figure 5.13(b).

5.6 Flow Height

One of the important characteristics of the flow is its height since this quantity is directly related to the strength of the hydraulic jump. Section 5.1.4 showed cross sections of the flow 1 cm in down-slope direction after the impingement zone in which the jump was visible but not as strong as predicted by Johnson and Gray, see figure 5.7. Top views of the height are shown in figure 5.9 where they were used to determine the coarse graining width. This section shows a top view of the height within the sub-domain in §5.6.1 and cross sectional views in §5.6.2 to determine the characteristics of the hydraulic jump. Conclusions are drawn in §5.6.3.

5.6.1 Top view

Figure 5.14(a) shows a top view of the sub domain in which the enclosed region is clearly visible. The resulting shape of the region differ from the one found by the finite volume results in the sharpness of the closing end of the region. The finite volume results predicted a so-called teardrop shock for the set



(a) Top view of the height of the flow for the sub-domain where height is shown by colour and the boxed area is used to calculate the average height of the flow in that area.

(b) Cross sectional views of the height of the flow over the width of the plate in the range $0.04 \text{ m} \leq x \leq 0.07 \text{ m}$

Figure 5.14: Height figures

of parameters used which was confirmed by the experiments but not by the DPM results. Nevertheless, a hydraulic jump can be seen which is closer investigated in §5.6.2 where cross sections of the flow in the enclosed region are shown. The figure also shows that the average height of the flow inside the enclosed region is 1.95 mm with a minimum of 0.86 mm at $x = 0.0595 \text{ m}$, $y = 0.075 \text{ m}$. The height outside the enclosed region settles to a value of 3.52 mm on average in the boxed area. Corresponding values for the original work are estimated as 1 mm within the enclosed region and 14 mm in the steady flow. The DPM results calculate the height within the enclosed region too high while it is underestimated in the steady flow. Both cases are caused by a lack of mass flow which result in a slower, and therefore less high, flow inside the enclosed region and less particles in the steady flow.

5.6.2 Cross sectional views

The strength of the hydraulic jump can be derived from the rate at which the height increases at the edge of the super-critical region. Figure 5.14(b) shows graphs where the height is plotted over the width of the plate at multiple x locations. From this figure, it can be concluded that the jump closest to the impingement zone (red line) is stronger and reaches a higher value than jumps further away from this zone. Nevertheless, the height of the flow for those lines starts at a lower value, increasing up to 3 mm. On average, the strength of the jump is calculated as the gradient of h with respect to y yielding a strength of 200 mm/m within $0.04 \text{ m} \leq x \leq 0.07 \text{ m}$.

5.6.3 Conclusion

This section showed the height of the flow in top and cross sectional views. Discrepancies with the original work are encountered in the height within the enclosed region which is, for the DPM results, too high and after the jump where the DPM results are too low. This is due to the lack of mass flow causing the particles inside the enclosed region to move slower and reducing the amount of particles after the jump. Both of these causes result in a lower and less strong jump which was confirmed by the cross sectional views.

5.7 Characteristics of the enclosed region

The enclosed region is characterised by the length of this region in down-slope direction and the maximum width of the region. This section gives a definition for this length in §5.7.1 and calculates the maximum width in §5.7.2. A conclusion is drawn in §5.7.3 where the results are compared to the results found in the original work.

5.7.1 Length of the enclosed region

The length of the enclosed region is defined as the distance from the stagnation point found in §5.1.2 up to the lowest point in the region [17]. The stagnation point is located at $x = 0.03$ m and the lowest point of the region was found in §5.6 as $x = 0.0595$ m which yields a length of 0.03 m. The teardrop shock, which was encountered for an inclination angle of 26.7° in the original work, showed a length of 0.26 m while the length of the blunted shocks, which were found at lower angles in the original work, ranged from 0.04 m up to 0.10 m. The DPM results show the most similarities with the blunted type of shock and the results are therefore compared with this type of result. The length of the enclosed region as found by the coarse-grained DPM results does not differ much from the lengths found in the original work. Nevertheless, the type of the shock is different which, again, indicates that the mass flow as used by the DPM solver is too small since it lacks kinetic energy in the enclosed region.

5.7.2 Width of the enclosed region

The maximum width of the enclosed region in the coarse-grained DPM results is measured by the maximum distance in-between the two jumps as shown in figure 5.14(b), yielding a width of 0.036 m. The original work showed the enclosed region by the solid black line in figure 5.13(b) and the maximum width is measured as 0.06 m at a down-slope distance of 0.05 m from the impingement point. The results found with the DPM method yield a much smaller width of the enclosed region indicating that the gravitational energy with respect to the kinetic energy in the radial from is much bigger. A higher mass flux should increase the maximum width of the region and it can thus be concluded that the flow lacks mass flow.

5.7.3 Conclusion

The enclosed region is smaller and less wide than the regions found in the original work. Both of these parameters indicate that the mass flow in the system is too small since an increase in this mass flow should yield a longer and wider enclosed region.

5.8 Parameter study

The previous sections considered the DPM results for an inclination angle of 26.7° and a falling height of 0.05 m which corresponded to the teardrop simulations performed in the original work. This section shows two other angles, 23.0° and 29.0° in §5.8.2 which were chosen according to the limits of the steady results shown in the original work. Furthermore, an extension in falling height is introduced in §5.8.2 by raising it to 0.075 m resulting in a jet velocity of 1.21 m/s. Conclusions are drawn based on these extensions in §5.8.3

5.8.1 Inclination angle

The influence of the inclination angle on the DPM results is investigated with the use of the resulting height profiles and the Froude numbers in the system. The enclosed region can be characterised with these fields as seen in §5.7. Figure 5.15 shows the height in millimetres and Froude number in the flow for three inclination angles, $\zeta = 23.0, 26.7$ and 29.0° respectively, from which it is clear that higher inclination angles cause a bigger enclosed region. The typical volume fraction for the lowest angle is 0.516 and 0.461 for the highest angle. The length of the regions is equal to 0.01 m, 0.03 m and 0.05 m respectively where the last is in the range as found by the original work. The minimum heights of the regions are 1.42 mm, 0.86 mm and 0.68 mm respectively, confirming the hypothesis that a less energetic mass flux causes a higher flow within the enclosed region. The width of the regions varies from 0.027 m for the lowest and up to 0.045 m for the highest angle which are both below the measured values in the original work. The figures also show that a higher inclination angle does not directly result in a less blunted shape.

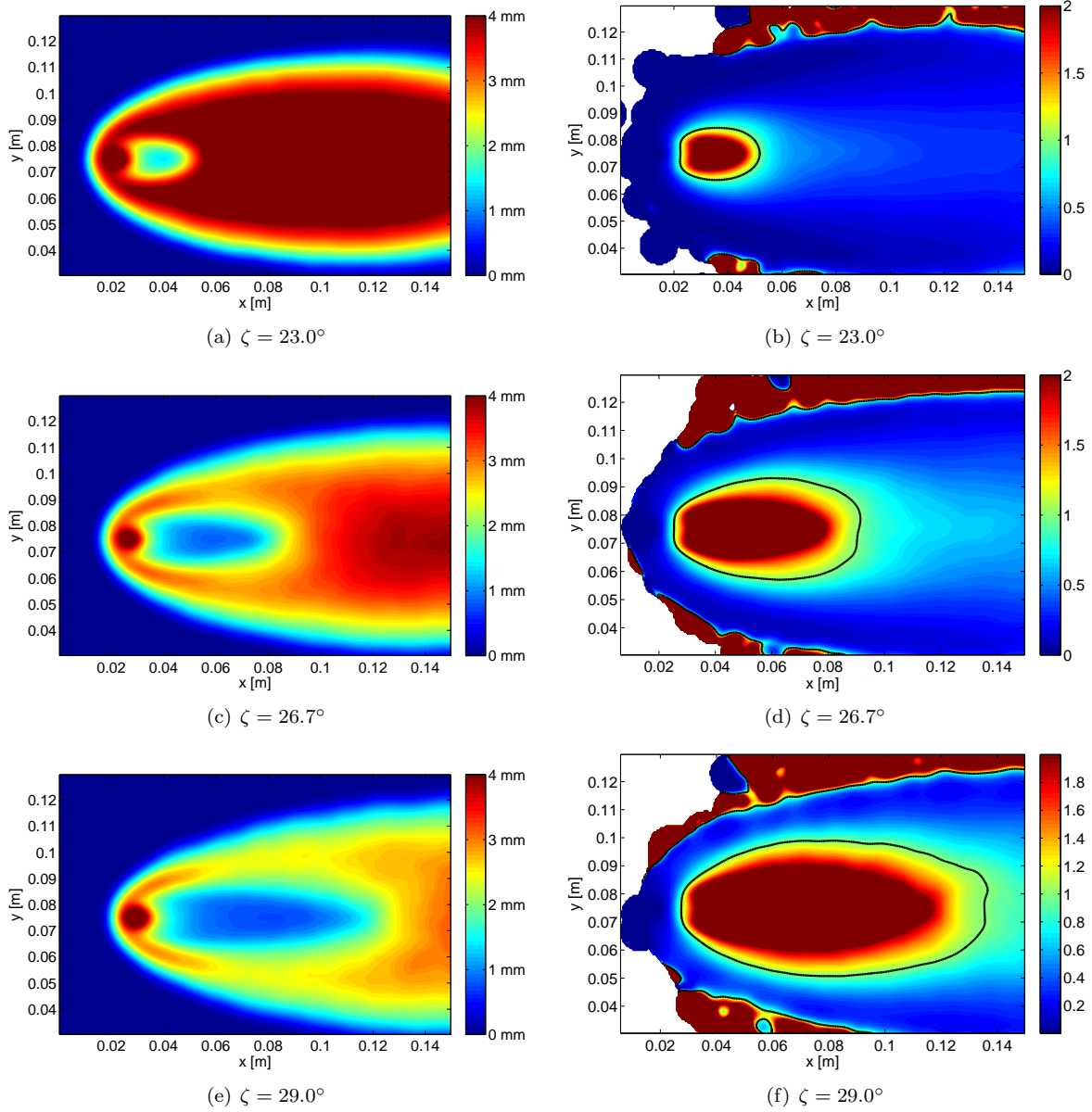


Figure 5.15: Height of the flow in millimetres and Froude number for three inclination angles and a falling height of 0.05 m. The fields are evaluated uniformly in x and y directions each 0.001 m.

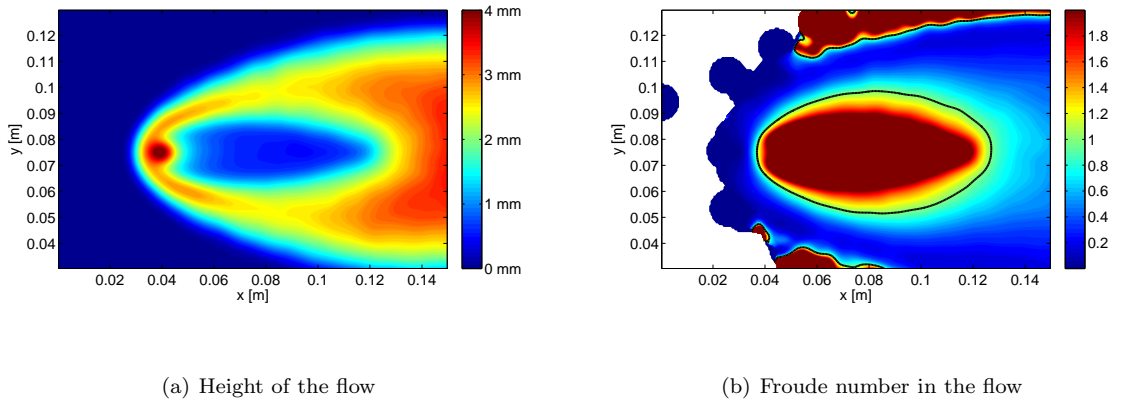


Figure 5.16: Characterisation results for a falling height of 7.5 cm and an inclination angle of $\zeta = 26.7^\circ$. The fields are evaluated uniformly in x and y directions each 0.001 m.

5.8.2 Falling height

Another system parameter having a significant influence on the results is the falling height since it raises the potential energy of the jet. This potential energy is converted into kinetic energy by conservation of energy yielding a higher jet velocity,

$$u_{jet} = \sqrt{2H_f g}. \quad (5.14)$$

Figure 5.16 shows the height (a) and Froude number (b) for a falling height of 7.5 cm corresponding to a jet velocity of 1.21 m/s. The typical volume fraction (5.5) is based on the region $x > 0.14$ m, 0.05 m $\leq y \leq 0.10$ m yielding a value of 0.50. These figures are compared with figures 5.14(a) and 5.12(b) respectively to find the differences in the characteristics of the enclosed region. The lowest point in the enclosed region is located at $x = 0.091$ m yielding a length of 0.06 m for this region. Even though such a length is bigger than the length of the simulation with a falling height of 0.05 m and the same inclination angle of 26.7° , it is still smaller than the lengths found in the original work. The Froude number shows that the shape is less blunted than those found in §5.8.1 which is due to the higher kinetic energy in the jet. Nevertheless, it is still classified as a blunted shock.

5.8.3 Conclusions

Even though the higher inclination angle and falling height increase the kinetic energy in the system, a teardrop shaped enclosed region is not found. Nevertheless, steady states were formed and the shape became less blunted. Therefore, a simulation with a much higher falling height is investigated in §5.9.

5.9 Highly kinetic flow

A simulation with much bigger falling height simulating heavier particles is started to investigate a highly kinetic jet where the setup parameters are shown in §5.9.1. This simulation ran for 55 days in which 1,000,000 particles over three seconds are simulated yielding a solution which cannot be classified as a steady state, i.e. the shape of the flow changes with time. Nevertheless, these results look promising and are thus discussed in this section. The mass flow in this system is discussed in §5.9.2, followed by the discrete results for the plate flow (§5.9.3) and the hydraulic jump (§5.9.4). These results are coarse grained to obtain the Froude number (§5.9.5) and the height (§5.9.6) of the flow allowing for the characterisation of the enclosed region. A coarse grained view on the impingement zone is shown in §5.9.7 and conclusions are drawn based on the gathered results in §5.9.8. Note that the simulation was performed in the early stages of the thesis in which several particle properties were unknown and computational errors still existed.

5.9.1 Setup parameters

As stated, the simulation at hand differs from the work presented in chapter 5 in both particle and system properties. This section lists the particle properties in table 5.1 and the system properties in 5.2. The differences in the particle properties yield heavier and stiffer particles with a higher friction coefficient. The system parameters create a bigger funnel which is located at a higher height. These differences yield more potential energy in the funnel and thus more kinetic energy over the plate.

5.9.2 Mass flow

The bigger funnel outlet diameter and high falling height yield a higher mass flux which can be seen from figure 5.17(a) where the accumulation of particles in the system is shown against time. Due to the size of the domain, which is much bigger than the original domain shown in chapter 3, no outflow of particles takes place and all particles thus stay in the system. It can therefore be concluded that the system is not at steady state and time averaging of results is thus not allowed. Figure 5.17(b) shows the accumulation rate of particles from which one can see that the average accumulation rate after initialisation of the problem is equal to 215,000 particles per second. This number is much bigger than the accumulation rate of the steady results which was 95,000 particles per second but still significantly smaller than the experimental particle rate of 700,000 particles per second.

5.9.3 Plate flow

The higher potential energy, due to the high falling height H_f , yield higher kinetic energy in the flow over the plate which can be clearly seen from figure 5.18 where the flow over the plate is shown at intervals of 0.5s with the visualisation method described in chapter 4. The hypothesis that a steady state is not yet fully reached is confirmed by this visual inspection since the enclosed region is reducing in size while the avalanche further down the plate grows in time. Even though a steady state is not observed, the shape of the enclosed region can be considered a teardrop shape which will be confirmed with the coarse grained results in §5.9.5. Both length and width of the super-critical flow-region are much bigger than those shown in figure 5.4.

S.	Description	Value	Units
d	Particle's diameter	0.006	[m]
μ_c	Friction coefficient	0.8	[-]
ρ	Density	2400	[kg m ⁻³]
t_c	Collision time	2.5×10^{-4}	[s]
e^n	Coefficient of restitution	0.6	[-]
k^t/k^n	Ratio of tangential and normal stiffness	2/7	[-]
γ^t/γ^n	Ratio of tangential and normal dissipation	1	[-]

Table 5.1: Particle properties

S.	Description	Value	Units
ζ	Inclination angle	25.4	[$^{\circ}$]
L	Length of the plate	0.60	[m]
W	Width of the plate	0.25	[m]
H_f	Falling height	0.43	[m]
D	Funnel diameter	0.017	[m]
n_z	Number of particles along the side of the funnel	50	[–]
a	Growth angle	60.0	[$^{\circ}$]

Table 5.2: System properties

5.9.4 Critical transition

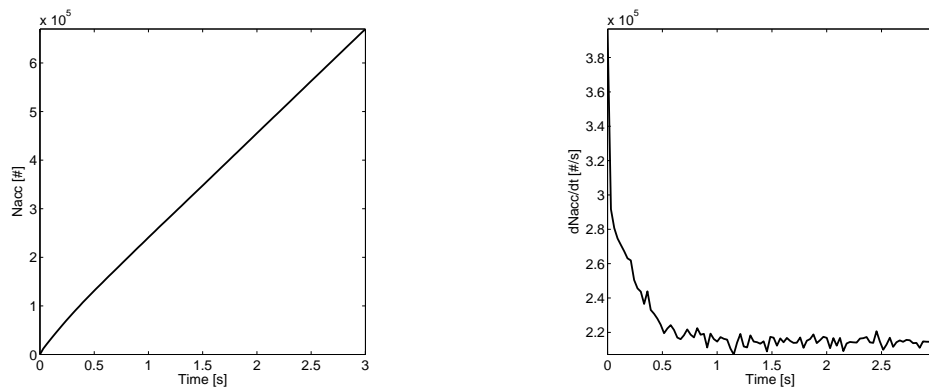
The finite volume results predicted a shock at the location at which the flow changes from super- to sub-critical, but such a steep gradient was not found in neither of the cases studied in the previous sections. Figure 5.19 shows similar cross sections as shown in figure 5.6. These sub-figures within figure 5.19 show a much steeper and clear transition than those in figure 5.6 and are further analysed after coarse graining of the results in §5.9.6.

5.9.5 Froude number

Coarse graining of the discrete set of results presented in the previous sections is performed to obtain the Froude number. The coarse graining domain is limited to obtain a high resolution solution from which the Froude number is shown in figure 5.20(b) in which a typical volume fraction of 0.516 is used. The figure shows a black line corresponding to $Fr = 1$ which is the transition of super- to sub-critical flow. Furthermore, white lines following typical particle paths originating from the impingement zone are added to visualize the flow direction. A near radial flow near the impingement zone is observed which is in agreement with the observations made by Johnson and Gray. Furthermore, the shape of the enclosed region is identified as a teardrop shape which is bigger than those found earlier. The stagnation point is determined in §5.9.7 and located at $x = -0.095$ m and one can see that the sub-critical flow is more energetic than those in the steady state solutions.

5.9.6 Height of the flow

The height of the flow is shown in figure 5.20(a) and one can see that the sub-critical flow is slightly thicker than the steady state flows which had a maximum height of approximately 4 mm. The average height in the sub-critical flow is 4.8 mm and within the super-critical flow 0.65 mm which is equivalent with values found in the original work. The minimum height in the enclosed region is 0.17 mm located at $x = 0.026$ m yielding a length of 0.12 m for the enclosed region. Such a length is equivalent with the



(a) Accumulation of particles against time

(b) Accumulation rate of particles against time

Figure 5.17: Accumulation of particles and the accumulation rate for the unsteady highly kinetic flow

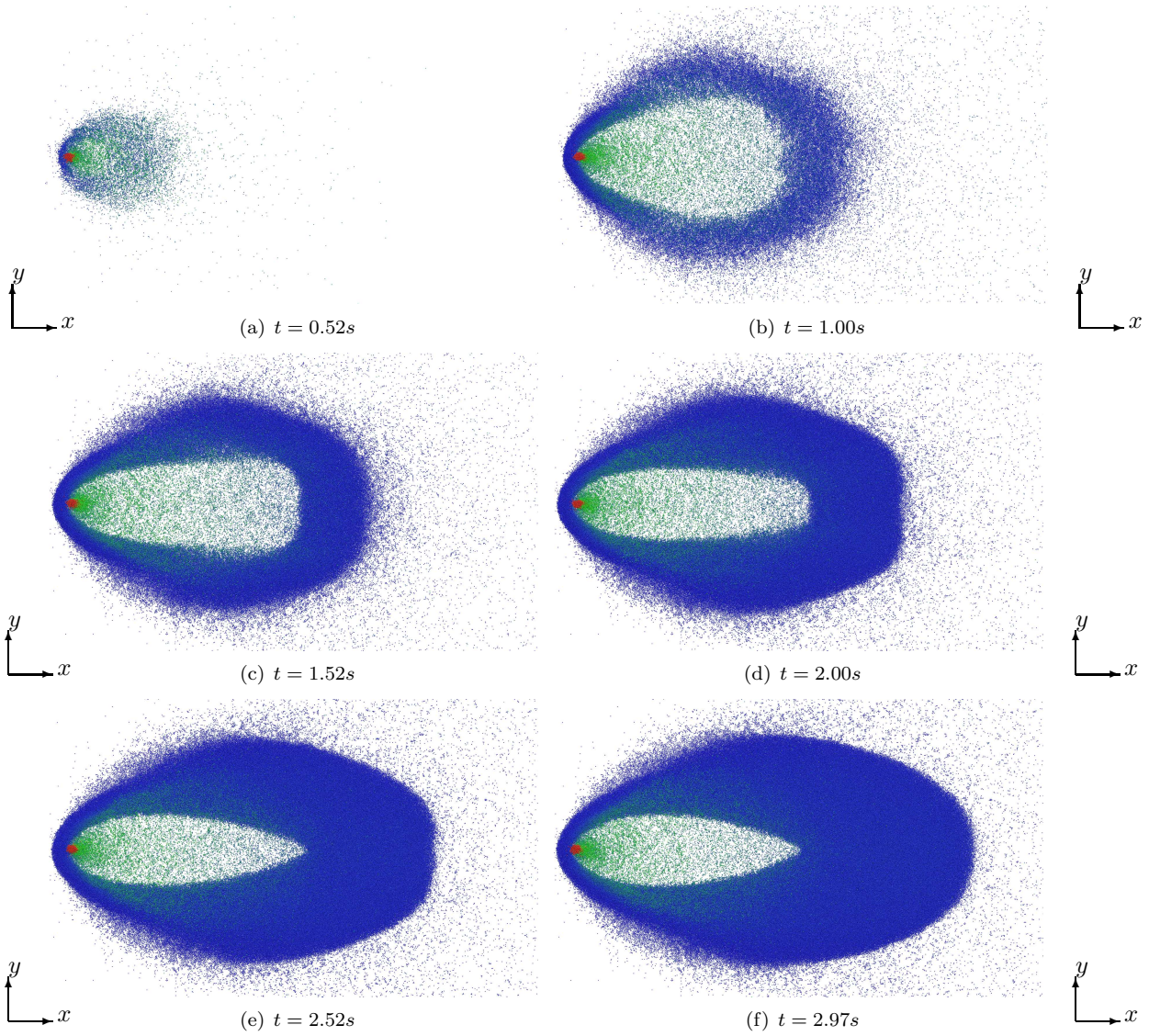


Figure 5.18: The top view of the numerical outcome of the flow over the plate at six different times where blue particles correspond to $\|U\| = 0$ m/s and red particles to $\|U\| = 3.14$ m/s.

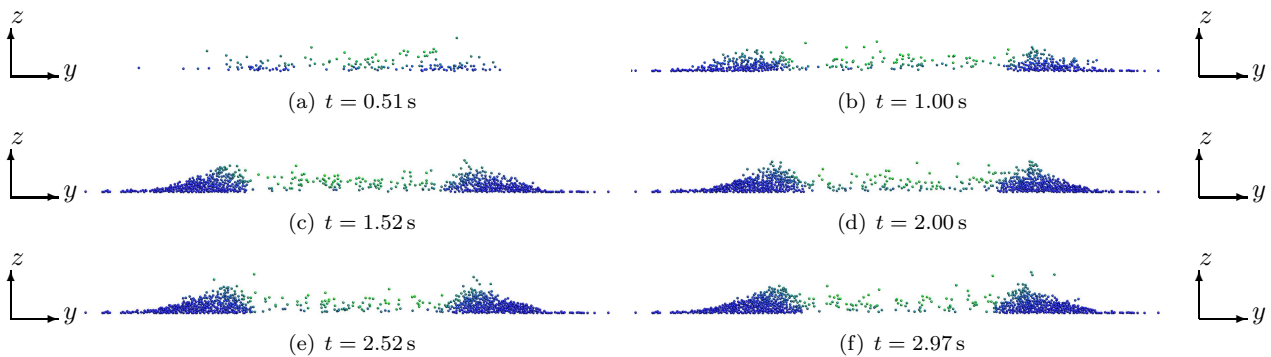
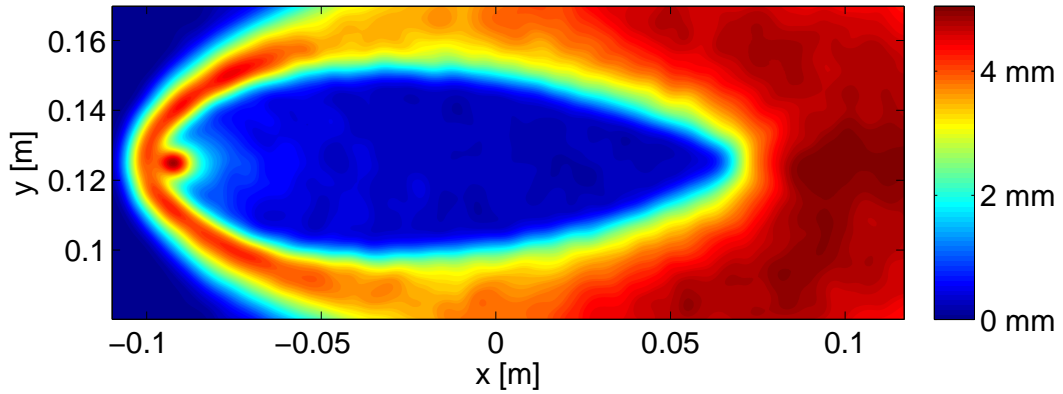


Figure 5.19: Cross sectional views from $x = -0.066$ m up to $x = -0.065$ m for the hydraulic jump in the system. Blue particles correspond to $\|U\| = 0$ m/s and red particles to $\|U\| = 3.14$ m/s. Fixed particles are hidden.



(a) Height of the flow

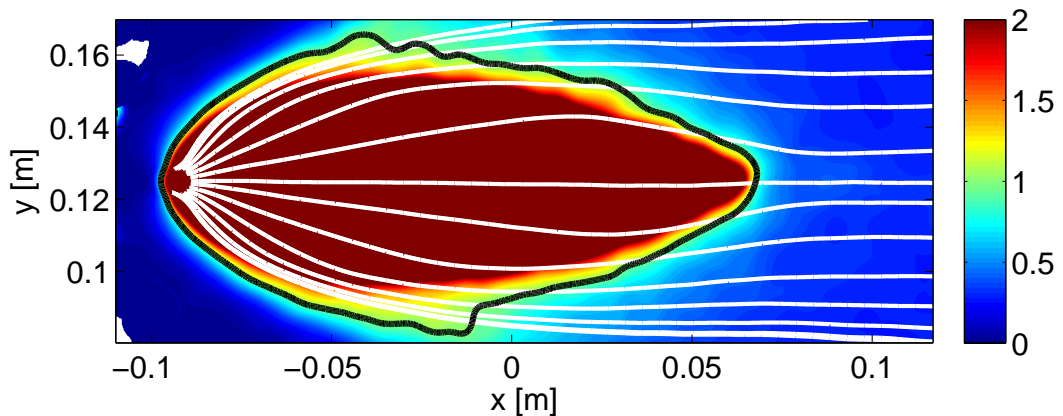
(b) Froude number in the flow where the black line corresponds to $Fr = 1$ and lines of typical particle paths are shown in white.

Figure 5.20: Characterisation results for a falling height of 43.0 cm and an inclination angle of $\zeta = 25.4^\circ$ at $t = 2.97$ s. The fields are evaluated each 0.001 m in both x and y directions.

length of the region in the experimental results [17] where a blunted shock was observed. Note that the simulation at hand did not reach a steady state yet which causes the enclosed area to shrink. The observed teardrop shape result may thus change when the simulation evolves further in time. Figure 5.21 shows cross sections similar to those shown in figure 5.14 and the strength of the hydraulic jump is calculated as 350 mm/m which is much more than those observed in the steady state solutions which had a strength of 200 mm/m.

5.9.7 Impingement

Coarse grained results in the (x, z) plane are calculated for the highly kinetic simulation to obtain more insight in the flow through the impingement zone. Figure 5.3(a) showed the flow profile through the impingement zone as proposed by Johnson and Gray [17]. The coarse grained density is shown as a contour plot in figure 5.22 where white streamlines are added to visualise the flow profile. The figure shows the x, z plane which is located at $y = 0.125$ m. The stagnation point is identified with the streamline flowing perpendicular into the bottom wall and is located at $x = -0.095$ m. The high density region in up-slope direction is caused by the small flow of particles going into that direction which can be seen from the single particle path flowing in that direction. This phenomenon is equivalent with experimental observations. Based on this graph, it can be concluded that the flow profile in DPM simulations matches the proposed profile in the original work.

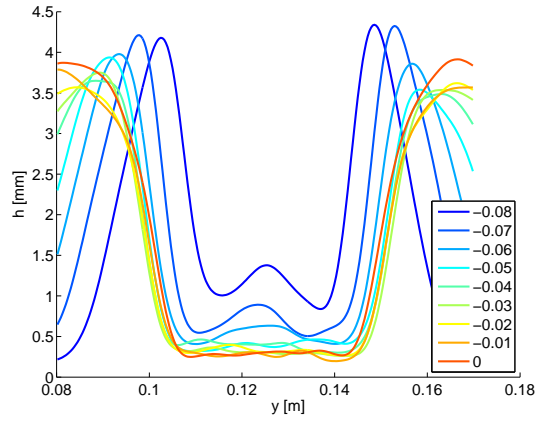


Figure 5.21: Cross sectional vies of the height of the flow over the width of the plate in the range $-0.08 \text{ m} \leq x \leq 0.00 \text{ m}$ for the jet originating from $H_f = 0.43 \text{ m}$ and an inclination angle of $\zeta = 25.4^\circ$ at $t = 2.97 \text{ s}$

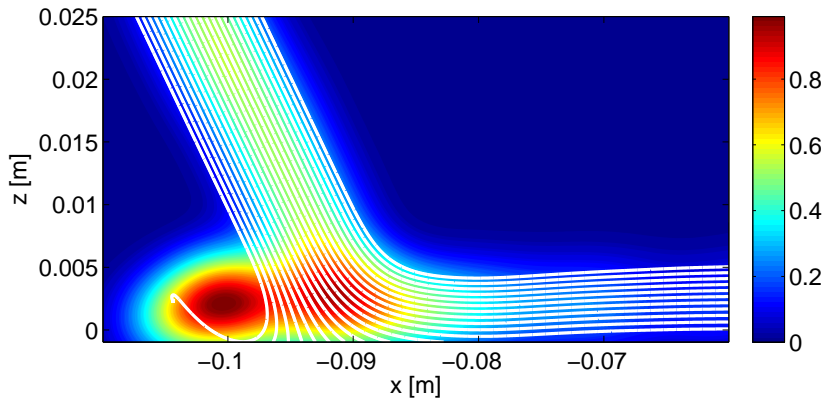


Figure 5.22: The flow through the impingement zone for the jet originating from $H_f = 0.43 \text{ m}$ and an inclination angle of $\zeta = 25.4^\circ$ at $t = 2.97 \text{ s}$. The density of the flow is shown by the contour plot which is generated in the (x, z) plane located at $y = 0.125 \text{ m}$ having a uniform spacing of 0.001 m . Typical flow paths are added in white.

5.9.8 Conclusions

Even though the absence of a steady state, the highly kinetic flow is analysed. This analysis showed a teardrop shaped enclosed region which had a length which is comparable to the experimental results. However, the region will shrink and its shape may change with the shrinkage. The hydraulic jump separating the super- from the sub-critical is stronger than the one observed in the steady state solution. Nevertheless, the jump is still weaker than those observed in experiments and finite volume results. The increased mass flow, combined with the significant increase in falling height emphasises that the DPM method is capable of modelling the problem. A full phase diagram as shown in Johnson and Gray [17] can be found since both types of the enclosed region are now found with the DPM method. However, it is strongly advised to parallelise the current code to reduce the computational time which is discussed in the next chapter.

Chapter 6

Parallelisation

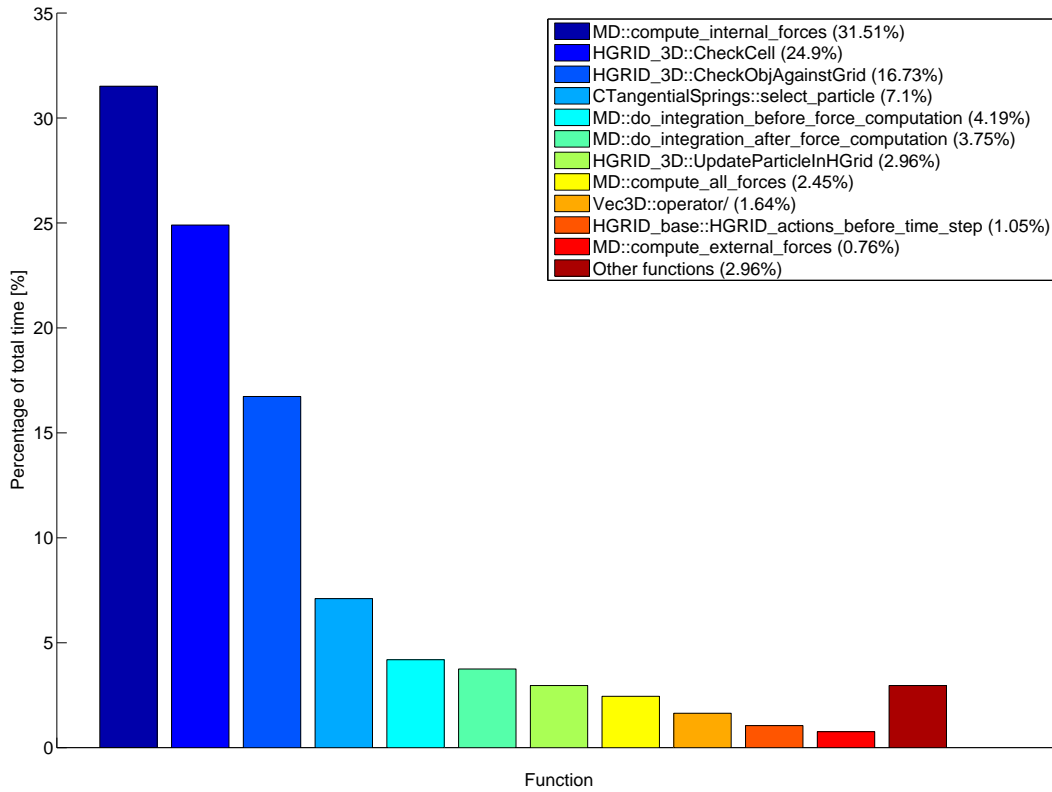
The results chapter showed that the mass flow should be increased significantly to obtain more realistic results but that the solver is limited by computational time. Decreasing this time can be done by parallelisation of the code, allowing multiple processors to work on one problem. This chapter therefore identifies the sections of the code where most of the computational time is spent in §6.1 and this profile is used to perform a preliminary study on the possibilities of applying the OpenMP [5] parallelisation method on the code (§6.2).

6.1 Profiler

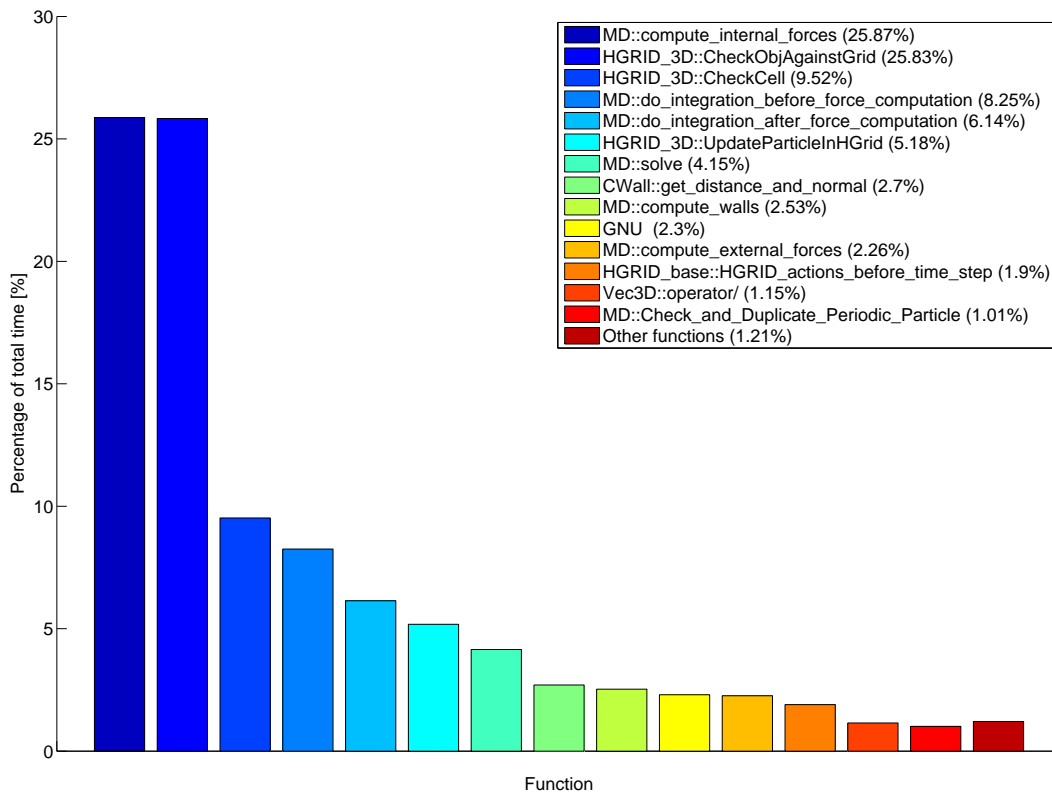
Investigating the computational time spent on certain functions within a code provides insight in the bottlenecks of such a code. Profiling is a tool to determine the computational time spent in each routine and `gprof` [9] is a tool which can be used to profile C++ codes. The resulting profile does not include the time spent on reading and writing nor the time used to swap memory. Where memory swapping is changing of the data which is instantaneously available for a processor. The total time used reported by the profiler is thus not equal to the wall-clock time which is the time in seconds needed for the execution of the programme. The profiler is applied to the computation of 25,000 time-steps in the steady state solution which is shown in §5.1-§5.7 and 375,000 time-steps in the unsteady highly kinetic simulation shown in §5.9. While the main functions within the code are the same for both problems, there are differences in the specific functions which are used in the initialisation of the problem. The parameters for the contact detection method are optimised for the steady-state solution which reduce the computational time and thus influences the profile output. Figure 6.1 shows the computing time spent in individual functions for both simulations and one can see that the functions containing differences are not listed which is due to the fact that these are only used in initialisation of the problem. As expected, most of the computational time is spent by calculating particle-particle collisions in the `compute_internal_forces` routine. In both cases, two other functions are also computationally expensive; `CheckCell` and `CheckObjAgainstGrid` which are both functions used by the contact detection method. Time integration before and after the force computation also contributes significantly to the computational time. Parallelising these functions is thus advised since they consume most of the computational time, where it can lead to a speedup of maximal,

$$\eta = \frac{1}{(1 - P) + P/S}, \quad (6.1)$$

according to Amdahl's law where the maximum speedup η depends on the parallelised proportion P of the code which can get a speedup of S . This law assumes that the computational effort does not increase with parallelisation, i.e. the overhead due to parallelising is equal to the overhead present in the same sequential code. The profiles as shown in figure 6.1 show that the most expensive functions accumulate up to 88% in the steady flow simulations and up to 76% in the unsteady flow. If it is assumed that the speedup S scales linearly with the number of processors used, speedups ranging from 4.1 for the unsteady flow and up to 8.5 for the steady flow if an infinite amount of processors is used, i.e. $\lim_{s \rightarrow \infty} P/S = 0$.



(a) Computational profile of the code for the steady flow



(b) Computational profile of the code for the unsteady high kinetic flow

Figure 6.1: Computational profiles for two simulations executed with Mercury where the value of the bin is the self-time, i.e. the time a function uses without calling other functions. Listed are the functions with the highest contributions and an 'Others' bin is added visualise the remaining part

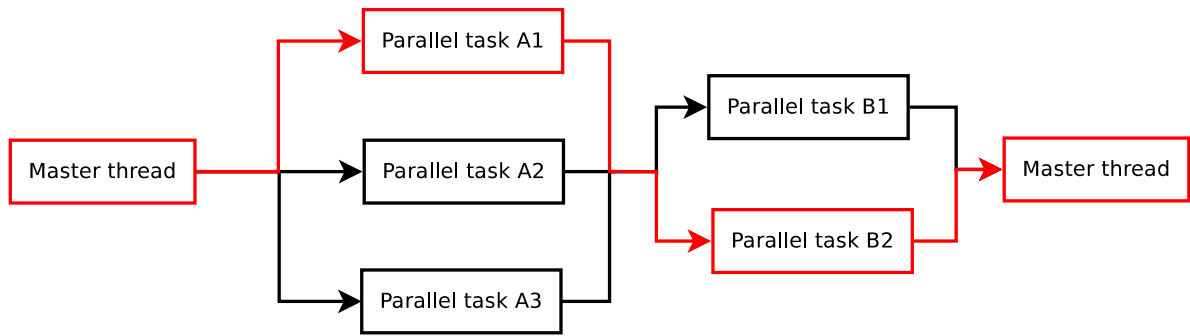


Figure 6.2: Flowchart of a parallelised code with two parallel regions.

6.2 OpenMP

The OpenMP parallelisation method is an ‘easy to apply’ parallelisation method and it is chosen for that reason. It stands for ‘Open Multi-Processing’ and it is a parallelisation method which can be applied on platforms which share memory, like multicore computers. The method can be applied to, for instance, C++ code where it is interpreted at the compilation of the code. Simple `pragma`s indicate locations at which the code should be compiled with OpenMP standards. Therefore, a `-fopenmp` flag should be added to the compiler, such as `gcc`, and it is important to optimise memory handling within OpenMP parallelised codes. This section briefly explains the method in §6.2.1 and discusses the parallelisation possibilities for the expensive functions in the source code of Mercury [26] (§6.2.2).

6.2.1 Introduction into OpenMP

Sequential codes execute a code in a single thread, where a thread is a single processor having access to the shared memory. The required computational time is fully dependent on the computational power available within that thread. Parallelised codes use multiple threads allowing for a maximum speedup which depends on the size of the parallelised regions according to Amdahl’s law (6.1), which is limited by the efficiency of parallelisation and the computational power in each thread. OpenMP is an implementation of multithreading and a code can thus be split in several parts which are executed parallel. A master thread is then pointed out in which the sequential parts, such as initialisation of parameters, of the code are executed. Figure 6.2 shows an example of a parallelised code with two parallel regions in which the first region is executed by three and the second by two threads. The red line within this figure indicates the work performed by the master thread. The other threads are indicated as ‘slave’ threads and the master thread decides the task they should perform. All the threads require read and write access to the data used and produced by other threads and the method is therefore limited to systems which share memory, i.e. multicore systems. Computational clusters with several nodes can thus not be used in OpenMP parallelisation due to the fact that the memory in these clusters is typically not shared over the processors.

The ‘parallel’ pragma

Parallelising a code with the OpenMP method uses ‘parallel’ pragma’s which are directives to specify machine- or operating-specific computer features. These pragma’s are interpreted in the compiling step of a C++ code and determine the parallel regions of a code. The coded box below shows an example in which a print command is parallelised and executed by the number of threads used, i.e. the word ‘Hello’ is printed twice if the code is executed on a dual-core machine. Due to the possibility of an unbalanced load distribution among the used threads it is also possible that ‘HeHllelloo’ is produced as output. The parallel execution of a script is thus neither chronological nor lexicographic by default.

```
#pragma omp parallel
{
    printf("Hello");
}
```

For loops

Typical regions of code which should be parallelised are `for` loops since these regions repeat a certain calculation many times. The computational expensive functions stated in §6.1 loop over all, or a selection of, particles in the system, causing a significant portion of computational time. A `for` loop can be parallelised with the ‘parallel’ pragma explained above where a specific pragma for the `for` loop is added at the location of the loop,

```
#pragma omp parallel
{
  #pragma omp for
  for (int i=0; i<10; ++i) printf(" %d",i);
}
```

where the loop is thus executed by multiple threads and the output may not necessary be in order, i.e. the output can be 0576123894.

Critical regions

Sections of code where the order of execution matters are called critical regions. Time integration is such a section for DPM simulations since all previous variables are needed before the integration can take place, see the algorithm shown in 1. Furthermore, write actions can also not be parallelised since the order of the output is very important. The `critical` directive ensures that such a region is executed by a single thread which guarantees the order of the output but yields a slowdown in the execution of the code, i.e. the overhead of a critical region is higher than the overhead of the sequential code itself.

Performance issues

The performance of a parallelised code strongly depends on the memory handling. The efficiency of this memory handling depends on the order of accessing data in a problem. A processor reads blocks of memory in stead of single lines. For instance, the data of all particles with an index less then 10 are copied in the memory when the data of particle 1 is required by the code. It thus overwrites existing data in the memory if that is necessary. Accessing particles 2 to 10 can then be done without a swap of memory. Lexicographic looping cause low memory swapping time since it loops index-wise over the data, i.e. from particle i to $i+1$, and is thus relative efficient. The size of the block depends on the size of the memory available and may differ for different processors. The performance of parallelised code thus depends on the hardware used. Overhead caused by parallelisation can be reduced significantly when this memory handling is performed perfectly, yielding speedups which are more than linear [5].

6.2.2 Parallelising Mercury

Section §6.1 showed that the major computational expensive functions check the location of the particles, calculate the forces in particle-particle collisions and perform the time integration. These routines are in general `for` loops and it should be possible to parallelise those. However, as pointed out in §6.2.1 memory handling is very important in the performance of a OpenMP based parallelisation of the code. Lexicographic looping is not possible due to the contact detection method which searches for particles inside closed boxes in the system. The encountered particles are not necessary ordered by index (lexicographical) and memory swapping therefore expected. No significant speedup can thus be achieved when the current version of Mercury is parallelised with the OpenMP parallelisation method. Therefore, it is advised to use combination of the OpenMP and the Message Passing Interface methods in a spatially distributed system. The system can then be parallelised with domain decomposition allowing for a significant speedup of the code. On the other hand, applying a so-called Morton ordering on the particles lead to a possible application of OpenMP on Mercury. This ordering sorts the particles based on their ‘`z-value`’ which is a one-dimensional representation of any multidimensional point. The value is a mixture of the binary representations of the coordinates in any dimension and allows for easy one-dimensional sorting algorithms. Applying the Morton algorithm together with a simple tree-sort algorithm yields a ordered list of particles which can be looped lexicographical, i.e. the index of a particle is now based on its `z-value`. OpenMP applied to this sorted system is thus

beneficial since the computational cost of memory swapping is significantly reduced. These hypotheses are not further investigated within the scope of this thesis.

Chapter 7

Conclusion and discussion

Real sized problems, such as a granular jet impinging on an inclined plane, are normally solved via continuum models such as the granular shallow layer equations. These models reduce the degrees of freedom in the flow to two variables, flow height and velocity resulting in a two dimensional solution. In contrast, the discrete particle method (DPM) does not need the granular shallow layer equations nor the assumptions made in these equations and simulates the whole flow particle-wise, yielding a fully three-dimensional solution. In this thesis, the application of the DPM method on big problems is investigated. The studied problem involved up to 1,000,000 particles which are simulated over 500,000 time-steps to answer the main research question: *Up to which level of detail is DPM capable of simulating a granular jet impinging on an inclined plane, confirming both the experiments as well the finite volume results from Johnson and Gray [17]?* The original work of Johnson and Gray [17] considered the same problem where both experiments and the finite volume method were used to obtain steady state solutions. In this research, similar results were found confirming the hypothesis that DPM is capable of simulating such a complex flow. Two types of simulations, steady state and highly kinetic ones, are used in the further analysis on the details of the flow. These simulations are used to answer the five sub-questions which are discussed in the upcoming paragraphs.

The first sub-question was listed as: *Does the flow profile within the impingement zone as found with the DPM model satisfy the assumptions made in the granular shallow layer equations?* A vertical cross section along the flow of the highly kinetic data is used in answering this question. The cross section showed typical particle paths through the centre of the jet near the impingement zone. A stagnation point was found, equivalent to the one proposed by Johnson and Gray. Moreover, the remaining part of the profile satisfied the same model. The discrete particle method provided the missing insight in this three-dimensional flow and it is thus proven that the method is capable of resolving unknown solutions.

“Is the DPM method capable of capturing a phenomenon similar to the hydraulic shock observed in the original work?”, is the second sub-question listed. Both types of simulations are used in answering this question. The steady state low mass-flux solution showed a weak transition where the flow within the super-critical region discharged in the sub-critical flow zone. This results in a high mass-flux relative smooth raise in the height of the flow. A stronger transition was found in the highly kinetic solution. Even though the mass flow is currently limited to a fraction of the original mass flow due to limits in the computational power, similarities were found. Moreover, the missing three-dimensional insight in these jump regions is provided by the applied DPM method.

A third aspect in the research was: *Can both typical solutions, found in the experiments and finite volume results, for the enclosed region be found with the DPM method?* The original work showed two distinct types of solutions to the impingement problem. One with a blunted shape enclosed region of highly kinetic flow and another which they called the teardrop shape. A parameter study on the inclination angle of the plate and the falling height of the jet were mapped in the original work. The DPM simulations showed both types from which the blunted shape region was found in all steady state solutions. A teardrop shape solution was found in the highly kinetic simulation, which approached a steady state. Extension of the found solutions into the full parameter space is not performed within this research due to not knowing the exact material properties, such as the friction coefficient. Little effort on increasing the computational efficiency will allow for the full mapping of the parameter space and a more detailed study on the material properties.

Investigating the fully three-dimensional flow at the down-slope end of the enclosed region was the

fourth research aspect. A steady and uniform flow was found in the DPM simulations confirming the low kinetic regimes in this flow. Furthermore, stationary particles on the boundary of the flow were also found which confirmed experimental observations. However, the complex three-dimensional flow at the point where the enclosed region ends was not found due to the lack of mass flux. This drawback can easily be overcome when the computational efficiency is increased as discussed in the next paragraph.

The fifth sub-question was listed as: *Can the computational time of the DPM method as used in the open source software Mercury [26] significantly be reduced by applying the OpenMP parallelisation method?* It focusses on the increase of computational power for the DPM method. The DPM solver used, Mercury, is an open source DPM solver which is developed by the Multi Scale Mechanics group within the University of Twente. This solver, as it is applied on the granular jet, is profiled to obtain insight in the distribution of computational power while simulating a big problem. The force calculation in particle-particle collisions, the contact detection algorithm and the time-integration scheme are identified as the computational bottlenecks. The OpenMP parallelisation method is analysed and good performance with this method is achieved when it is applied to systems which are solved chronological or lexicographical. The contact detection algorithm causes a non-chronological nor lexicographical looping and yield therefore a very high computational overhead. It is therefore not expected that application of the OpenMP method on the current code yields a significant speedup. Application of a domain-decomposed parallelisation algorithm with non-shared memory is advised to overcome this overhead. On the other hand, significant speedup can be achieved by mapping the three-dimensional particle locations in a one-dimensional space with use of Morton sorting. This allows for lexicographical looping over the particles since their index then corresponds to the position on the Morton curve. Issues of memory swapping are significantly reduced and it is expected that near-linear speedups with the OpenMP algorithm can be found.

Additionally, a fully three-dimensional and interactive visualisation method is developed within this research. The method uses an existing OpenGL rendering engine which is specialised in the visualisation of Molecular Dynamics, VMD. This software is modified to represent the DPM results with all of its details. Furthermore, cross sectional views can easily be generated and investigated allowing for a fully three-dimensional inspection of the results. The method is also capable of visualising objects such as (finite) walls or automatic rotation which can be used in simulations of e.g. rotating drums.

With all sub-questions answered, it is possible to answer the main research question. The simulations performed within this research showed significant similarities to the observations made in experiments and the finite volume method. Moreover, three-dimensional flow is analysed near the impingement zone, confirming the proposed flow model in the original work. With both typical solutions at hand it is also expected that the a parameter space can easily be found with DPM. Such a parameter space can then be compared to the original work. Increasing computational efficiency by applying a parallelisation method using domain-decomposition and/or the application of a Morton curve advised. Detailed studies on both, material and system, parameters can then easily be performed.

Bibliography

- [1] O. Bokhove and A. Thornton. Shallow granular flows. *Bookchapter in Handbook of Environmental Fluid Dynamics*, 2011.
- [2] J. Boudet, Y. Amarouchene, B. Bonnier, and H. Kellay. The granular jump. *J. Fluid Mech.* 572:413-431, 2007.
- [3] J. Bush and J. Aristoff. The influence of surface tension on the circular hydraulic jump. *J. Fluid Mech.* 489:229-238, 2003.
- [4] C. Campbell and A. Gong. The stress tensor in a two-dimensional granular shear flow. *J. Fluid Mech.* 164:107-125, 1986.
- [5] B. Chapman, G. Jost, and R. v. d. Pas. *Using OpenMP*. Massachusetts Institute of Technology, 2008.
- [6] M. Cieplak, J. Koplik, and J. Bavanar. Molecular dynamics of flows in the knudsen regime. *Physica A* 287:153-160, 2000.
- [7] P. Cundall and O. Strack. A discrete numerical model for granular assemblies. *Geotechnique*, 29(4765), 1979.
- [8] I. Goldhirsch. Stress, stress asymmetry and couple stress: from discrete particles to continuous fields. *Granular Matter* 12:239-252, 2010.
- [9] S. Graham, P. Kessler, and M. McKusick. gprof:a call graph execution profiler. *Proceeding SIGPLAN '82 Proceedings of the 1982 SIGPLAN symposium on Compiler construction*, 1982.
- [10] J. Gray. Rapid granular flow. *Unpublished*.
- [11] J. Gray. Granular flow in partially filled slowly rotating drums. *J. Fluid mech.* 441:1-29, 1999.
- [12] J. Gray, Y. Tai, and S. Noelle. Shock waves, dead zones and particle-free regions in rapid granular free surface flows. *J. Fluid Mech.* 491:161-181, 2003.
- [13] J. Gray, M. Wieland, and K. Hutter. Gravity-driven free surface flow of granular avalanches over complex basal topography. *Proc. R. Soc. Lond. A.* 455:1841-1874, 1999.
- [14] R. Hartkamp, T. Weinhart, S. Luding, and A. Ghosh. A study of the anisotropy of stress in a fluid confined in a nanochannel. 2011.
- [15] P. d. i. H. Hoeijmakers. Gasdynamics. (115434) *Lecture notes - Part I, release 1.0*, 2010.
- [16] W. Humphrey, A. Dalke, and K. Schulten. VMD – Visual Molecular Dynamics. *Journal of Molecular Graphics*, 14:33–38, 1996.
- [17] C. Johnson and J. Gray. Granular jets and hydraulic jumps on an inclined plane. *J. Fluid Mech.* 675:87-116, 2011.
- [18] J. Lord Rayleigh. On the theory of long waves and bores. *Proc. R. Soc. A.* 90:324-328, 1914.
- [19] S. Luding. Collisions & contacts between two particles. *H. J. Herrmann, J.-P. Hovi, and S. Luding, (ed.), Physics of Dry Granular Media, NATO ASI Series E350, Kluwer Academic Publishers, Dordrecht, 285.*, 1998.

- [20] S. Luding. Structure and cluster formation in granular media. *Pramana-J. of Phys.* 64(6):893-902, 2005.
- [21] S. Luding. Introduction to Discrete Element Methods: Basics of Contact Force Models and how to perform the Micro-Macro Transition to Continuum Theory. *Journal of Environmental and Civil Engineering EJECE* 12:785-826, 2008.
- [22] L. Meirovitch. Fundamentals of vibrations. *McGRAW-HILL, ISBN 0-07-288180-1*, 2001.
- [23] O. Pouliquen. Scaling laws in granular flows down rough inclined planes. *Physics of Fluids*, 1999.
- [24] O. Pouliquen and Y. Forterre. Friction law for dense granular flows: application to the motion of a mass down a rough inclined plane. *J. Fluid Mech.* 453:133-151, 2002.
- [25] S. Savage and K. Hutter. The motion of a finite mass of granular material down a rough incline. *J. Fluid Mech* 199:177-215, 1989.
- [26] A. Thornton, T. Weinhart, D. Krijgsman, and R. Fransen. Mercury discrete particle simulations. www2.msm.ctw.utwente.nl/athornton/MD, 2011.
- [27] E. Wajnryb, A. Altenberger, and J. Dahler. Uniqueness of the microscopic stress tensor. *J. Chem. Phys.* 103:9781-9787, 1995.
- [28] E. Watson. The radial spread of a liquid jet over a horizontal plane. *J. Fluid Mech.* 20:481-499, 1964.
- [29] v. d. E. Weide. Discretization schemes for hyperbolic partial differential equations. 2009.
- [30] T. Weinhart, A. Thornton, S. Luding, and O. Bokhove. Closure relations for shallow granular flows from particle simulations. *Granular Matter*, submitted August 2011, 2011.
- [31] T. Weinhart, A. Thornton, S. Luding, and O. Bokhove. From discrete particles to continuum field near a boundary. *Granular Matter*, submitted August 2011, 2011.
- [32] F. White. The Buckingham π theorem in dimensional analysis. *Fluid Mechanics, Sections 5.1-5.4*.